

Microcratering in Polyvinylidene Fluoride

by

Anthony John Shu

B.A., University of California Berkeley, 2009

A thesis submitted to the
Faculty of the Graduate School of the
University of Colorado in partial fulfillment
of the requirements for the degree of
Doctor of Philosophy
Department of Physics

2015

This thesis entitled:
Microcratering in Polyvinylidene Fluoride
written by Anthony John Shu
has been approved for the Department of Physics

Tobin Munsat

Prof. Mihály Horányi

Date _____

The final copy of this thesis has been examined by the signatories, and we find that both the content and the form meet acceptable presentation standards of scholarly work in the above mentioned discipline.

Shu, Anthony John (Ph.D., Physics)

Microcratering in Polyvinylidene Fluoride

Thesis directed by Prof. Tobin Munsat

Dust is defined as macroparticles as small as a few molecules up to several micrometers in diameter. In the context of space exploration, it was originally seen only as a technical obstacle to applications; dust can damage instrument surfaces, coat mating surfaces preventing proper seals, and impair or obstruct measurements. Because of the ubiquity of dust in the solar system and its role in the origin of planets and other bodies, the study of dust and related phenomena has evolved to a scientific subdiscipline which can provide us insight into the origins and evolution of our solar system.

In order to facilitate this, a hypervelocity dust accelerator has been built at the University of Colorado at Boulder and is being used to probe impact phenomena, dust mitigation techniques, dust detection techniques, and more. One such dust detector is a Polyvinylidene Fluoride (PVDF) dust detector. The PVDF dust detector is very lightweight and consumes little power. Due to these properties, PVDF detectors can potentially be used on any spacecraft to gain information on the local dust environment. It is not fully understood how this PVDF dust detector signal is generated, so at present can only be used as a dust counter.

In this thesis I discuss the importance of the study of dust phenomena, describe the accelerator experiment, and describe a study conducted to determine the underlying physical principles of PVDF dust detectors. This included measuring crater size scaling laws, measuring the detailed shape of craters, and applying this data to simulations of the signals being generated by PVDF detectors.

Dedication

To all of the fluffy kitties, clearly already evil beings of death and destruction.

Acknowledgements

The author would like to thank Tobin Munsat for all the support he has provided throughout this process. Also, Drs. Anne-Lise Routier-Kierzkowska and Dorota Kwiatkowska for allowing the use of their 3D reconstruction code in conducting this study and the Nano-Characterization Facility at the University of Colorado, Boulder for their help in using the FIB and FESEM as well as the dust accelerator facility at the Max Planck Institut für Kernphysik in Heidelberg, Germany. This project was performed using funding from the National Aeronautics and Space Administration, the National Lunar Science Institute, and the Solar System Exploration Research Virtual Institute.

Contents

Chapter

1	Introduction	1
1.1	Dust Research	1
1.2	Laboratory experiments	4
1.3	PVDF Detectors	5
2	The Accelerator	9
2.1	The Accelerator	12
2.1.1	Overview	12
2.1.2	Dust Source	14
2.1.3	Focusing and High Voltage	17
2.1.4	Detectors and Particle Selection	20
2.1.5	Second Generation PSU	30
2.2	Results	32
2.3	Data Handling	36
2.4	Current and Future Work	37
3	Cratering	40
3.1	Introduction	40
3.2	Experimental methods	41
3.2.1	Overview	41

3.2.2	Imaging using scanning electron microscopes	42
3.2.3	Focused Ion Beam Cross Sectioning	44
3.2.4	3D reconstruction using Stereophotogrammetry	47
3.2.5	Elemental analysis using EDS	52
3.3	Scaling-Law Results	55
3.4	Conclusions and Future Work	61
4	Cratering Theory	63
4.1	Introduction	63
4.2	Theory	63
4.3	Surface Fitting	64
4.4	Results	69
4.5	Conclusions and Future Work	74
5	PVDF Signal Simulations	75
5.1	Introduction	75
5.2	Previous Work	75
5.3	Relaxation Method Simulation	78
5.4	Results	79
5.5	Conclusions and Future Work	90
6	Conclusions	93
	Bibliography	96

Tables

Table

2.1	Sensitivities of the detector electronics on the beamline.	22
2.2	Statistics and rates of particles accelerated by CCLDAS dust accelerator.	34
4.1	Initial guess for parameters of surface to be fit. z_m is the measured surface of the crater and radius is the measured radius of the crater from chapter 3	66
4.2	Fit parameters and 95% confidence bounds for those fits	72

Figures

Figure

- 1.1 Picture of Apollo 17 astronaut Gene Cernan's lunar suit on display at the National Air and Space Museum in Washington, D.C. Despite efforts to clean the suit prior to re-entering the lunar module, Gene Cernan was unable to remove dust from his spacesuit (Wikipedia contributors, 2015). 2
- 1.2 Composite picture of the NASA Mars Exploration Rover Spirit's deck. So much dust has collected on the solar panel that it almost blends into the dusty background (Webster, 2008). 2
- 1.3 An image of the Student Dust Counter, a PVDF dust instrument launched aboard the New Horizons spacecraft to Pluto(Szalay et al., 2013) 6
- 2.1 Mass and velocity ranges of particles accelerated by various common techniques (Auer, 2001; Fechtig et al., 1978). 11

- 2.2 IMPACT dust accelerator. The Pelletron on the left side creates the 3 MV potential difference through a chain induction system that works similarly to a Van de Graaf machine. The dust particles start off in a source inside the Pelletron, are charged and sent into the main acceleration tube. The accelerated particles are then sent through three detectors that measure velocity and mass in real time. A logic circuit uses this information to decide whether or not the particle is accepted and sends a signal to the deflector plates which deflect unwanted particles out of the beam path. The dust passes through a final detector (to verify the characteristics of particles that reach the target chamber) and then into the target chamber itself. 13
- 2.3 20 kV dust source. The reservoir holds dust and is pulsed between 0-20 kV relative to the extraction plate. The needle is held at the maximum potential of the reservoir. Dust grains that come in contact with the needle are ejected. 15
- 2.4 This shows the chain charging system of a pelletron (Davis, 2001). The inductor/supressor creates an electric field between them and the grounded pulley. The pulley is conducting so that when a pellet comes in electrical contact with the pulley you can consider the pulley and link to be a single conductor. As the link is rotated into the field, a charge separation occurs where negative charge is pushed onto the pulley making the link positively charged at the inductor. The link then leaves electrical contact while still in this field allowing the chain to transport charge to the terminal shell where it is pulled off by the pickoff pulleys. 18
- 2.5 Simulation of dust beam from dust source to entrance of accelerating tube calculated in SIMION. Red lines are equipotential lines spaced 2 kV apart. Inset shows exit of accelerating tube. a)The Einzel lens is off resulting in a beam in the inset that is diverging. b) Same simulation with Einzel lens at optimal voltage. Inset shows resulting beam to be collimated. Beams as small as 1 mm in diameter can be achieved. 19

- 2.6 Image charge detector. Image charge is induced on the inner conductor when a charged particle enters. This charge is detected using a charge sensitive amplifier and can be used to determine particle charge. Velocity is determined through time of flight, which can be done by a single detector or multiple detectors. 22
- 2.7 The charge sensitive amplifier circuit diagram. Signals run from left to right. This circuit has three stages, the CSA stage, the gain stage, and the buffer stage. The CSA stage converts the charge signal to a voltage signal, the gain stage multiplies the voltage by a factor of 10, and the buffer stage ensures that a 50Ω wire can be driven by the CSA circuit. 23
- 2.8 Typical signals from image charge detectors and gate output along beamline. Particle charge is proportional to signal height and velocity is determined by time-of-flight between the first and third detectors. The TTL (transistor-transistor logic) gate pulse shows where the electrostatic deflection plates are turned on and off, before the particle arrives and after the particle leaves. Each vertical black line signifies where the particle has reached in time. 25
- 2.9 Block diagram of the Particle Selection Unit. Detectors 1 and 3 are used to determine velocity through time of flight while detector 2 is used to determine charge. A delay generator is then used to output 6 delayed pulses when a particle reaches a user-selectable position behind the start of the third detector. The first two of these pulses are used to turn off and on a set of deflection plates that bend particles out of the beam path. The remaining 4 delays can be used for timing and data acquisition triggers. 27
- 2.10 Simulation of cross correlation between noisy signal and filter. a) A very noisy signal. The signal is in the same position as the ideal signal in b, but is essentially invisible to the naked eye. b) The ideal signal with no noise being added. c) The filter that is used to cross correlate with the noisy signal. d) The filtered signal, the buried signal is now very clear and obvious. 31

- 2.11 Density Distribution of velocity and mass of CCLDAS dust accelerator. Lines show theoretical maximum limit of the accelerator and the expected output of a particle with a SNR of 1 and are dependent on terminal voltage, which was 2.2 MV for this set. Due to the FPGA PSU, particles below the red line are now visible to our detection electronics. Mean velocity is 11.3 km/s and mean mass is 8.74×10^{-15} kg (See table 2.2 for more statistics). 33
- 2.12 Solid line with squares shows a SIMION simulation of voltage on the Einzel lens and the resulting spot radius. The three dashed lines show half the calculated FWHMs of images of the beam spot using a long integration camera (SBIG ST-237). Inset shows the image of best focus. 35
- 2.13 a) Hole in 7 μm aluminum foil used for ejecta detection from micrometeorite impacts. b) Crater in fused silica glass sample used for lunar retroreflectors. c) Lunar Dust EXperiment (LDEX) engineering model inside the LEIL target chamber. This particular instrument will only be used for testing and will not fly in space. d) LDEX flight model inside the LEIL target chamber. This particular instrument was delivered to NASA and flew aboard the LADEE mission in 2013. 38
- 3.1 Average velocity and diameter of impactors for the samples in this study. Each data point represents the average of around 400 impactors on a single sample. The error bars represent the standard deviation of the masses and velocities for each of the samples used in this study. 43
- 3.2 Sample images of craters found in PVDF. Diameters of craters were determined by manually selecting ten points on the rim of the crater and then performing a least squares fit of those points to an ellipse. The diameter is taken to be the average of the major and minor diameters. The depth was determined by 3D stereophotogrammetry. 43

3.3	a) Initial crater imaged at 0 degrees. b) Same crater imaged at 52 degrees. c) Crater imaged after initial stair pattern cut. d) A close up of the cross sectioned crater. e) Same crater after a thin layer of platinum is deposited. f) A view of the cross sectioned crater from directly above.	46
3.4	Two images of the same crater. The right image is taken at a 5 degree tilt compared to the left image.	49
3.5	Two images of the same crater where matching points found by the SWIFT and SURF algorithms are shown. Green crosses are good matches, red circles were matches that failed a fidelity criteria.	50
3.6	Two images of the same crater with epipolar lines drawn. Lines are color coded to show the same line across the two images.	50
3.7	Two images of the same crater with epipolar lines aligned. These epipolar lines were recalculated so are not identical to those in figure 3.6.	51
3.8	Two images of the same crater that have now been registered.	51
3.9	The two images from figure 3.8 are overlayed and the opacity of the top layer was reduced to 50%. Inside the crater, the disparity is the most obvious. On the surface, it is not clear there is any disparity.	53
3.10	Sample 3D reconstruction from two images. In the color map, cool colors represent lower depths.	54
3.11	a) 3D reconstruction of a crater shown in b and c with the depth profile measured from the cross section overlayed. Notice the two depth profiles are well matched. b) Cross section of the crater viewed at a 52° angle. c) Undamaged view of the crater, crater interior is visible. d) Cross section of a different crater. e) Same crater as d, interior is not visible. f) 3D reconstruction with depth profile overlayed. Notice in this case the profiles do not match.	54

- 3.12 Sample EDS measurement of a crater. The image is blurry due to the higher accelerating voltage required to make EDS measurements. Image resolution is not important since x-ray energy constitutes the measurement. 56
- 3.13 a) Crater diameter divided by particle diameter versus velocity. The red line is a least squares fit to $\frac{d_c}{d_p} = av^b$, the green line is the scaling law Eq. 2 from Poppe et al. (2010) multiplied by 10, and the black line is the scaling law Eq. 6 from Poppe et al. (2010) multiplied by 10. b) Crater depth divided by particle diameter versus velocity. The red line is a least squares fit to $\frac{f_c}{d_p} = cv^d$, and the green line is the scaling law Eq. 1 from Poppe et al. (2010); McDonnell and Sullivan (1991) using iron as the projectile. The black line is also Eq. 1 from Poppe et al. (2010) with olivine as the projectile material, which was mistakenly used in the simulation (Poppe, 2013). 57
- 3.14 The velocity of all particles was ≈ 6 km/s. This work used iron particles hitting a PVDF target. The Price et al. (2010) data used silica projectiles hitting an aluminum foil. The Kearsley et al. (2006) data used soda-lime glass projectiles on aluminum foil, and include punctures as well as craters. The Hörz (2012) data used aluminum particles hitting an aluminum foil. 60
- 4.1 a) Comparison of Gaussian and super Gaussian functions. A super Gaussian is a Gaussian where the absolute value of the displacement r is raised to a higher order than 2. b) Measured surface of an impact crater where the impactor had a velocity of 6.10 km/s and a radius of 126 nm. c) 2D Gaussian fit to the surface in a $(z = ae^{-\frac{x^2+y^2}{w^2}})$, a and w were fit parameters. d) 2D super Gaussian fit to the surface in a $(z = ae^{-\left(\frac{\sqrt{x^2+y^2}}{w}\right)^n})$, a , w , and n were fit parameters. The color scale is the same for b,c, and d. 66
- 4.2 a) The measured surface of the crater. b) The initial guess used to start the fitting code. c) The final fitted surface after running the fitting code. d) An example of a bad fit. This surface was obtained by fitting the surface to a Gaussian. 68

- 4.3 Comparison of goodness of fits of different crater surfaces. a,b) The measured surface and the best fit to the crater with the best goodness of all the measured surfaces. c,d) The measured surface and the best fit to the crater with a median goodness of fit. e,f) The measured surface and best fit to the crater with the worst goodness of fit. Here it appears the code fit to a local minima instead of the entire crater. 70
- 4.4 a) The surface measured from the PVDF sample shown in 3D with lighting. The impactor had a velocity of 6.10 km/s and a radius of 126 nm. b) The measured surface as a colormap. c) The fitted surface in the same lighting as a. d) The fitted surface as a colormap. Fitted parameters are $a = -0.364$, $w = 0.1567$, and $n = 5.5636$. As you can see the fit compares quite well with the measured surface. 71
- 4.5 Equation for fitting used was $p = \alpha v^\beta$ where p is the parameter to be fit. Vertical error bars were plotted only in cases where there were more than 5 measured crater surfaces to fit parameters to. Otherwise the vertical error bar is missing due to the fact that there is no good estimate of the error. a) Fit for parameter a, crater depth. Fit equation is similar to measured depth scaling law in section 3.3. b) Fit for parameter w, crater radius. Good agreement with the diameter scaling law measured in section 3.3. c) Fit for parameter n, crater curvature. Suggests that as velocity increases and/or size decreases, the hole is more cylindrical. 73
- 5.1 This shows potential contours for a 5 μm diameter crater and 10 μm depth crater. The shaded area represents PVDF material and the black lines are equipotential lines. Potential contours in the bulk of the PVDF are spaced evenly while near the surface the spacing is decreased to illustrate the fringing fields near the crater (Poppe et al., 2010). 77
- 5.2 The ratio of theoretical to experimental charge for (a) Simpson and Tuzzolino's theory, (b) an analytic approximation and (c) Poppe et al. (2010) (Poppe et al., 2010). 80

5.3	The ratio of theoretical to experimental charge showing simulation results from using the crater scaling law used in Poppe et al. (2010) and the crater scaling law measured in this work. The black pluses are using the crater scaling law measured in this work but using the theory from Simpson and Tuzzolino (1985).	81
5.4	Contour plots of the simulation data. Each of these plots shows a slice through the center of the crater. a) Initial potential guess, potential lines are spaced 1kV apart from -6 kV to 6 kV. Near the PVDF surface, starting at ± 6.5 kV, lines are spaced every 20 V. b) Permittivity of the simulation, shaded region is PVDF. c) Polarization of simulation, shaded region is PVDF. d) Final calculated potential, same contour lines as a.	83
5.5	Contour plots of the E fields and charge. a) Calculated electric field in the x-direction (notice the magnitude is at most 2 orders of magnitude smaller than in the z-direction). b) Calculated electric field in the z-direction. c) Charge density. . .	84
5.6	Comparison between simulation with updated crater scaling law and with a different relative permittivity. The trend continues in both datasets and does not appear improved at all by changing the permittivity.	85
5.7	Comparison between simulation with the original simulation using measured crater scaling law and same simulation with different polarization, and with different polarization and relative permittivity. Unfortunately the trend has not been fixed by varying polarization.	87
5.8	Simulation run with a 401x801 grid, resolution is quadrupled in z compared to figures 5.4 and 5.5 by doubling the number of z grid cells and doubling the number of cells the pvdf spans.	88
5.9	Original simulation results with measured scaling law plotted with simulation results with increased resolution in the z-direction. Resolution was increased by a factor of 4.	89

5.10	Simulation run with a 401x801 grid, and the crater is modeled as a super Gaussian based on the fitting parameters measured in Chapter 4. a) The permittivity of the simulation (looks identical to the polarization but with different color values). b) Final calculated potential of the simulation. c) Electric field in the Y-direction. d) Charge density.	91
5.11	Original simulation results with measured scaling law plotted with simulation results with super Gaussian shaped crater. The spurious dependence has been very slightly reduced, but otherwise the results appear similar.	92

Chapter 1

Introduction

1.1 Dust Research

Dust can be found just about anywhere, from inside a room, to the furthest reaches of the earth, to distant nebulae in outer space. Dust is defined as macroparticles anywhere from a few molecules to several micrometers in diameter. Originally it was seen only as a technical obstacle to space exploration and study. Dust particles damage spacecraft and experiments creating craters in optical surfaces and solar panels, damage electronics, coat surfaces, prevent vacuum seals, and are a general health hazard. It also caused ground based observation of space to appear hazy or unfocused. Figure 1.1 shows an image of Apollo 17 astronaut Gene Cernan's lunar suit which is on display at the National Air and Space Museum in Washington D.C. The suit is still covered in dust due to the difficulty in removing the dust. Astronauts tried their best to remove dust before re-entering the lunar module, but despite their efforts, the dust remained on the suit where it could eventually be inhaled by the astronauts causing a health hazard. Furthermore, Apollo astronauts discovered that seals in their lunar suits, such as the wrist locks, became hard to operate, visors were scratched badly enough to reduce visibility, and leak rates from the suits increased after operating in the lunar dusty environment (Wagner, 2006). The Spirit and Opportunity rovers on Mars use large solar panels in order to generate energy. These solar panels can become covered in dust (shown in figure 1.2) preventing the Sun's energy from reaching the rovers. The Mariner 4 spacecraft flew through a cloud of space dust in 1967. This dust cloud ripped away bits of insulation and even changed the craft's orientation in space (Phillips, 2007). Understanding the



Figure 1.1: Picture of Apollo 17 astronaut Gene Cernan's lunar suit on display at the National Air and Space Museum in Washington, D.C. Despite efforts to clean the suit prior to re-entering the lunar module, Gene Cernan was unable to remove dust from his spacesuit (Wikipedia contributors, 2015).

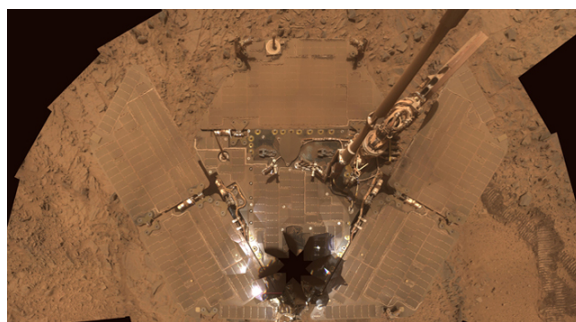


Figure 1.2: Composite picture of the NASA Mars Exploration Rover Spirit's deck. So much dust has collected on the solar panel that it almost blends into the dusty background (Webster, 2008).

properties and dynamics of dust, as well as their effects on materials, can help greatly in ensuring instruments, vehicles, and personal equipment remain in good working order, reducing the risk of missions failing, many of which can cost billions of dollars.

On the other hand, dust can also be used to gain insight on the inner workings of planets, moons, and galaxies. Dust can be collected like photons and analyzed for origins, trajectories, and composition. This information can be used in much the same way as photons in conventional astronomy for dust astronomy (Grün et al., 2002). In this manner, a new source of information is unlocked to unravel the mysteries of our universe. By studying dust grains and their properties like mass, velocity, and composition, in our solar system, it is possible to glean information about the origins of the solar system, dynamics and evolution of the solar system, and the composition of the different bodies of the solar system. The Cosmic Dust Analyzer (CDA) aboard the Cassini Spacecraft was able to determine that Enceladus, one of the moons of Saturn, has a subsurface ocean, and jets of this ocean near the south pole of Enceladus are the major source of ice particles in the E-ring of Saturn (Spahn et al., 2006; Postberg et al., 2009). Furthermore, determining the chemical makeup and trajectory of grains of dust will allow the mapping of the surface of Surface Bound Exospheres (SBEs) from orbit which can assist in asteroid mining operations, and determining the most scientifically interesting landing spot (Sternovsky et al., 2011).

While dust can provide a wealth of information to help shed light on the mysteries of our solar system, detecting this dust is difficult and expensive. Dedicated instruments such as CDA (Srama et al., 2004) and Dust Telescope (DT) (Sternovsky et al., 2011) are expensive and difficult to produce. In 1985, Simpson and Tuzzolino suggested the use of thin Polyvinylidene Fluoride (PVDF) films as dust impact detectors (Simpson and Tuzzolino, 1985). Since then, several space-bound instruments have used PVDF dust detectors including the Dust Counter and Mass Analyzer (DUCMA) instrument (Simpson et al., 1986) on Vega 1 and 2 to comet 1P/Halley, the High Rate Detector (HRD) on the Cassini Mission to Saturn (Srama et al., 2004), the Student Dust Counter (SDC) on New Horizons to Pluto (Horányi et al., 2008), the Dust Flux Monitor Instrument (DFMI) on the Stardust mission to comet 81P/Wild 2 (Kissel et al., 2004), the Space Dust (SPADUS)

instrument on the Earth orbiting Advanced Research and Global Observation Satellite (ARGOS) (Tuzzolino et al., 2005), and the Cosmic Dust Experiment (CDE) on the Aeronomy of Ice in the Mesosphere (AIM) mission in orbit around the Earth (Poppe et al., 2011). These types of detectors are capable of detecting a high flux of particles, they are lightweight, consume little power, and are relatively inexpensive. For example, large surface area ($\gg 1 \text{ m}^2$) PVDF dust detectors may be the best choice to monitor the spatial and temporal variability of interplanetary and interstellar dust fluxes reaching the surface of the Moon.

1.2 Laboratory experiments

To study dust in space, dust detectors are built on Earth and then launched into space. In order to understand the signals returned by these detectors, calibration of these detectors is necessary where the properties of the impactor are precisely known. These properties include the velocity, the mass, the size, the composition and more of the impactor, depending on the type of instrument being calibrated. For different instruments, this can mean different things. For example, a mass spectrometer such as CDA must be able to determine the different elements that compose the impactor. The signal size is dependent on the velocity and size of the impactor due to ion generation, as well as which elements are visible (Goldsworth et al., 2002). As such, the calibration requires impactors where the impactor material is precisely known and wide ranging, and the velocity and mass of the impactor must be known. This calibration can be achieved by means of a dust accelerator. This is a machine that can emit dust particles at high speeds (1-100 km/s) in a controlled way such that the chemical composition of the dust, the diameter of the dust, and the velocity of each particle that is emitted are known.

There are several methods of doing this including light gas guns, explosives, and electrostatic accelerators. An electrostatic dust accelerator takes a dust particle and charges its surface. The charged particle is then passed through a large voltage differential that accelerates the particle up to speed. The electrostatic method was chosen due to the fact that dust in space generally has a high velocity relative to the measuring instrument. Space dust can be ejected at velocities

greater than 100 km/s (Kempf et al., 2005). This velocity range is currently achievable only using electrostatic accelerators. The mass of the dust can vary, however, generally extends from $10^{-18} - 10^{-14}$ kg (Landgraf et al., 2000). This mass range also overlaps well with the impactors produced by an electrostatic accelerator. Furthermore, for very small particles, an electrostatic accelerator produces single particles instead of a “shotgun” spray. This is important for calibration as a shotgun spray would mean that precise information on each individual signal is unknown.

In addition to calibrating dust detectors, the accelerator is used to study impact related phenomena such as damage to materials, and ejecta. It was used to study damage in glass surfaces for the purpose of placing a new lunar retro-reflector on the moon (Currie et al., 2011). It was also used to study neutral gas species produced in hypervelocity impacts (Collette et al., 2014b) and charge yield in different materials (Collette et al., 2014a). There are many areas of study in the hypervelocity regime that are not well understood and so there are many areas of study that can be tackled using this accelerator. The accelerator will be used to study dust ablation, where a dust particle traveling at hypervelocity hits a wall of gas and ablates due to the frictional heating it experiences. This type of experiment will allow better understanding of radar data measuring the influx of micrometeors into Earth’s atmosphere (Janches et al., 2006) as well as the atmospheres of other planets. In this thesis, I describe the construction of a 3 MV electrostatic dust accelerator and its use in the study of crater formation in PVDF.

1.3 PVDF Detectors

PVDF detectors measure the flux of dust particles, but provide only limited information on the velocity and size of the impacting grains. An example of a PVDF detector is shown in figure 1.3. A PVDF detector is simply a thin piece of PVDF plastic, typically 28 μm thick, that is coated with a thin layer of aluminum and nickel on both sides. A charge sensitive amplifier (CSA) is connected across the two sides of the the PVDF. When a crater or hole is punched into the PVDF, a charge signal is created across the two sides which is measure by the CSA. There is no bias voltage required to run the instrument so in principle, the only power requirement for this detector is the

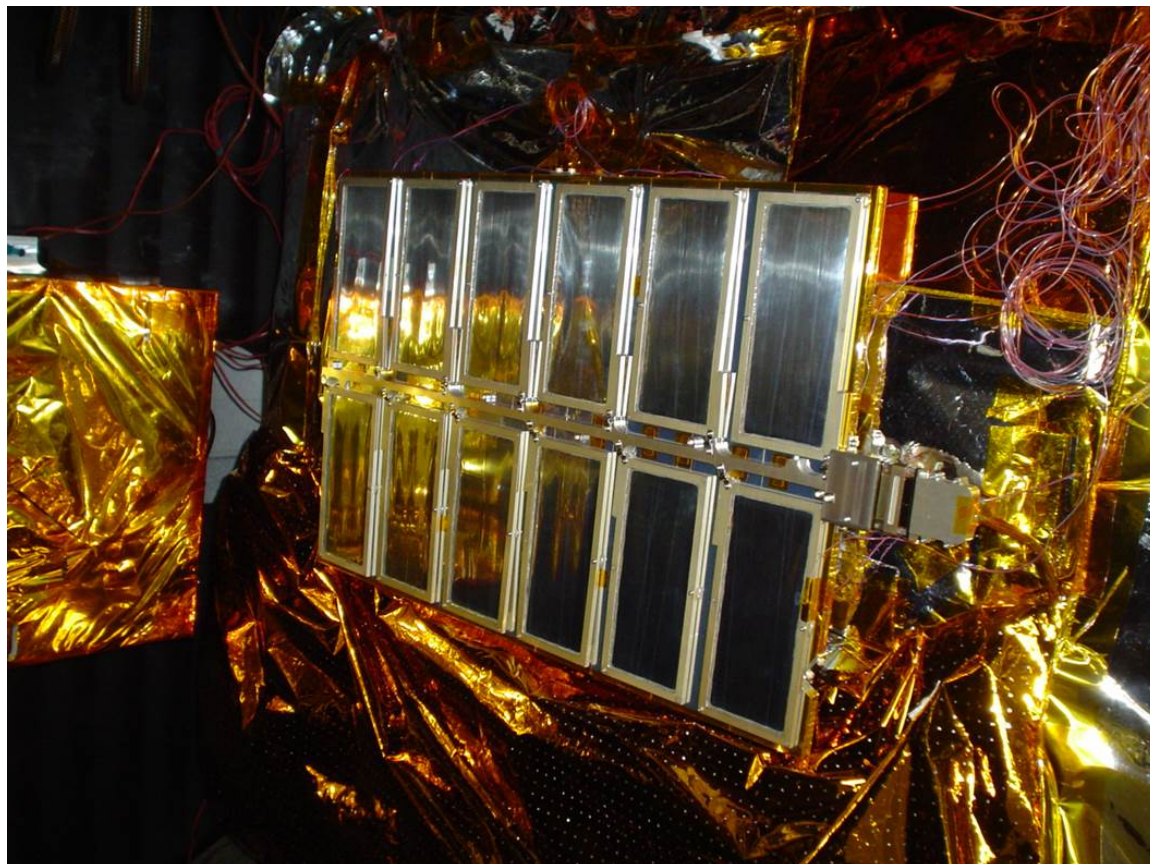


Figure 1.3: An image of the Student Dust Counter, a PVDF dust instrument launched aboard the New Horizons spacecraft to Pluto (Szalay et al., 2013)

power needed to run the charge sensitive amplifier electronics. The total weight of the SDC, is 1.6 kg and the average power consumption is 5.1 watts (Horányi et al., 2008). In comparison, the CDA instrument weights 16.36 kg and has an average power consumption of 11.70 watts (Srama et al., 2004). This means that SDC is 10 times lighter and uses a little less than half the amount of power of CDA.

The relationship of the magnitude of the depolarization charge produced from a PVDF detector and the properties of the impactor is not well understood. Two different theories have been proposed (Poppe et al., 2010; Simpson and Tuzzolino, 1985) that predict PVDF response based on impactor properties; however, each theory depends on the dimensions of the crater formed from the dust impacting on the detector. As such, the choice of crater size scaling law, the relation of impactor properties to crater properties, influences the result. Calibration of these dust detectors was done using an electrostatic accelerator. In Poppe et al. (2010), the scaling law used was adapted from a scaling law measured using aluminum impactors on aluminum targets. The results of the theory in Poppe et al. (2010) do not match the calibration data. It is believed that this may be due to the fact that the crater scaling law used was adapted from very different materials. Electrostatic dust accelerators typically use iron as an impactor material due to its ease of use, well-understood properties, and spherical shape, but a scaling law for iron impactors in PVDF has not been explicitly determined.

In order to determine a crater size scaling law relevant to the materials used in calibrating the instrument, I performed experiments using the 2 MV Van de Graaff dust accelerator at the Max-Planck-Institut für Kernphysik (MPIK) (Mocker et al., 2011) in Heidelberg, Germany using iron spheres of different diameters and velocities while the Colorado accelerator was being first commissioned. Craters formed by the impacts were analyzed using a Focused Ion Beam (FIB) and a Field Emission Scanning Electron Microscope (FESEM) located in the Nano-Characterization Facility (NCF) at the University of Colorado, Boulder. This thesis presents the building and development of an electrostatic accelerator, the methodology used to analyze crater depths and diameters from scanning electron microscope (SEM) images and present preliminary results. The

physics of the cratering process are discussed and the shape of craters is described. Simulations were carried out to better understand the depolarization charge in the PVDF and a review and analysis of cratering theory was performed to better understand the cratering process.

Chapter 2

The Accelerator

Analysis of interplanetary dust is useful for studying the origin and evolution of the universe. Similar to the use of photons in light astronomy, dust particle origins and evolution can be studied to gain a better understanding of the universe (Grün et al., 2005). On airless bodies such as the moon, dust may play a role in strange phenomena such as the high-altitude excess brightness seen on the horizon by the Apollo astronauts (Colwell et al., 2007). Dust also represents a technical obstacle to space exploration and experimentation. Dust in space can travel at very high velocities relative to spacecraft (many km/s). This dust can damage optical surfaces and solar panels, as well as puncture protective equipment. These high speed impacts occur in the hypervelocity regime, where the dust is moving faster than the speed of sound in the projectile and the target materials. The velocity at which particles are in the hypervelocity regime therefore changes depending on what the dust is made of and what it is hitting; however, the hypervelocity regime is generally considered to begin somewhere between 3 and 20 km/s for many materials. To calibrate dust instruments and to gain a deeper understanding of the impact processes involved, measurements of hypervelocity impacts under relevant and highly controlled conditions are required.

In order to study these and many other phenomena, dust accelerators have been used to simulate micrometeorite bombardment in a laboratory setting (Friichtenicht, 1962; Mocker et al., 2011; Hasegawa et al., 1999; Shu et al., 2012). The methods of launching hypervelocity dust include plasma accelerators, light gas guns, shaped explosive charges, and electrostatic accelerators. Plasma accelerators are plasma guns which use fast expanding plasma to launch particles from 1-30 km/s

(Ticos et al., 2006). Light gas guns work similarly. In a light gas gun, a combustion chamber is filled with combustible powder. By igniting this powder, gas expands and pushes a piston which compresses a light gas, typically hydrogen or helium. This gas is held inside a chamber with a diaphragm that is designed to burst once the pressure rises above a certain threshold. Sitting behind this diaphragm is the projectile to be launched, typically held within a sabot to ensure all of the built up pressure is used to launch the projectile. Once the pressure of the light gas increases beyond the failure point of the diaphragm, the diaphragm bursts, and the gas accelerates the projectile up to speeds of 10 km/s (Moritoh et al., 2001). Shown in figure 2.1 are the different possible ranges of projectile mass and velocity. The electrostatic accelerator has the ability to reach into the highest velocity regimes which are relevant to dust particles in space. Because of this, the method of acceleration used in the Colorado accelerator is electrostatic, where dust particles are charged and then passed through an electric potential difference, thereby accelerating them to high speeds. This method, described by Shelton et al. (1960), was pioneered by Friichtenicht (1962) with a 2 MV Van de Graaff accelerator. During this time, fear of damage from space debris drove several such accelerators to be built including the dust accelerator at the Max-Planck-Institut für Kernphysik (MPI-K) in Heidelberg, Germany (Rudolph, 1966). The electrostatic method offers several advantages. Generally, a light gas gun can only launch very small (<0.1 mm) particles in a spray where the individual velocity of each particle is not measured. The electrostatic method launches single particles where each particle is characterized that can be considered in ensemble as a “beam”. The ensemble properties of the dust beam can be controlled using standard techniques from ion accelerators, such as focusing using an electrostatic lens or beam steering using charged parallel plates. The main limitation of the electrostatic method is the inability to launch larger particle sizes.

After the Apollo era, the need for dust accelerators appeared to be diminished, resulting in the decommissioning of many facilities. Recently, many instruments, including the Cosmic Dust Analyzer (CDA) on the Cassini mission around Saturn (Srama et al., 2004), the Student Dust Counter (SDC) on the New Horizons Mission to Pluto (Horányi et al., 2008), and the Galileo Dust

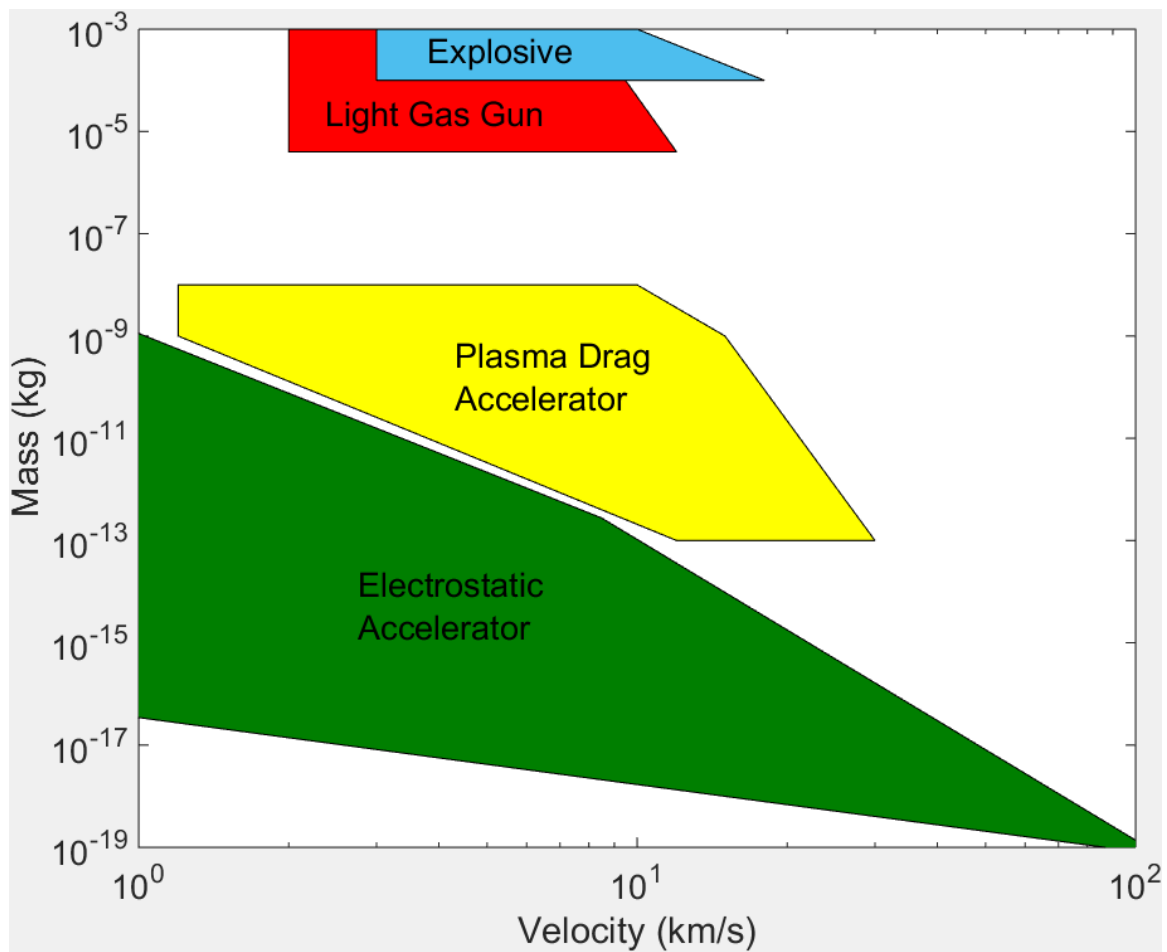


Figure 2.1: Mass and velocity ranges of particles accelerated by various common techniques (Auer, 2001; Fechtig et al., 1978).

Detector System (DDS) aboard the Galileo mission around Jupiter (Krüger et al., 2003), study dust and require controlled laboratory conditions for calibrations. In response, a 3 MV electrostatic hypervelocity dust accelerator has been built and tested at the Colorado Center for Lunar Dust and Atmospheric Studies (CCLDAS) which has now been renamed the Institute for Modeling Plasmas, Atmospheres, and Cosmic dust (IMPACT). This facility, based on the MPI-K accelerator, can be used to calibrate dust instruments such as the Lunar Dust EXperiment (LDEX) (Horányi et al., 2014) that flew aboard the Lunar Atmosphere and Dusty Environment Explorer (LADEE) in 2013-2014, as well as test material suitability to the harsh environment of space. Furthermore, basic plasma processes found in impact plasmas, such as ejecta distribution and composition, will be studied.

2.1 The Accelerator

2.1.1 Overview

The IMPACT accelerator is based on the MPI-K accelerator (Mocker et al., 2011). Shown in Figure 2.2, the dust starts off in a dust reservoir which charges the dust and injects it into the accelerating potential. The accelerating potential is maintained across an acceleration tube via a Pelletron chain. This acceleration tube is made up of metal potential rings separated by ceramic blocks to keep the potential difference falling linearly. Following the acceleration tube are two (originally three) image charge detectors (Srama and Auer, 2008) used to determine velocity and charge in flight in order to down-select particles that enter the target chamber. A pair of deflection plates follow, that direct unwanted particles out of the beam path. The deflection plates and its associated electronics that determine if a particle is within the acceptable velocity, charge, and/or mass window is collectively called the particle selection unit (PSU). A final detector is used to confirm the velocity and charge of particles that enter the target chamber.

Two interchangeable target chambers can be used at the end of the beamline. The main target chamber is the Lunar Environment Impact Laboratory (LEIL) test chamber, a 1.2 m diameter, 1.5

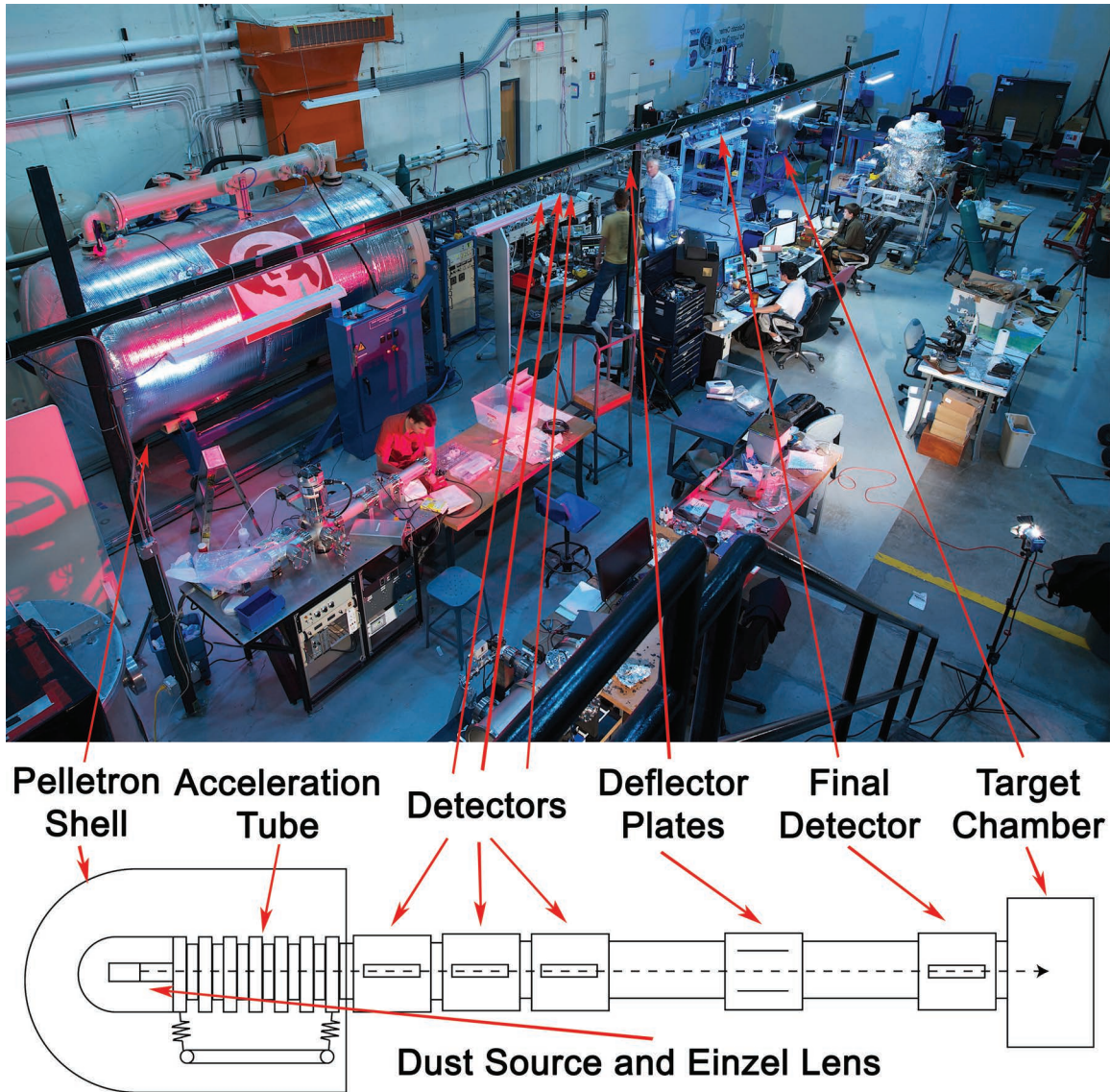


Figure 2.2: IMPACT dust accelerator. The Pelletron on the left side creates the 3 MV potential difference through a chain induction system that works similarly to a Van de Graaf machine. The dust particles start off in a source inside the Pelletron, are charged and sent into the main acceleration tube. The accelerated particles are then sent through three detectors that measure velocity and mass in real time. A logic circuit uses this information to decide whether or not the particle is accepted and sends a signal to the deflector plates which deflect unwanted particles out of the beam path. The dust passes through a final detector (to verify the characteristics of particles that reach the target chamber) and then into the target chamber itself.

m long cylindrical target chamber with over 30 ports for solar wind simulators, UV lamps, and electrical feedthroughs. This target chamber can be used to simulate the local environment in many regions in space, however can only be pumped to a pressure of 10^{-7} Torr. A second, 0.75 m diameter, 1.1 m long cylindrical UHV chamber is used for impact plasma studies. The UHV chamber is rated for pressures down to 10^{-10} Torr, and is designed for detection of trace elements and electrically neutral species in impact debris. A separate 20 kV accelerator consisting of just the dust source and two image charge detectors has also been constructed. This test stand is primarily used as a rapidly accessible test bed for different dust materials to be used in the large accelerator, however, it can also be used as a facility for slow speed (< 5 km/s) dust experiments.

The output of the accelerator is a “beam” of dust particles. This beam differs from laser beams or electron beams in that the beam is a collection of individual, non-interacting particles that are emitted at a non-constant rate, sometimes with several seconds between particles. The beam displays ensemble behaviors such as divergence and focusing; however, it does not have collective external or internal interactions. It can be characterized by its spot size or beam diameter, rate of individual particles, and pointing direction.

2.1.2 Dust Source

The beam starts inside a dust source housed inside the Pelletron shell. This source was designed after a unit in use at the MPI-K (Stübiger et al., 2001). Any particle material may be used as long as the surface is conducting to allow charging of the particle through contact. Metals, such as iron, are typically used due to the ease of charging, but materials such as gold-coated latex or silicates can also be used. A cross section of the dust source is shown in Figure 2.3. Dust is placed inside the reservoir, and after reaching high vacuum, the reservoir is pulsed between 0-20 kV relative to the extraction plate. The width, height, and frequency of these pulses provides coarse control over the physical characteristics (i.e. charge and velocity, but not size and mass) and rate of particles ejected from a mixed sample. A needle, held at the maximum voltage of the pulsing reservoir, is located at the center of the reservoir. When the reservoir voltage is low

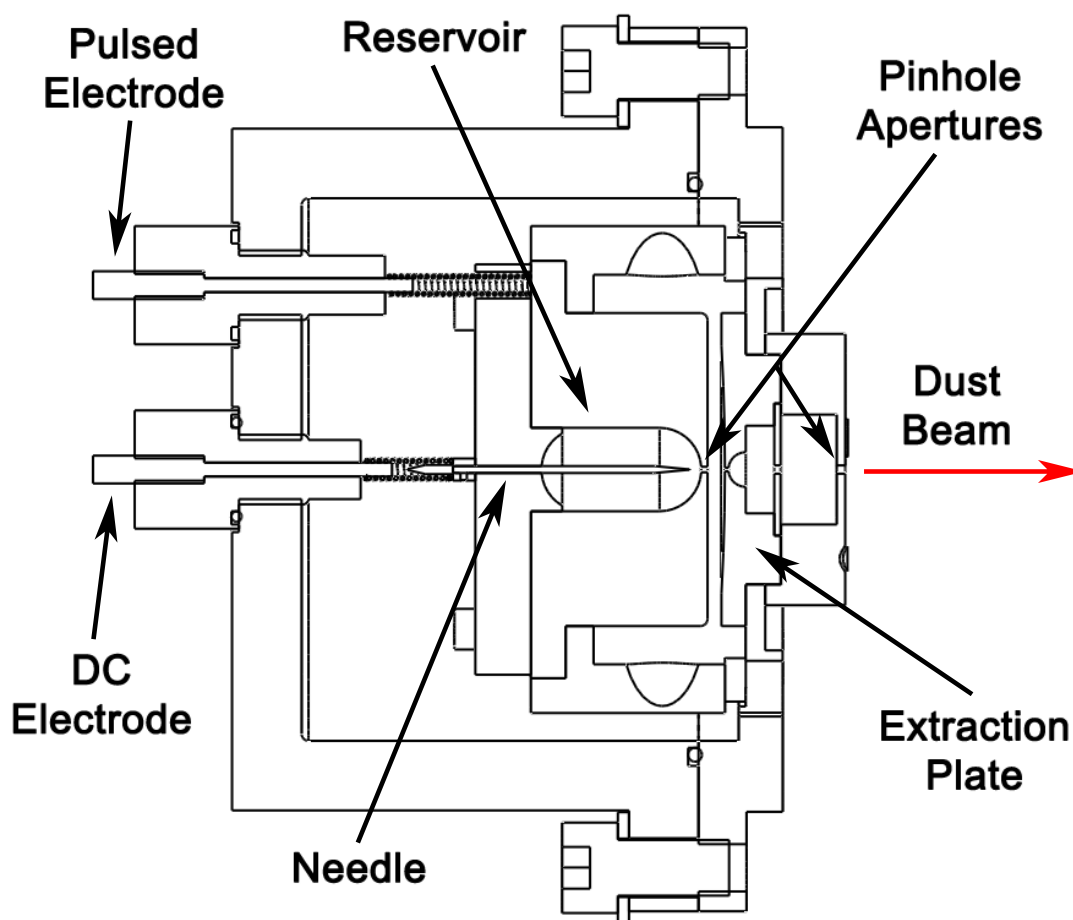


Figure 2.3: 20 kV dust source. The reservoir holds dust and is pulsed between 0-20 kV relative to the extraction plate. The needle is held at the maximum potential of the reservoir. Dust grains that come in contact with the needle are ejected.

compared to the needle, an electric field between the needle and reservoir induces a slight negative charge on the conducting dust. This allows the dust to levitate and become attracted to the needle. Whenever a dust particle contacts the tip of the needle, the particle becomes charged positively by contact or electron emission and is ejected by the electric field between the needle and the extraction plate (Mocker et al., 2011). This charging process is somewhat random and thus the charge and mass of the particles being ejected is not well controlled. The dust then exits through three concentric pinhole apertures in the reservoir, extraction plate, and outer shell, which collimates the pre-accelerated beam.

The magnitude of particle charging has several limits. Iron particles that are charged negatively will undergo field emission when the electric field strength reaches about 10^9 V/m (Shelton et al., 1960). By charging the particles positively, field desorption occurs at about 20×10^9 V/m (Müller, 1955; Paler et al., 1961). In fact, the choice to launch positively charged particles is due to the higher field emission limit of positive vs. negative charge. The charge, q , on a spherical particle given a surface electric field E of a particle can be calculated using Gauss' law to be

$$q = 4\pi\epsilon_0 E r^2 \tag{2.1}$$

where r is the particle radius and ϵ_0 is the permittivity of free space. Dividing by the particle mass, $m = 4\pi r^3 \rho / 3$, where ρ is the density of the particle, gives

$$\frac{q}{m} = \frac{3\epsilon_0 E}{r\rho}. \tag{2.2}$$

This shows that the particles with the largest charge-to-mass ratio are also the smallest and that for a given particle radius, the charge-to-mass ratio is limited. Particles also cannot be charged to a surface potential beyond the potential of the charging electrode. This places constraints on the total charge-to-mass ratio any single particle can have, thereby limiting the performance of the accelerator. The resulting impact on the operating space of the accelerator is discussed in section 2.2.

2.1.3 Focusing and High Voltage

The Pelletron charging system is similar to a Van de Graaff generator, which uses a moving belt to physically transport charge to a high-voltage terminal. The primary differences are that a chain of metal pellets connected by insulating links is used instead of a belt, and an inductive charge-separation system is used to charge the chain instead of a brush. Looking at figure 2.4, the system works by charging an inductor and suppressor to a negative and positive voltage, respectively, up to 50 kV. This generates an electric field pointed from the drive pulley, which is grounded, to the inductor. The pulley is conducting on all surfaces so that when a link is in contact with the pulley, it is electrically connected, creating a single conductor system. When a link passes into the field created by the inductor, a charge separation occurs where negative charge is pushed onto the pulley. This charge separation is maintained until the link no longer contacts the pulley leaving an individual link charged positively. This link is then transported to the terminal end where a pickoff pulley is used to pull some of the charge off onto another inductor to repeat the process this time bringing negative charge from the terminal to the drive pulley. A suppressor over the terminal pulley pushes all remaining charge onto the pulley which is connected through many large resistors along the potential rings of the pelletron to ground generating the high voltage. This series of potential rings, separated by ceramic blocks, is called the acceleration tube. The metal chain is more durable and does not generate any belt dust in the system. Furthermore, the metal can be charged to higher voltages enabling systems of 25 MV or greater (Jones, 1981). This system is housed inside a metal vessel which is filled with 6 atmospheres of SF_6 to prevent arcing. This is due to the fact that SF_6 has a much higher dielectric strength compared to air, about 2.5 times. Vacuum cannot be used as the required level of vacuum in order to suppress arcing at several megavolts would be difficult to achieve.

The entrance of this potential drop strongly focuses the charged particle beam, whereas the exit does not. This is due to the fact that particles are traveling slowly near the entrance and fast near the exit. This strong focusing leads to a highly divergent beam at the exit of the acceleration

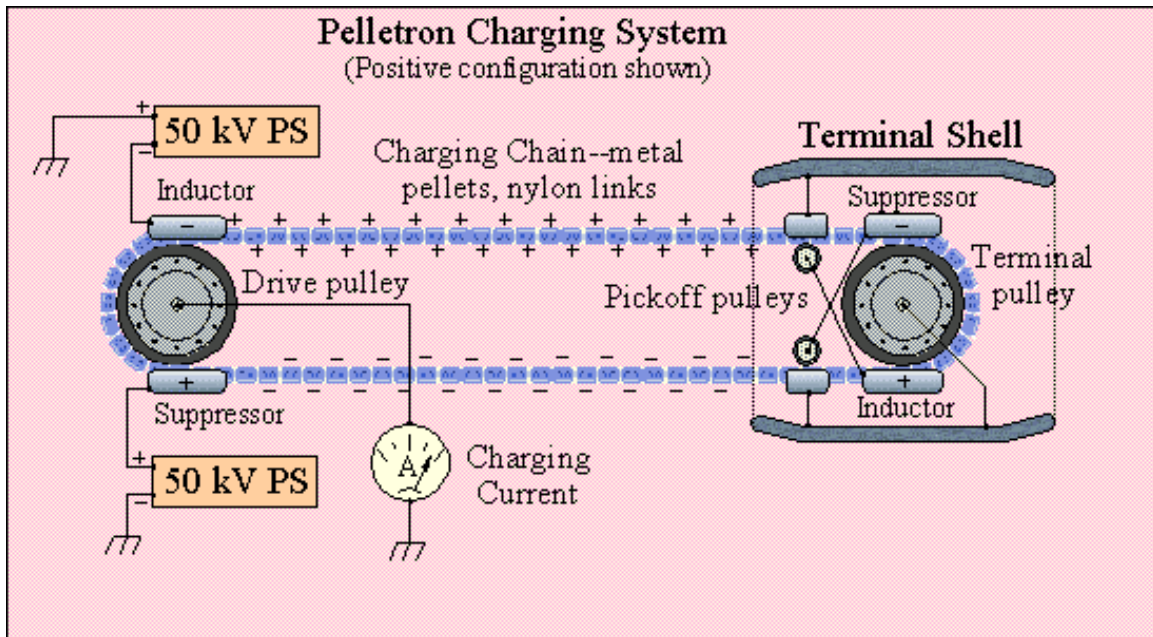


Figure 2.4: This shows the chain charging system of a pelletron (Davis, 2001). The inductor/suppressor creates an electric field between them and the grounded pulley. The pulley is conducting so that when a pellet comes in electrical contact with the pulley you can consider the pulley and link to be a single conductor. As the link is rotated into the field, a charge separation occurs where negative charge is pushed onto the pulley making the link positively charged at the inductor. The link then leaves electrical contact while still in this field allowing the chain to transport charge to the terminal shell where it is pulled off by the pickoff pulleys.

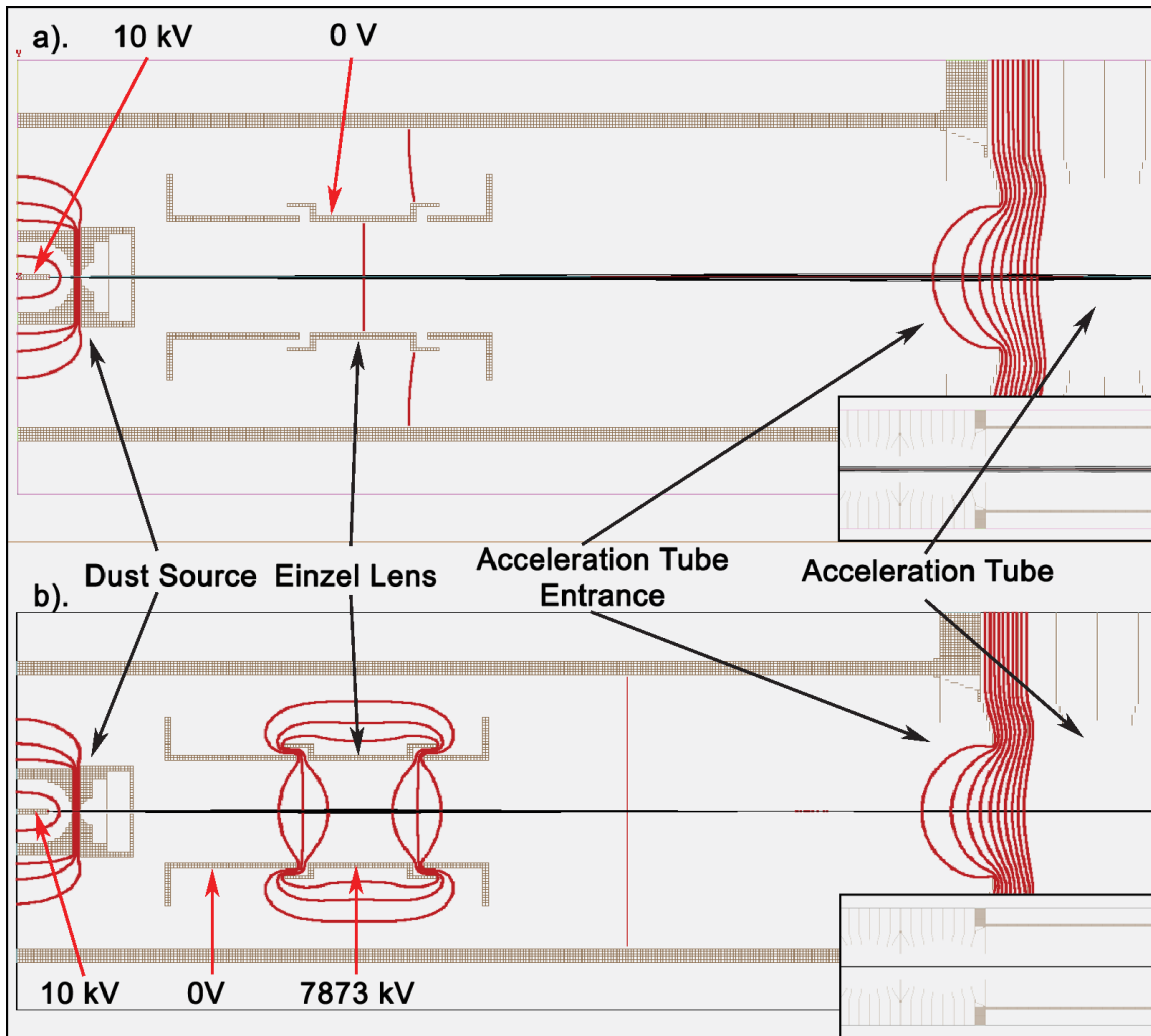


Figure 2.5: Simulation of dust beam from dust source to entrance of accelerating tube calculated in SIMION. Red lines are equipotential lines spaced 2 kV apart. Inset shows exit of accelerating tube. a) The Einzel lens is off resulting in a beam in the inset that is diverging. b) Same simulation with Einzel lens at optimal voltage. Inset shows resulting beam to be collimated. Beams as small as 1 mm in diameter can be achieved.

tube. To collimate this beam, an Einzel electrostatic focusing lens is placed between the dust source and acceleration tube. The lens is used to prefocus the beam so that a divergent beam enters the accelerating tube and is then collimated by the entrance of the acceleration tube.

The Einzel lens consists of three concentric inline cylindrical electrodes, only the center of which is charged to high-voltage. The outer two cylinders are kept grounded. This forms a saddle-shaped potential causing charged particles to be focused. SIMION, a charged particle optics simulation software package, is used to model the collective characteristics of the dust beam under different voltage conditions and determine the appropriate focusing voltage. As shown in figure 2.5a, the source produces a beam that becomes focused by the entrance of the acceleration tube. At the exit, this beam is diverging as seen in the inset. In figure 2.5b, the Einzel lens is set to the optimal voltage and the beam becomes prefocused so a diverging beam enters the acceleration tube entrance. The focusing of the entrance collimates the beam as seen in the inset. These simulations have shown that the theoretical dust beam diameter minimum is on the order of 1 mm.

2.1.4 Detectors and Particle Selection

Particle properties are detected in flight using a series of two image charge detectors, constructed from the MPI-K detector design (Srama and Auer, 2008). Originally 3 detectors were used. The first and third detectors were used to determine velocity and charge using time of flight and had a very high sensitivity. The second detector had a lower sensitivity to extend the dynamic range of measurement of the charge. If a signal saturated the electronics on detectors 1 and 3, then it would not on detector 2. This second detector has since been removed as particles that saturate the detector electronics are very rare. Each detector is composed of two grounded shielding cylinders and a central detection cylinder as shown in figure 2.6. When a particle enters the central cylinder, an image charge is induced onto the cylinder. The cylinder is narrow and very long compared to the end openings such that nearly all of the charge on the particle is induced onto the cylinder. The induced charge is detected using a charge sensitive amplifier (CSA) connected to the central cylinder through the CSA probe in figure 2.6. The amplitude of the signal is

proportional to the charge of the particle by a calibrated constant, and the velocity of the particle can be determined using time-of-flight between two detectors. A single detector can also be used to detect velocity, determined using time-of-flight from when it enters and exits the detector, and is used only as a check with the final detector to ensure particles entering the target chamber are the desired particles. From this information, the mass of the particle can be derived using the equation

$$\frac{1}{2}mv^2 = QU_p, \quad (2.3)$$

where m is the particle mass, v is the particle velocity, Q is the particle charge, and U_p is the accelerating potential of the Pelletron. The detectors are very sensitive to acoustic noise, and resonant vibrations can be excited in the detectors whenever vibrational energy is provided. Because of this, magnetically levitated turbo pumps and other vibration-damping hardware are used on the beamline to reduce vibrations. Since particle charge is related to signal height from the CSAs, particle detection is done through simple thresholding. If the output of the CSA reaches a certain level, a particle is detected. This level must be set above the acoustic and other noise sources in order to prevent false triggers.

The CSA circuit is shown in figure 2.7. The circuit consists of three stages. The first stage is the CSA stage where the charge signal is converted to a voltage. This is done using an Amptek A250 charge sensitive preamplifier. The signal is then passed through a band pass filter and then fed into the gain stage. The gain stage is simply a non-inverting amplifier circuit with a gain of 10. The signal is passed through another bandpass filter before entering the buffer stage. The buffer stage is a simple buffer amplifier that reproduces its input as identically as possible. This stage is to ensure enough power to drive the 50 Ω cables used in the lab. In order to calibrate these circuits, a very small but well known voltage pulse is applied onto a calibrated capacitor at the input of the circuit. This produces a current pulse with a total charge given by $Q = CV$, where Q is the charge, C is the capacitance, and V is the voltage. The output of the circuit is then read out and a sensitivity given in V/C is found. The sensitivities of the three detectors are listed in table 2.1.

A typical signal is shown in figure 2.8, and shows how the charge and velocity are measured.

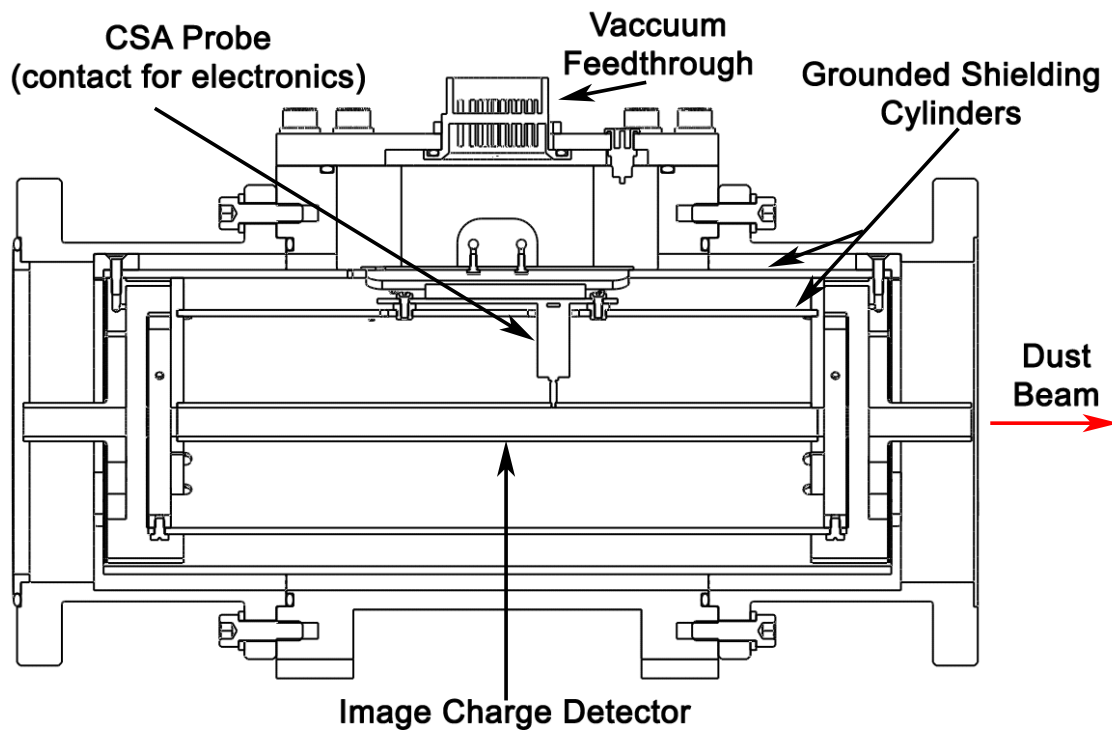


Figure 2.6: Image charge detector. Image charge is induced on the inner conductor when a charged particle enters. This charge is detected using a charge sensitive amplifier and can be used to determine particle charge. Velocity is determined through time of flight, which can be done by a single detector or multiple detectors.

Detector number	Sensitivity
1	$1.14 \pm 0.05 \times 10^{13} \text{ V/C}$
2	$1.24 \pm 0.02 \times 10^{13} \text{ V/C}$
3 (final)	$1.21 \pm 0.01 \times 10^{13} \text{ V/C}$

Table 2.1: Sensitivities of the detector electronics on the beamline.

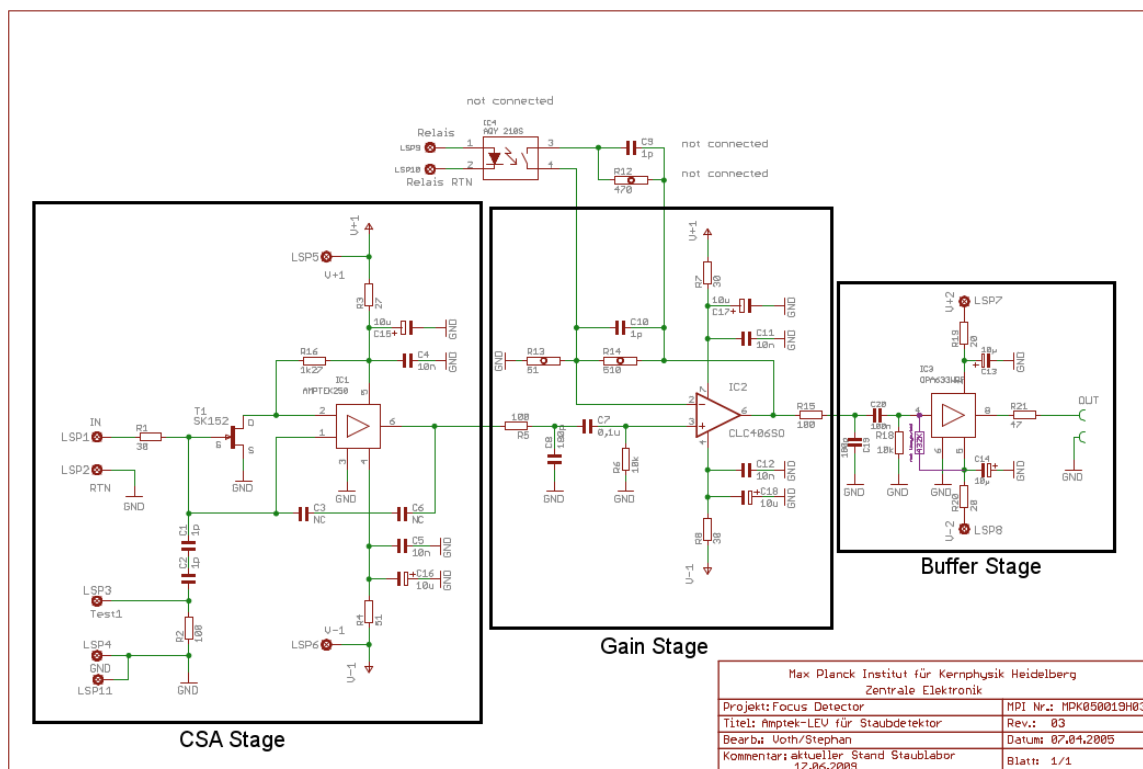


Figure 2.7: The charge sensitive amplifier circuit diagram. Signals run from left to right. This circuit has three stages, the CSA stage, the gain stage, and the buffer stage. The CSA stage converts the charge signal to a voltage signal, the gain stage multiplies the voltage by a factor of 10, and the buffer stage ensures that a 50 Ω wire can be driven by the CSA circuit.

When the square pulse on the first detector trace passes the threshold, it has entered the first detector tube. When the square pulse on the third detector trace passes the threshold, the particle has entered the third detector tube. By measuring the delay between these two times, the velocity is determined by time of flight. Once the velocity is known, the delay required to reach the beginning and the end of the PSU deflection plates is known, so the time required to open and close the PSU gate is known. Finally, the particle reaches the final detector signifying that the particle has entered the target chamber and will hit the target. These points are depicted in figure 2.8 by the black lines. The time scale for acoustic noise is large enough that the signals appear to sit on a DC offset (which have been removed in figure 2.8). This changing baseline still contributes to the noise floor as a simple threshold will still trigger from a changing baseline.

The fastest particles tend to have the smallest signals. According to Paler et al. (1961), the charge q , on a spherical particle of radius r , contacting a spherical electrode with radius R and charged to a voltage of V_p is

$$q = \frac{2\pi^3 \epsilon_0 V_p r^2 R}{3(R+r)^2}. \quad (2.4)$$

If $R \gg r$ then equation 2.4 reduces to

$$q = \frac{2\pi^3 \epsilon_0 V_p r^2}{3R}. \quad (2.5)$$

The mass of the particle is given by

$$m = 4/3\pi\rho_p r^3, \quad (2.6)$$

where ρ_p is the mass density of the particle. From Equation 2.3 it is clear that

$$v = \sqrt{2U_p \frac{q}{m}}. \quad (2.7)$$

Using equations 2.5 and 2.6 then

$$\frac{q}{m} = \frac{\pi^2 \epsilon_0 V_p}{2\rho_p R}. \quad (2.8)$$

Equations 2.7 and 2.8 show that $v \propto \sqrt{1/r}$. This means that the fastest particles are the smallest. Equation 2.5 shows that the smallest particles have the lowest charge, making them the most

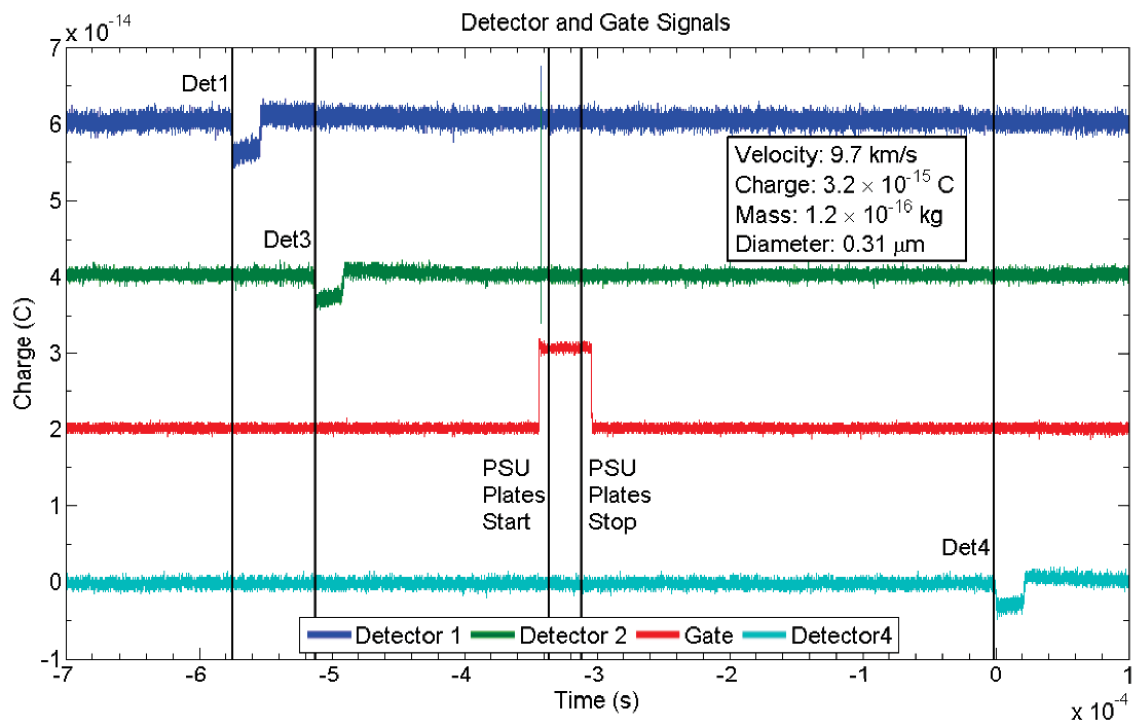


Figure 2.8: Typical signals from image charge detectors and gate output along beamline. Particle charge is proportional to signal height and velocity is determined by time-of-flight between the first and third detectors. The TTL (transistor-transistor logic) gate pulse shows where the electrostatic deflection plates are turned on and off, before the particle arrives and after the particle leaves. Each vertical black line signifies where the particle has reached in time.

difficult to detect. For example, a 100 nm diameter iron particle that has been charged to 1 kV potential will have 5.6 fC of charge and will be accelerated to 90 km/s. On the other hand, a 1 μ m diameter iron particle that has also been charged to 1 kV potential will have 56 fC of charge and will be accelerated to only 9 km/s. Notice that the charge is increased by an order of magnitude but the velocity is decreased by an order of magnitude.

If I combine equations 2.2 and 2.4, then the electric field at the surface of a particle charged by a spherical electrode is

$$E = \frac{\pi^2 V_p R}{6(R+r)^2}. \quad (2.9)$$

Looking at this I see that the best charging occurs when R is smallest, corresponding to as sharp a needle as possible. The potential of the electrode is given by

$$V_p = \frac{q}{4\pi\epsilon_0 R}. \quad (2.10)$$

By using equation 2.1 but replacing r with R I can get the relation of the maximum possible voltage that can be applied to the charging electrode,

$$V_{P_{max}} = R E_{Rm}, \quad (2.11)$$

where E_{Rm} is the maximum possible field intensity at the surface of the charging electrode (Paler et al., 1961). Replacing V_p in equation 2.4, I obtain

$$\left(\frac{q}{m}\right)_{max} = \frac{\pi^2 \epsilon_0 R^2 E_{Rm}}{2\rho r (R+r)^2}. \quad (2.12)$$

This equation tells us the maximum charge I can place on the particle given a spherical electrode. However, the maximum charge that a particle can hold is given by

$$q_{max} = 4\pi\epsilon_0 r^2 E_{rm}, \quad (2.13)$$

where E_{rm} is the maximum possible field intensity at the surface of the particle. If I now take equation 2.9 and replace E with E_{rm} and solve for V_p , then I obtain

$$V_{P_{max}} = \frac{6(R+r)^2 E_{rm}}{\pi^2 R}, \quad (2.14)$$

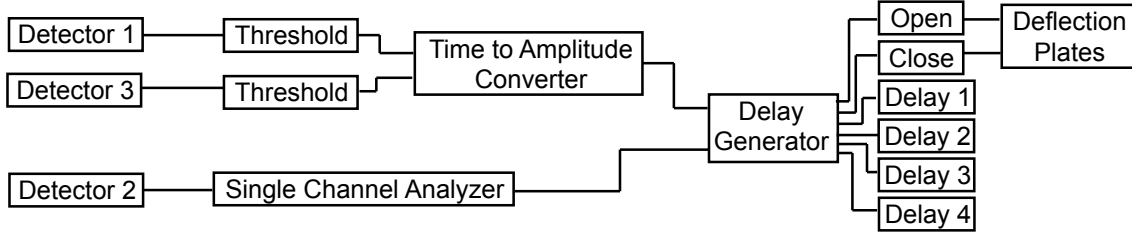


Figure 2.9: Block diagram of the Particle Selection Unit. Detectors 1 and 3 are used to determine velocity through time of flight while detector 2 is used to determine charge. A delay generator is then used to output 6 delayed pulses when a particle reaches a user-selectable position behind the start of the third detector. The first two of these pulses are used to turn off and on a set of deflection plates that bend particles out of the beam path. The remaining 4 delays can be used for timing and data acquisition triggers.

which is the maximum electrode potential needed to charge the particle to the maximum that it can hold. If I now take the ratio, $V_{P_{max}}/V_{p_{max}}$, and assume that $E_{Rm} \approx E_{rm}$ then, I get

$$\frac{V_{P_{max}}}{V_{p_{max}}} = \frac{\pi^2 R^2}{6(R+r)^2}. \quad (2.15)$$

By rewriting this equation as

$$\frac{V_{P_{max}}}{V_{p_{max}}} = \frac{\pi^2/6}{1 + 2(r/R) + (r/R)^2}, \quad (2.16)$$

I see that this ratio is one if $r/R = \pi/\sqrt{6} - 1 \approx 0.283$. This means that whenever $r/R \leq 0.283$ the contact charging is charging the particle to its maximum possible charge which means that this method of charging is effective for charging dust particles (Paler et al., 1961).

As the charge and mass distribution of particles from the source are broad, a particle selection unit (PSU) is used to analyze detector signals in real time to downselect individual particles before they reach the target. In this way, only particles within a user-selectable range of mass, energy, or velocity enters the target chamber. Figure 2.9 shows a block diagram of the PSU. Signals from detectors 1 and 3 are fed into a thresholding Schmitt trigger and the outputs are then sent as start and stop pulses to a time-to-amplitude converter/single channel analyzer (TAC). The TAC converts the delay between the start and stop signals into a voltage which it then compares to a user selected voltage window. If the voltage is within the window, it emits a TTL pulse. The

second detector output is fed into a single channel analyzer (SCA). If the voltage peak lies within a user selected voltage window on the SCA, then the SCA will emit a TTL pulse. If both the TAC and SCA output pulses (i.e. both the charge and velocity are within the desired ranges), a delay generator creates triggers with various delays corresponding to the arrival times of the particles at specific locations along the beamline. This method can only select particles based on their velocity and charge. Looking at equation 2.3, it is clear that selecting both velocity and charge is equivalent to selecting mass. This means, however, that in order to select mass, a velocity range must first be selected, and then a mass range can be selected via the charge selection.

Because the delay times are different for each particle (dependant on its velocity), a separate circuit was constructed to calculate the delay times. This circuit counts up the number of 10 MHz clock signals that fit in between the start and stop pulse, and then counts down to zero on up to six user-selected delay clock frequencies. The ratio of the user selected clock frequency and the 10 MHz clock determines the distance behind the start of the third detector that the delay generator will output a pulse. Each output pulse can be set independantly:

$$d_p = d_{det} \frac{f}{f_m}, \quad (2.17)$$

where f is the frequency of the delay clock, $f_m = 10$ MHz is the master clock frequency, d_p is the distance behind the start of the third detector the pulse is emitted, and d_{det} is the distance between the start of the first and third detectors. The first two of these delays are used to control an electrostatic deflector gate which consists of two parallel plates held at a potential difference of 6 kV. The first delay signal determines the start of a TTL pulse and the second delay signal determines the end. The resultant TTL signal grounds the deflection plates when a desired particle reaches 10 cm in front of the plates and charges them when the particle has reached 10 cm behind the plates. In this way, only particles that are selected can enter the target chamber. The other four delay signals can be used to trigger experiments and data acquisition systems anywhere in the beamline behind the third detector.

This 6 kV deflection plate is sufficient to bend all the particles out of the beam path regardless

of the velocity or charge of the particle. To see this, the electric field generated by the two plates is given by

$$E_p = V_p/s, \quad (2.18)$$

where $V_p = 6$ kV is the potential across the two deflection plates and $s \approx 5$ cm is the separation between the plates. The force on a particle is this electric field times the charge on the particle. The time that this particle is in this field is given by

$$t = l/v, \quad (2.19)$$

where v is the velocity of the particle and l is the length of the plates. Since the acceleration on the particle is the force applied on the particle divided by the mass of the particle, the acceleration is given by

$$a = \frac{qE_p}{m} \quad (2.20)$$

$$= \frac{qV_p}{sm}. \quad (2.21)$$

Now replacing m using equation 2.3 I get

$$a = \frac{qV_p v^2}{s2qU_P}. \quad (2.22)$$

This means the deflection that the particle gets is

$$\delta y = at^2/2 \quad (2.23)$$

$$= \frac{qV_p v^2}{4qU_P s} \frac{l^2}{v^2} \quad (2.24)$$

$$= \frac{V_p l^2}{4U_P s}. \quad (2.25)$$

This deflection sets the angle at which the particle leaves the plates, given by

$$\tan(\theta) = \delta y/l = \frac{V_p l}{4U_P s}. \quad (2.26)$$

This equation shows that this angle only depends on the accelerating voltage of the Pelletron, the voltage across the deflection plates, the length of the deflection plates, and the separation of the

deflection plates, none of which are properties of the particle being deflected. This means that all particles will be deflected by the same amount regardless of how fast or how large the particle is. A shield is set after the deflection plates that prevent particles from continuing down the beamline unless they are within the 1 cm opening of the last detector. Interestingly, prior to the installation of this shield, some dust particles were actually entering the target chamber by going around the detection tube. This was discovered when calibrating the LDEX instrument.

2.1.5 Second Generation PSU

Because the fastest and rarest particles have the lowest charge, an effort was undertaken to reduce the noise floor of the image-charge detectors, which will effectively increase the upper limit of usable particle velocities. A new particle selection unit that actively filters the signal using a field programmable gate array (FPGA) was designed and tested for this purpose. Since the expected signal shape is known, real-time running cross-correlation with a digital filter can be performed to extract particle information for signals that are ordinarily lost within the background noise. Figure 2.10 shows a simulation of the real time filtering performed by the FPGA. Figure 2.10a shows a signal lost in noise, b shows the ideal signal within that noise, c shows the shaped digital filter, and d shows the output of a running cross correlation of noisy signal and the filter. This shows that an essentially invisible signal can be made clearly visible through the clever choice of filter. By using two detectors, the velocity of these particles can be determined by time-of-flight between the clear, filtered peaks. The maximum of the correlation is proportional to the product of the velocity and the charge. As such, charge information can also be derived. This procedure is applicable to any signal so long as the signal shape is known. A full description of this new PSU is given in Thomas et al. (2013).

This work significantly reduced the noise floor for our signals giving access to a range of particles previously not possible. Computer simulations suggests a reduction in noise by a factor of 5. Furthermore, the FPGA implementation of the PSU allows more complicated particle selection such as pure mass selection, which the previous version did not. The old particle selection unit can

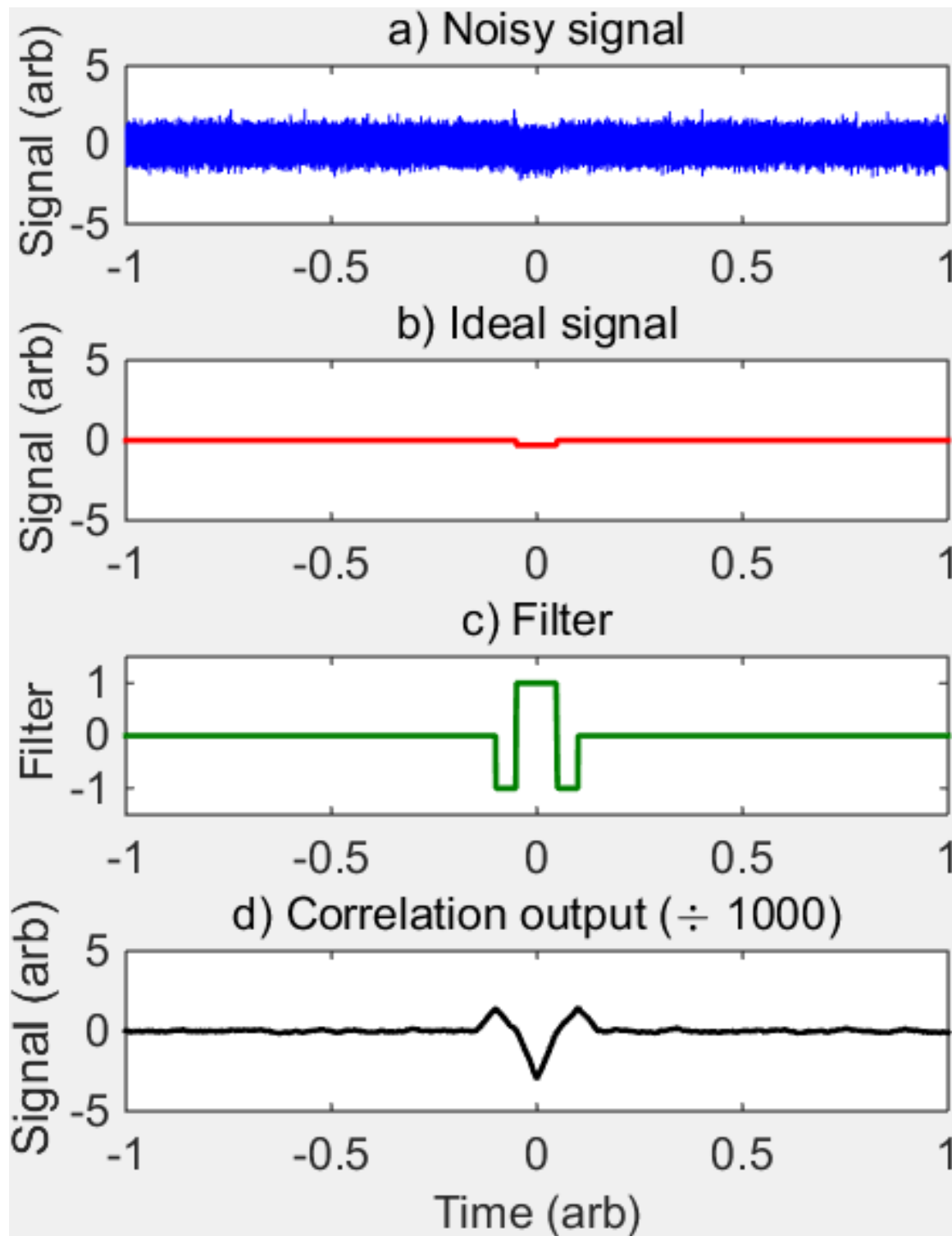


Figure 2.10: Simulation of cross correlation between noisy signal and filter. a) A very noisy signal. The signal is in the same position as the ideal signal in b, but is essentially invisible to the naked eye. b) The ideal signal with no noise being added. c) The filter that is used to cross correlate with the noisy signal. d) The filtered signal, the burried signal is now very clear and obvious.

only select particles based on mass by first choosing a velocity range and then limiting particles by their charge. While this effectively limits the mass of a particle selected, it does not allow all particles of a given mass to be selected. An FPGA based PSU has the ability to select the mass of all particles by varying the required charge selected based on the measured velocity of the particle.

2.2 Results

The first shot of the IMPACT dust accelerator was on February 16th, 2011. Since then, dust particles with diameters ranging from 0.028-8.60 μm have been accelerated to velocities of 0.2-108 km/s. Figure 2.11 shows a velocity vs. mass plot of particles emitted from the accelerator. Two lines are plotted indicating a theoretical physical limit of the accelerator and the expected signal from noise from the electronics. These limits depend on the terminal voltage of the accelerator and threshold of the detection electronics. The green line represents the ion field emission limit and follows the equation

$$m = \frac{36\pi}{m\rho^2} \left(\frac{2U_p\epsilon_0 E}{v^2} \right)^3, \quad (2.27)$$

where E is the ion field emission limit which can be 10^{10} V/m, U_p is the potential of the Pelletron, and ρ is the mass density of the dust (Sternovsky et al., 2001). This limit represents the absolute upper limit to the velocity that a particle of a given mass can have, assuming the particle is spherical. If the electric field of the particle were to exceed this limit, the particle would begin emitting ions thereby limiting its maximum charge. At the upper reaches of the distribution, particles are charged very close to this limit. The red line represents the minimum detectable charge based on the threshold triggering of an oscilloscope and effectively limited by the detector noise level. This line follows the equation

$$m = \frac{2qU_p}{v^2}, \quad (2.28)$$

where $q = 1$ fC, the triggering threshold of the oscilloscope. Since the implementation of the FPGA PSU, it is now possible to beat this limit, hence the reason there are particles below the limit in figure 2.11. The mean velocity of particles accelerated is 11.3 km/s while the mean mass is

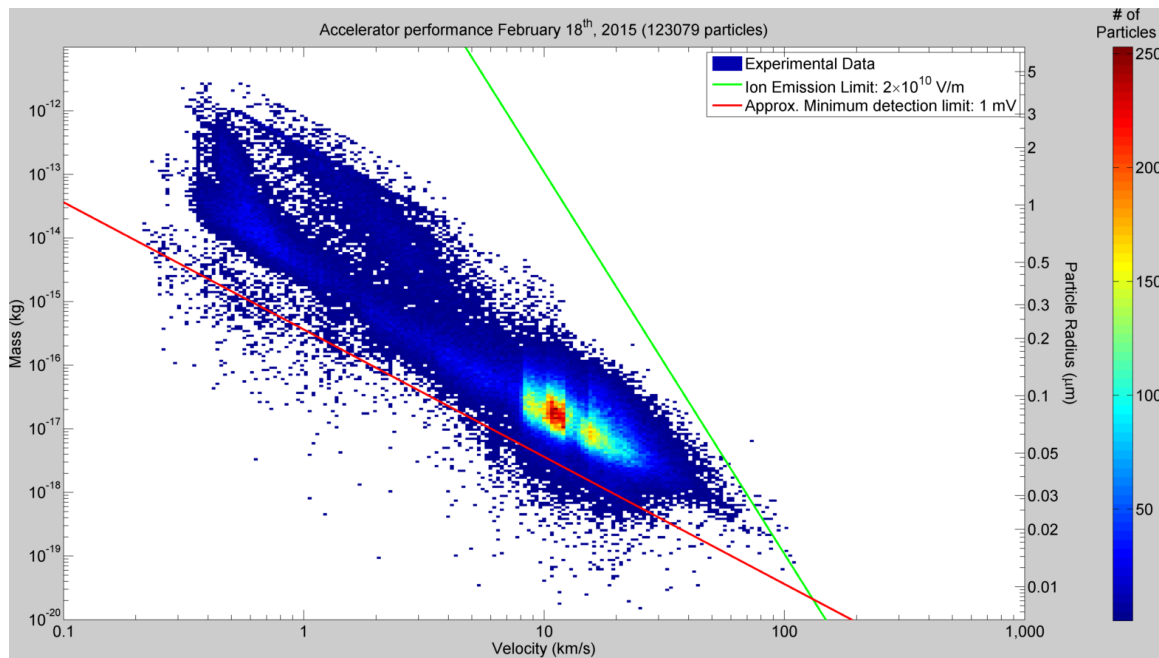


Figure 2.11: Density Distribution of velocity and mass of CCLDAS dust accelerator. Lines show theoretical maximum limit of the accelerator and the expected output of a particle with a SNR of 1 and are dependent on terminal voltage, which was 2.2 MV for this set. Due to the FPGA PSU, particles below the red line are now visible to our detection electronics. Mean velocity is 11.3 km/s and mean mass is 8.74×10^{-15} kg (See table 2.2 for more statistics).

Mean velocity	11.3 km/s
Max velocity	108 km/s
Standard deviation velocity	7.66 km/s
Mean mass	8.74×10^{-15} kg
Standard deviation mass	5.50×10^{-14} kg
Mean diameter	604 nm
Standard deviation diameter	1.81 (μm)
Fraction of particles above mean velocity	0.46
Rate of particles at mean velocity	1 Hz
Rate of particles above 20 km/s	< 1 Hz

Table 2.2: Statistics and rates of particles accelerated by CCLDAS dust accelerator.

8.74×10^{-15} kg. The rate at which the mean velocity of particles are accelerated is approximately 1 Hz. Approximately half of the particles are faster than the mean velocity. The rate of particles below 10 km/s is typically well above 1 Hz. Above 10 km/s, the rate tends to fall off depending on dust source depletion. This information is summarized in table 2.2.

The dust particle beam has also been characterized. Figure 2.12 shows results recorded 2.2 m from the exit of the Pelletron. A quartz target and camera were placed into the beamline prior to the first three image charge detectors. The dust impacting the quartz targets create weak light flashes that when integrated over several minutes, yield an image of the beam spot. By taking multiple images at different Einzel lens settings, it is possible to determine settings for best focus as well as beam characteristics at each setting. The smallest measured radius is 0.84 mm when the voltage on the central electrode of the Einzel lens is set to 8.82 kV. This result agrees well with the simulated value of 0.48 mm at an Einzel voltage of 8.8 kV suggesting that SIMION simulations accurately represent the beam. One possible cause for the small deviation is that the SIMION simulated beam has particles with a single charge to mass ratio, while the accelerator beam is made of particles with different charge to mass ratios. Further work will be done to measure the spot size and focusing settings at other points along the beamline.

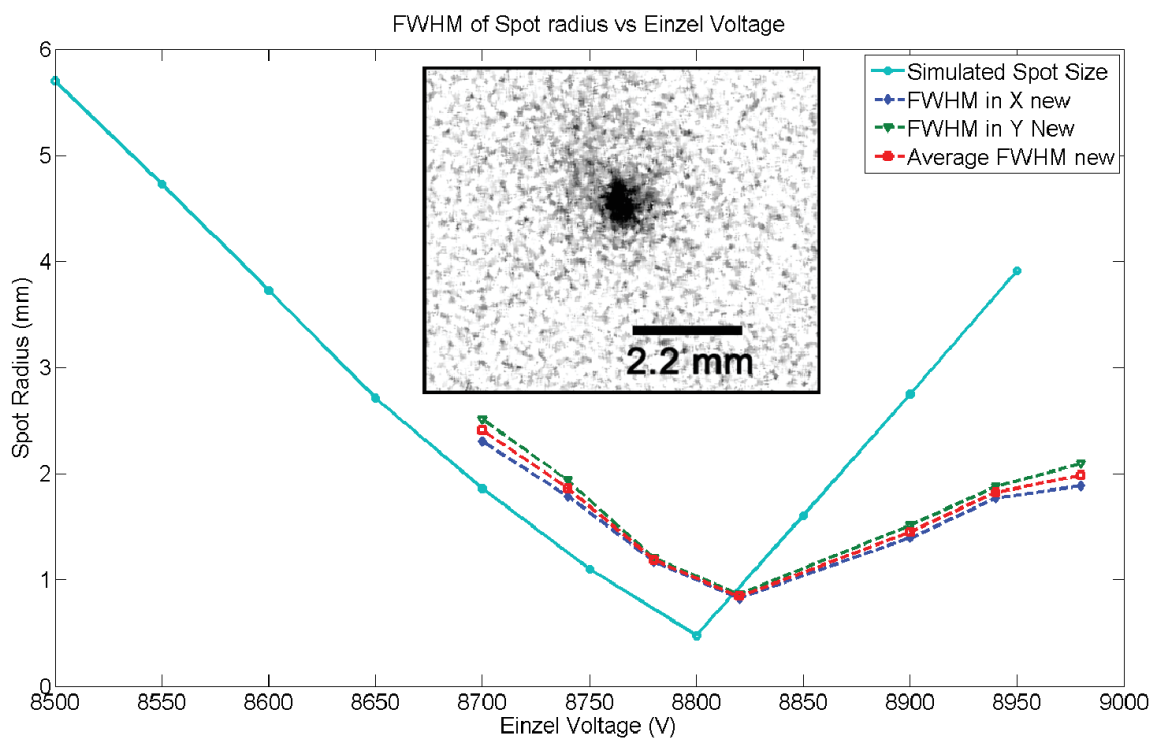


Figure 2.12: Solid line with squares shows a SIMION simulation of voltage on the Einzel lens and the resulting spot radius. The three dashed lines show half the calculated FWHMs of images of the beam spot using a long integration camera (SBIG ST-237). Inset shows the image of best focus.

2.3 Data Handling

The accelerator generates a lot of data that needs to be monitored in near real time. Because of this several systems have been setup to handle the large throughput of data to ensure that all data is recorded and analyzed. A MySQL database was created to store all metadata associated with the accelerator, including metadata on each individual particle recorded by the accelerator. The detector signals are recorded using two oscilloscope acquisitions cards from National Instruments and read into LabVIEW. Unfortunately, due to the high rate of particles being emitted by the accelerator, it is possible to generate data at a rate faster than it is possible to write to hard disk. In order to ensure that no data is lost, the accelerator saves data in several steps. First the data is recorded in memory in a queue by the LabVIEW data acquisitions program (called a vi) and an entry in the database is created. This memory queue is the only space where data can be written fast enough to keep up with the fastest rate data can be generated. Unfortunately, this space is limited so the rate must be controlled so this memory space is not filled. A separate vi then pulls the waveforms from this queue and writes them to hard disk as a raw waveform in labview format. This is done in order to ensure that waveforms are written to hard disk as fast as possible. Once this happens, it guarantees that I can always post process the signal even if something goes wrong in the data analysis chain. Ideally, the waveforms would be analyzed in real time to extract velocity and charge of the impactor. Unfortunately, this can only be done with very primitive thresholding techniques as more complicated techniques take too much computing power that slows down the data acquisition process.

Labview waveform files are hard to read and understand as they are in a proprietary format read only by LabVIEW. In order to convert these waveform files and analyze them, a separate vi is used to call a more complicated IDL routine to analyze these waveforms and rewrite them into the much more accessible HDF5 format. This IDL routine uses the same method as the FPGA based PSU to detect and measure particle properties. It filters the raw waveform signal by correlating the signal with several box shaped filters to extract the signal from noise (see section 2.1.5). Using

this routine it became possible to analyze signals well within the noise. Once the IDL routine has measured the velocity and charge, the MySQL entry is updated with these properties. A pointer is also included that allows the system to find where the waveform file is saved. This system was designed this way so that if the analysis routine is updated, then previous signals can be reanalyzed.

2.4 Current and Future Work

The accelerator has been used for several experiments. For example, a sample of 7 μm thick aluminized mylar foil was placed into the beamline to determine the possibility of using thin foils as a secondary ejecta detector for micrometeorite impacts. This experiment, shown in figure 2.13a is part of an ongoing experiment to determine the combination of thickness of a thin film and physical characteristics of an impactor that will cause the particle to crater, and when it will penetrate. This assists in determining the penetration limits of thin foils. Currently, polyvinylidene fluoride (PVDF) is the most interesting thin film material (Simpson and Tuzzolino, 1985). Due to its permanent dipole moment, cratering in PVDF will cause a charge increase (or decrease depending on which side of the PVDF is cratered) that can be captured as a voltage spike. The relation of the amount of material displaced, the physical characteristics of the impactor, and the amplitude of the charge signal is not well understood. This characterization will enable PVDF to detect mass and velocity of impacting particles. (Horányi et al., 2008). Due to the light weight and low power requirement, PVDF detectors can be added to many spacebound missions to collect data on the dust environment. Furthermore a large active area detector is more feasible using PVDF.

In another experiment, several samples of fused silica were placed into the beamline in order to characterize the damage and effect micrometeorites have on future lunar retroreflectors. The resultant craters were imaged using a scanning electron microscope (SEM) showing craters approximately 0.7-3 μm in diameter. Future work includes determining the depth of the craters seen in figure 2.13b. This is also part of an ongoing study to determine the ability of various materials to act as barriers to microparticles. Samples of carbon, stainless steel, tungsten, and molybdenum have also been exposed to the dust beam for this purpose. These particular samples will be useful

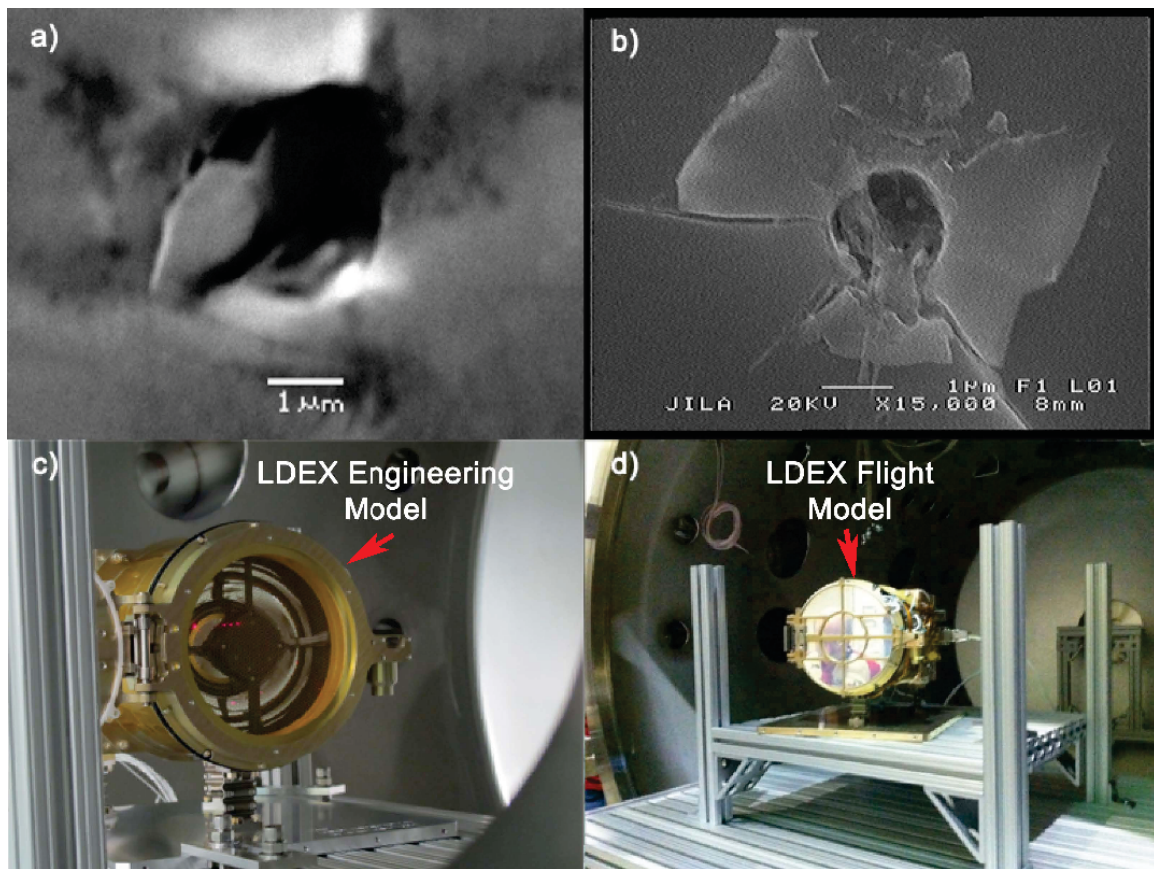


Figure 2.13: a) Hole in $7\ \mu\text{m}$ aluminum foil used for ejecta detection from micrometeorite impacts. b) Crater in fused silica glass sample used for lunar retroreflectors. c) Lunar Dust EXperiment (LDEX) engineering model inside the LEIL target chamber. This particular instrument will only be used for testing and will not fly in space. d) LDEX flight model inside the LEIL target chamber. This particular instrument was delivered to NASA and flew aboard the LADEE mission in 2013.

in determining the best wall tile material for nuclear fusion devices. Since fusion devices can generate a significant quantity of dust, and dust poses a danger in the fusion process (Krasheninnikov et al., 2011), it is important to determine which material will mitigate the creation of dust in these devices. This can easily be extended to materials for deployment in space. The constant micrometeorite flux poses a serious problem for solar panels powering equipment, glass windows on space vehicles and space suits, and fabric for space suits.

Calibration is a requirement for any instrument prior to being deployed in the field. For dust instruments bound for space, finding a controlled source of hypervelocity dust particles is difficult, so instruments such as LDEX require facilities such as the IMPACT accelerator. This provides a test bed so that obtained signals can be well understood, and theories to explain unexpected signals can be tested. The LDEX engineering model, shown in figure 2.13c, and flight model, shown in figure 2.13d, were partially calibrated at this facility. LDEX will characterize the lunar exospheric dust experiment and measure any spatial and temporal variability and impacts on the lunar atmosphere (Horányi et al., 2014).

Other planned experiments include light flash experiments, calibration of time-of-flight mass spectrometers such as the Large Area Mass Analyzer (LAMA) (Sternovsky et al., 2007), and detection of neutral particles generated by impact. Light flashes can be used to determine impactor characteristics such as mass and velocity (Eichhorn, 1975), or composition by detecting light spectra (Wanke et al., 2005) and have application in dust detection in space as well as defense applications on Earth. Neutral particle detection will provide insight into the impact process and evolution of planetary bodies. Other feasible studies include studying the effects of space weathering and planetary cratering.

In the next chapter, an experiment using a similar accelerator is described to measure the crater scaling laws of iron impactors on polyvinylidene fluoride targets.

Chapter 3

Cratering

3.1 Introduction

Simpson and Tuzzolino (1985) suggested the use of thin polyvinylidene fluoride (PVDF) films as dust impact detectors. Since then, several space-bound instruments have used PVDF dust detectors including the Dust Counter and Mass Analyzer (DUCMA) instrument (Simpson et al., 1986) on Vega 1 and 2 to comet 1P/Halley, the High Rate Detector (HRD) on the Cassini Mission to Saturn (Srama et al., 2004), the Student Dust Counter (SDC) on New Horizons to Pluto (Horányi et al., 2008), the Dust Flux Monitor Instrument (DFMI) on the Stardust mission to comet 81P/Wild 2 (Kissel et al., 2004), the Space Dust (SPADUS) instrument on the Earth orbiting Advanced Research and Global Observation Satellite (ARGOS) (Tuzzolino et al., 2005), the Cosmic Dust Experiment (CDE) on the Aeronomy of Ice in the Mesosphere (AIM) mission in orbit around the Earth (Poppe et al., 2011), and the Arrayed Large-Area Dust Detectors in INterplanetary space (ALADDIN) instrument on the Interplanetary Kite-craft Accelerated by Radiation Of the Sun (IKAROS) spacecraft Hirai et al. (2014). These types of detectors are capable of detecting a high flux of particles, they are light weight, and consume little power. For example, large surface area ($\gg 1 \text{ m}^2$) PVDF dust detectors may be the best choice to monitor the spatial and temporal variability of interplanetary and interstellar dust fluxes reaching the surface of the Moon.

PVDF detectors measure the flux of dust particles, but provide only limited information on the velocity and size of the impacting grains. The relationship between the magnitude of the charge produced from a PVDF detector and the properties of the impactor is not well understood.

Two different theories have been proposed (Poppe et al., 2010; Simpson and Tuzzolino, 1985) that predict PVDF response based on impactor properties; however, each theory depends on crater dimensions. A scaling law to establish a relation between the properties of the impactor and the crater remains to be experimentally determined. In order to calibrate these dust detectors, electrostatic accelerators are used as a source of dust grains with appropriate velocities (1-100 km/s). Electrostatic dust accelerators typically use iron as an impactor material due to its ease of use, well-understood properties, and spherical shape.

In order to determine a crater size scaling law, I performed experiments at the 2 MV Van de Graaff dust accelerator at the Max-Planck-Institut für Kernphysik (MPI-K) (Mocker et al., 2011) in Heidelberg, Germany using iron spheres of different diameters and velocities. Craters formed by the impacts were analyzed using a Focused Ion Beam (FIB) and a Field Emission Scanning Electron Microscope (FESEM) at the Nano-Characterization Facility (NCF) at the University of Colorado, Boulder. In this chapter, we discuss the methodology used to analyze crater depths and diameters from scanning electron microscope (SEM) images and present our results.

3.2 Experimental methods

3.2.1 Overview

I report on the experimental results using 24 samples of 52 μm thick PVDF film that were exposed to the dust beam at the MPIK accelerator. These experiments were performed in 2012, before the FPGA based PSU was completed on the IMPACT accelerator preventing the ability of precise mass and size selection. Each sample was exposed to a different impactor velocity and size range. Figure 3.1 shows the average velocities and masses of approximately 400 impactors on each target. The accelerator delivers particles in a large mass and velocity range which must be downselected to the range for each target sample. The range of sizes used on each sample were selected to balance the amount of time it would take to acquire 400 shots with getting as narrow a range as possible for each sample. Unfortunately it is not yet possible to track a single crater to

its impactor in the data so it is only possible to take averages of size ranges. Particle selection is achieved by detecting the mass and velocity in-flight and allowing only the desired particles to stay in the beam by grounding a pair of parallel plates held at high voltage (Mocker et al., 2011). After exposure to the dust beam, each of the 24 samples was inspected in the SEM, and a representative collection of craters were identified and analyzed. The two instruments used for analysis were the FESEM and FIB at the NCF. Crater dimensions are detected by 3D stereophotogrammetry, where 3D information is calculated by reconstruction techniques using two images taken at different viewing angles. Several craters were also cross-sectioned in order to test the validity of the 3D stereophotogrammetry technique.

3.2.2 Imaging using scanning electron microscopes

SEM imaging requires a conducting surface to prevent the buildup of a charge density on the sample so that the electron beam can reach the surface without deflection. Additionally, the release of gases from the exposed surface of a sample can lead to a decrease in signal due to interaction of the electron beam with the gas instead of the sample surface. This results in a loss of resolution in the image. In order to minimize these effects, a 40 nm gold layer was deposited onto each sample. The gold layer increased the contrast and resolution of each image allowing more detail to be visible within craters. However, using the gold layer results in a reduction in signal when using energy-dispersive X-ray spectroscopy (EDS) to analyze the chemical composition of the sample (see Sec. 3.2.5). Choosing a working distance for the image is also important. A small working distance increases the x-y resolution, but a large working distance increases the depth of field of the image. It is important to have a high x-y resolution so that small features can be resolved and used to rectify stereo pairs inside and outside of the crater. A large depth of field allows for a higher resolution of features at different depths, important in finding matching points within the craters for stereophotogrammetry. Figure 3.2 shows several sample images of craters taken in the FESEM. In some craters it is possible to image the bottom of the crater with high resolution, whereas for others, the bottom remains dark and unresolved.

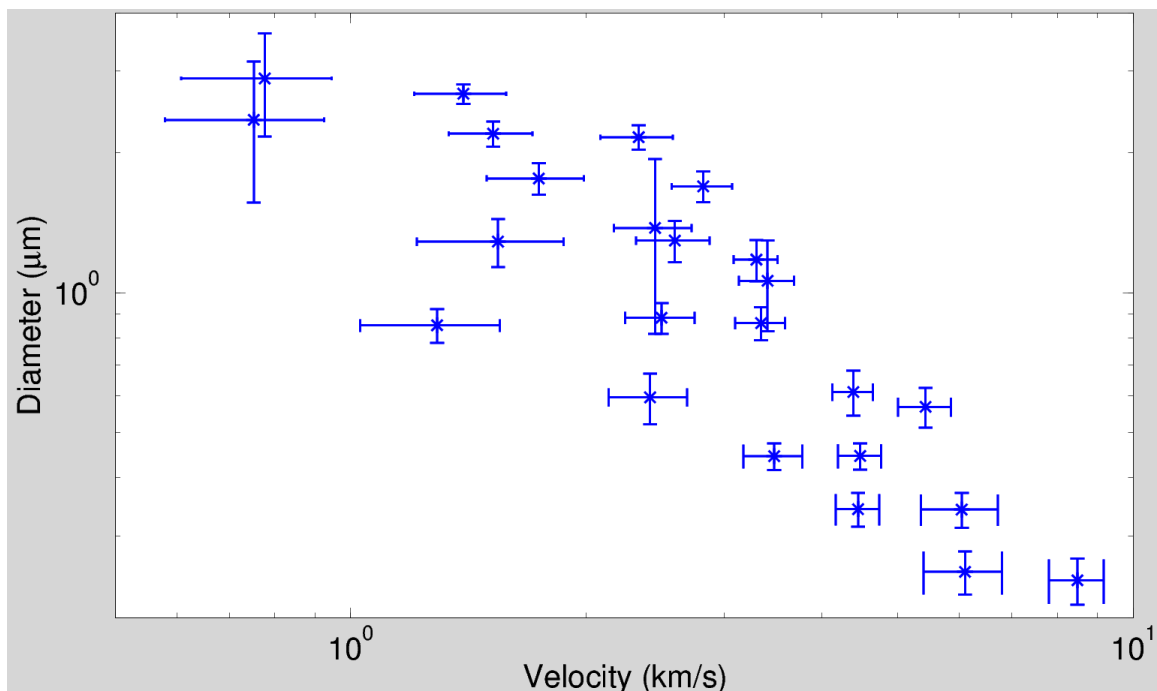


Figure 3.1: Average velocity and diameter of impactors for the samples in this study. Each data point represents the average of around 400 impactors on a single sample. The error bars represent the standard deviation of the masses and velocities for each of the samples used in this study.

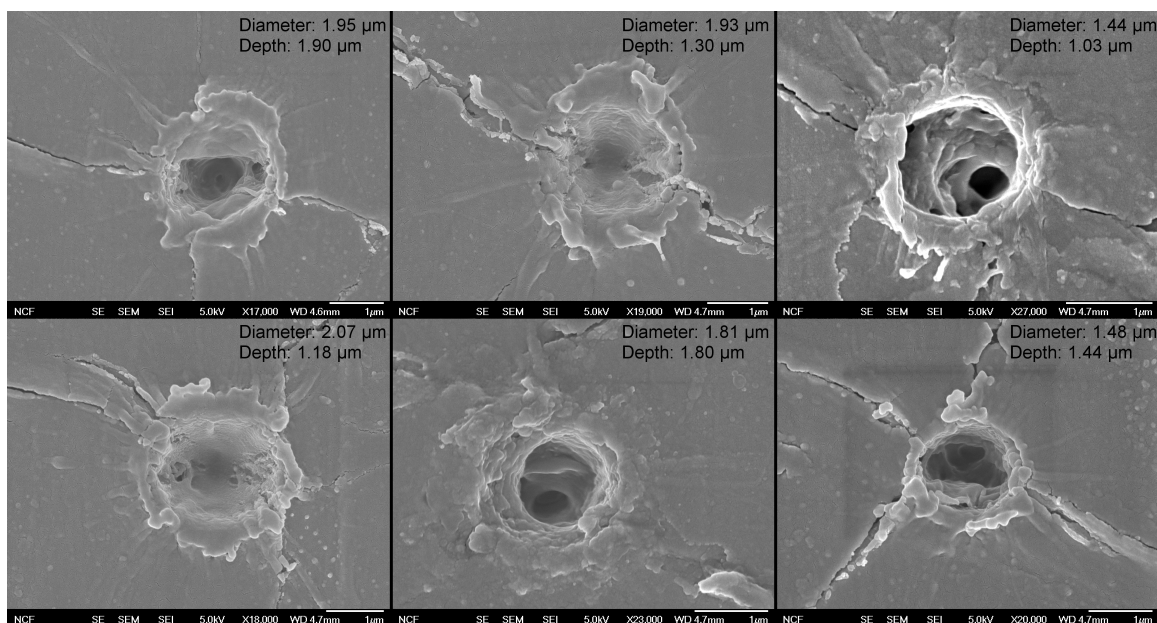


Figure 3.2: Sample images of craters found in PVDF. Diameters of craters were determined by manually selecting ten points on the rim of the crater and then performing a least squares fit of those points to an ellipse. The diameter is taken to be the average of the major and minor diameters. The depth was determined by 3D stereophotogrammetry.

Crater diameters were measured using the SEM images by manually selecting 10 points on the rim of the crater. A least squares method was used to fit an ellipse to the chosen points. The diameter was estimated as the average of the major and minor diameters.

3.2.3 Focused Ion Beam Cross Sectioning

A direct method of measuring depth is by physically cutting a cross section of each crater. This method allows one to see the complete profile of the crater and thereby know exactly how deep the crater is. A FIB is a device similar to an SEM but uses a focused beam of gallium ions instead of electrons. Due to the much heavier mass of gallium ions, the beam sputters away the material as it rasters across the surface. By controlling where the beam rasters, one can cut away material in a precisely controlled manner to create a cross section of the object. The FIB at the NCF is also equipped with an electron column to allow imaging using an electron beam. This reduces the damage done to the sample as searching for craters and coarse aiming can be done with the electron beam. The electron beam is aimed at the same spot as the ion beam but at a 52° angle.

The FIB at the NCF is also capable of depositing platinum by injecting methylcyclopentadienyl platinum trimethyl gas to the surface of the sample near the ion beam. The ion beam dissociates the gas into volatile components, which are sputtered away, and platinum, which is adsorbed onto the surface. The strength of the ion beam must be controlled. Too high an ion flux and the surface will sputter away faster than the deposition creating a cut, but too low an ion flux results in the platinum-rich gas to be wasted as too little of it is broken up and adsorbed onto the surface. Both of these processes are necessary to create a proper cross section of the crater in PVDF.

Figure 3.3 shows the process of creating a cross section. Figure 3.3a shows the initial discovery of the crater. The sample is then tilted to 52° as in Figure 3.3b to align it perpendicularly to the ion beam. A rectangular stair pattern hole that is at least twice as wide as its deepest point is cut into the sample approximately $1 \mu\text{m}$ away from the lowest point of the crater (Figure 3.3c). This stair pattern is made up of a succession of rectangular holes with the same width that are cut

deeper as it nears the deepest position of the crater. This is done to reduce the time needed to cut a hole deep enough to see the cross section using the electron beam. A final cleaning cut is then made to remove the remaining $1\ \mu\text{m}$ width of material to reach the perceived deepest position of the crater. This is done at a lower ion flux in order to preserve a sharp boundary at the crater. Figure 3.3d shows a close up of the crater after the final cleaning cut. The boundary of the crater is nearly invisible due to the fact that the PVDF material is non-conducting and results in low contrast. After depositing a thin layer of platinum seen in Figure 3.3e, the boundary becomes clear and the depth profile can be measured. Figure 3.3f shows the same crater imaged from directly above proving that the boundary is very sharp. Looking at Figure 3.3, parts a and c, a melt layer is clearly missing between the two images. This was an unintentional side effect when focusing the ion beam for cross-sectioning. In the future, it may therefore be more appropriate to deposit a thicker platinum layer to preserve the crater's shape and enhance contrast in the boundary after cross-sectioning. Finally, by measuring the boundary between the platinum and PVDF and correcting for the tilted viewing angle, a depth profile can be measured with high accuracy.

This method of depth measurement is advantageous because it is direct. Since the physical surface is being measured it in principle guarantees an accurate measurement of the full depth profile of the crater. Unfortunately it also suffers from several disadvantages:

- 1) This process is time consuming and requires a user to select and determine each cut and deposition. Each crater requires at least half an hour for cutting and depositing. This time must be added on top of the time required to search for each crater in a sample which can take anywhere between several minutes to several hours.
- 2) The measurement does not guarantee finding the deepest point in the crater since it can be difficult to determine the lowest point prior to cutting. As such, the position of the cut must be decided by the user prior to knowing the best possible place to cut. This can in principle be avoided by cutting and imaging several slices through the crater, however, the time requirement increases as the number of cuts increases.
- 3) Due to the much higher momentum of the ion beam, it is difficult to ensure the sample stays

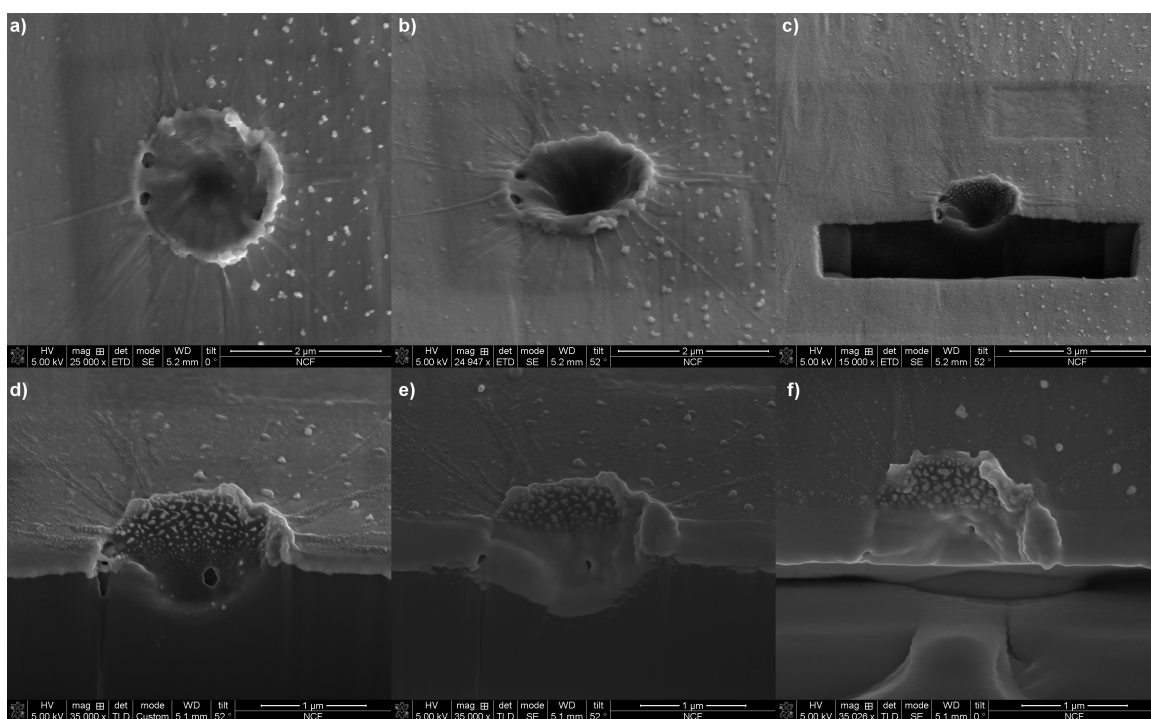


Figure 3.3: a) Initial crater imaged at 0 degrees. b) Same crater imaged at 52 degrees. c) Crater imaged after initial stair pattern cut. d) A close up of the cross sectioned crater. e) Same crater after a thin layer of platinum is deposited. f) A view of the cross sectioned crater from directly above.

unchanged prior to measurement, and it becomes impossible after the measurement. The reason for this is that a prerequisite to sputtering or depositing material is to focus the ion beam. This focusing must be achieved by scanning the beam across the target to be analyzed. Precautions are taken to minimize the sputtering caused by focusing; however, some sputtering is unavoidable. After cross-sectioning, the sample is destroyed and cannot be reused.

3.2.4 3D reconstruction using Stereophotogrammetry

An indirect measurement of depth can be achieved by creating a 3D reconstruction using stereophotogrammetry. This method is relatively quick compared to cross sectioning, approximately five minutes per crater, enabling the analysis of a larger number of craters. It involves taking two images of the same feature at different viewing angles and reconstructing the 3D position of each pixel by matching pixel points and calculating the disparity in position between matched pixels in the two images. This disparity map can then be translated into a depth map by a simple linear transformation.

This process can be broken into two steps. First the two images must be registered to allow numerical comparison between the two images. The second step is reconstructing the 3D model of the object through detection of the disparity in position between matching pixels in each image. The first step is done by taking advantage of the epipolar geometry of imaging a single 3D object from different viewpoints. Given a pixel q in the first image, epipolar geometry describes the constraint that the corresponding pixel in the second image, q' , must lie on a line called an epipolar line. To describe this geometry in computer vision, a matrix called the fundamental matrix is used. The fundamental matrix F can be determined by matching pixels between two images according to Luong et al. (1993). The epipolar constraint can be described by

$$l'_q = Fq \quad (3.1)$$

where l'_q is the epipolar line that q' must lie on. Since q' must lie on this line, then

$$q'^T Fq = 0 \quad (3.2)$$

Once the fundamental matrix is determined, a set of epipolar lines can be drawn across both images. In the case of tilted images in the SEM, the tilt axis never changes. Because of this, the epipolar lines are parallel to each other. By then lining up an epipolar line in the first image with its corresponding epipolar line in the second image, the two images become registered. The second step is done by using the two registered images and determining the disparity in position between matching pixels to form a disparity map. This disparity map can then be transformed with an affine transformation into an elevation map (Lane, 1969).

In order to carry out this process, a 3D reconstruction code written in Matlab by Routier-Kierzkowska and Kwiatkowska (2008) is used. Figure 3.4 shows two images of the same crater where the right image is taken at a 5 degree tilt compared to the left image. The code works by first finding matching subpixel features in both images using the SWIFT (Lowe, 2004) and SURF (Bay et al., 2006) algorithms. Figure 3.5 shows points in both images that are matching. In this image, 729 points were found that could be matched across the two images. The green crosses signify matches with high fidelity while the red circles signify matches with a lower fidelity. The code then determines the fundamental matrix by minimizing the left hand side of equation 3.2 for each of the matching features. Once the fundamental matrix is determined, the epipolar lines are calculated. These epipolar lines are shown in figure 3.6. These images show the epipolar lines on both images. The lines are color coded to more easily line them up across the two images. The code then aligns the two images such that when both images are placed side by side, the epipolar lines across the two images are continuous. This can be seen in figure 3.7. As we can see, now that the epipolar lines are aligned, matching features on both images fall on the same epipolar line and the images are registered. This reduces the pixel matching between the two images to one dimension. Each pixel in one image is then matched to a pixel in the second image and the disparity and the confidence of matching is calculated. To see this disparity, the registered images without the epipolar lines are show in figure 3.8. By finding common points on the two images it is possible to see that there is some disparity between some points and almost none in other points. To make this more obvious, figure 3.9 shows the right image overlayed onto the left image with 50% opacity.

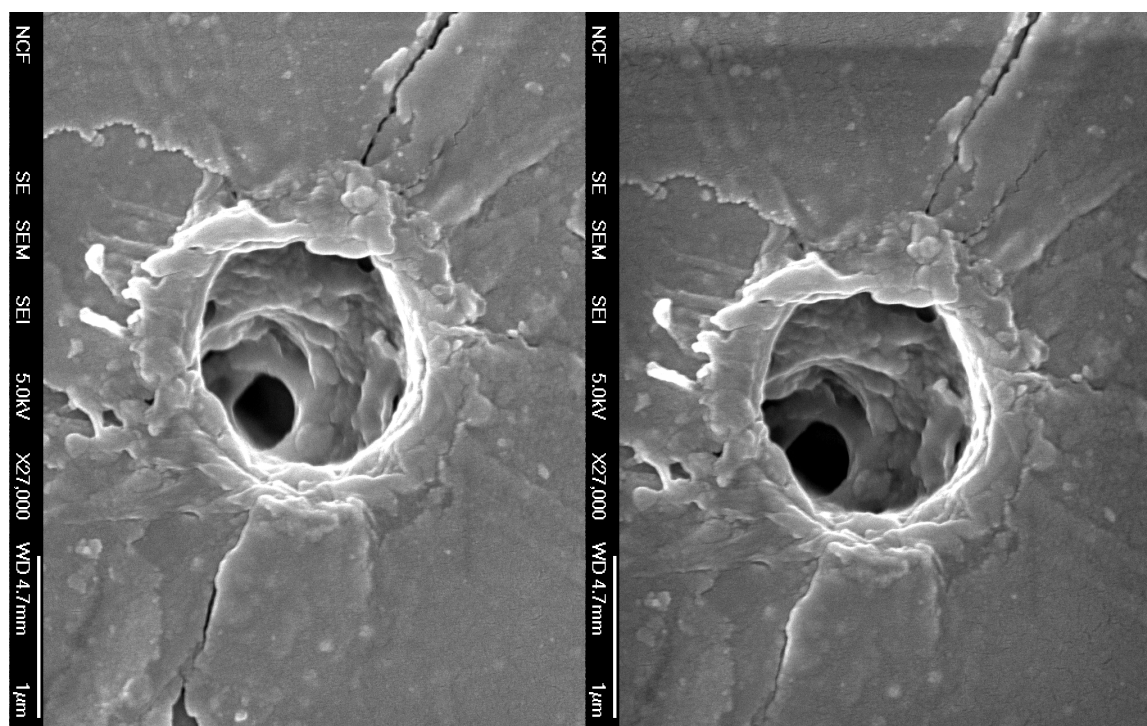


Figure 3.4: Two images of the same crater. The right image is taken at a 5 degree tilt compared to the left image.

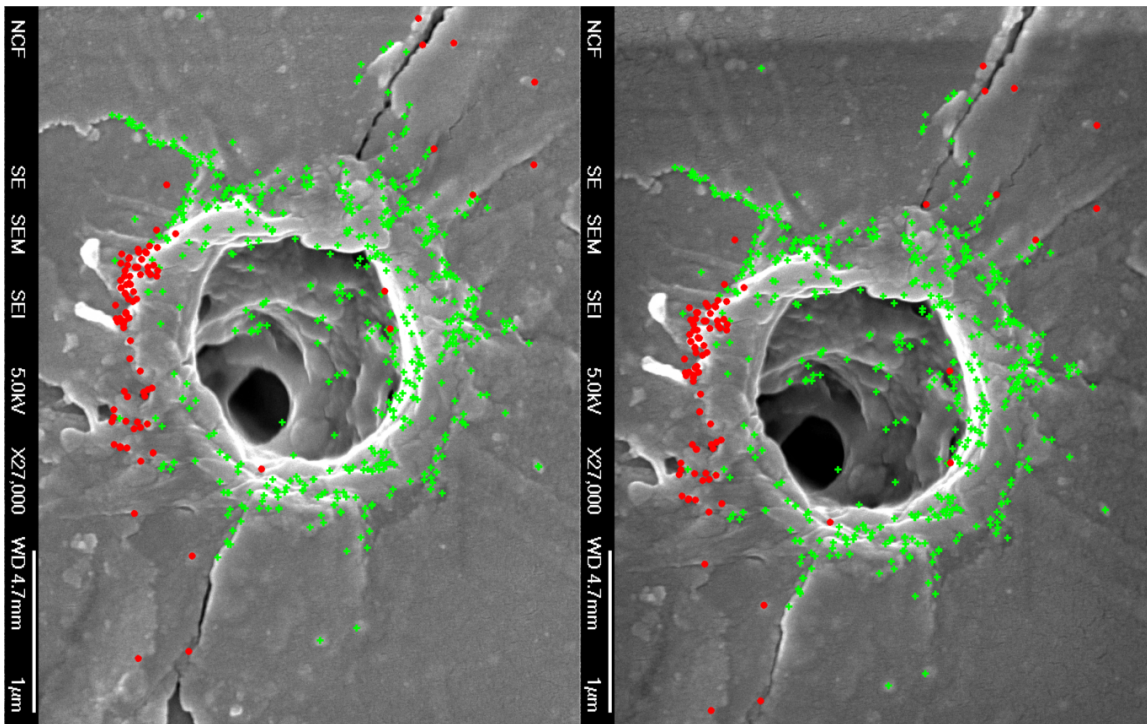


Figure 3.5: Two images of the same crater where matching points found by the SWIFT and SURF algorithms are shown. Green crosses are good matches, red circles were matches that failed a fidelity criteria.

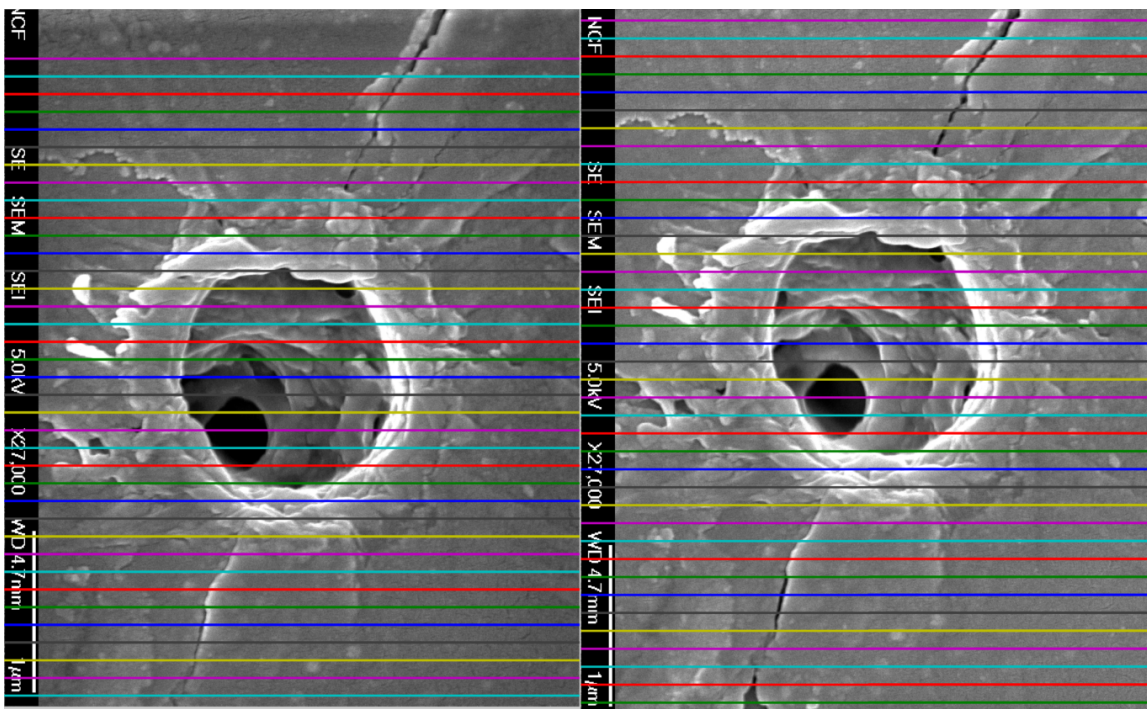


Figure 3.6: Two images of the same crater with epipolar lines drawn. Lines are color coded to show the same line across the two images.

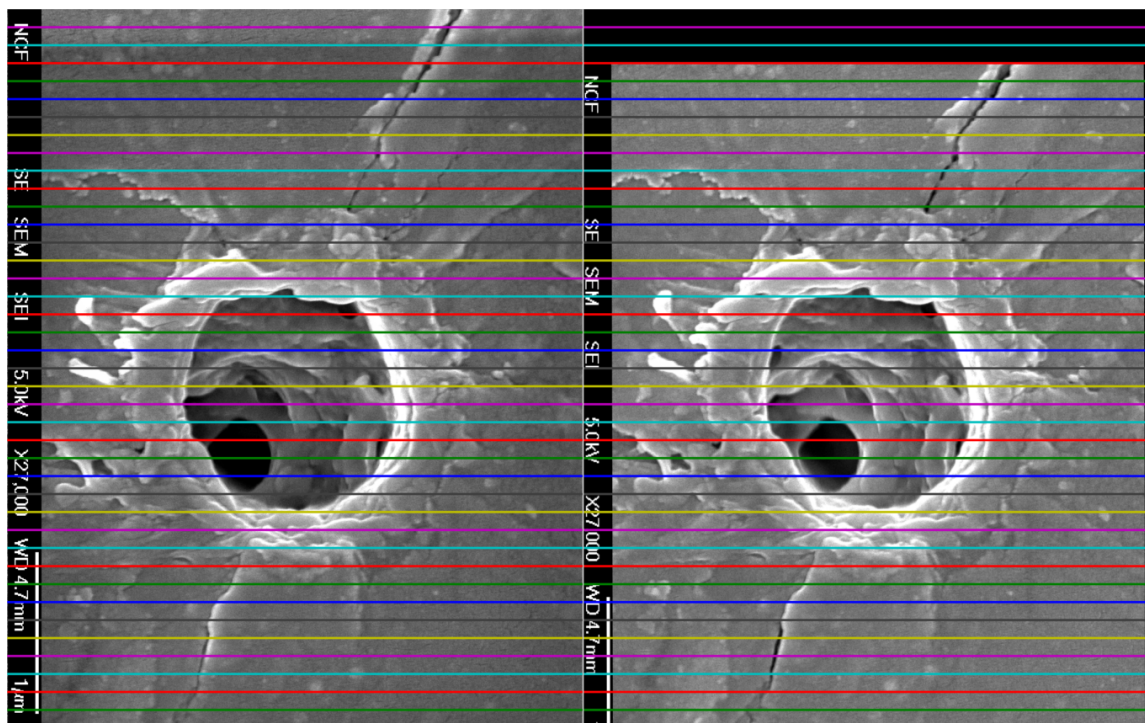


Figure 3.7: Two images of the same crater with epipolar lines aligned. These epipolar lines were recalculated so are not identical to those in figure 3.6.

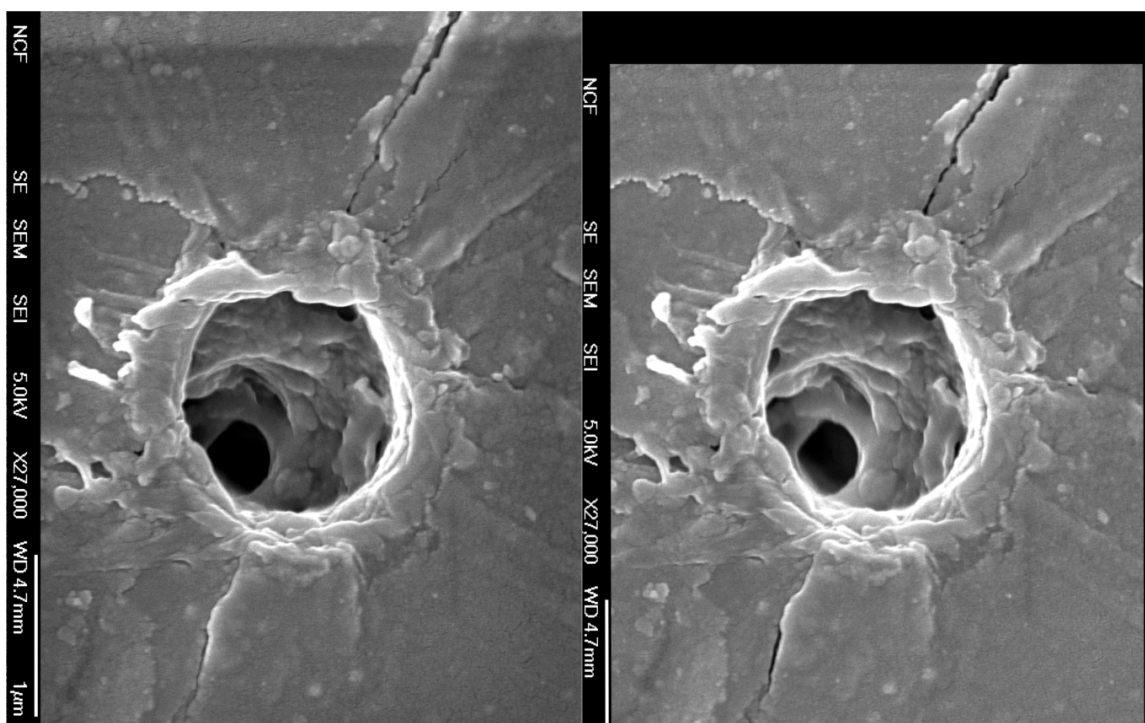


Figure 3.8: Two images of the same crater that have now been registered.

Looking at this image it becomes clear that within the crater there is a bit of disparity between the two images. On the other hand, on the surface of the image, there is very little. The tilting of the sample and the fact that the sample has a 3D shape causes this difference in disparity. Therefore, a disparity map can be computed. This disparity map is used to calculate the depth by equations developed by Lane (1969) and Piazzesi (1973). The result of this process is shown in Figure 3.10. Here the reconstruction is plotted in 3D with the image overlayed on the model. A color map is also plotted underneath the model to give a better idea of the elevation features in the crater.

While the 3D reconstruction method is quicker, it requires that images be taken where features can be resolved in the entirety of the crater. Certain crater geometries make this very difficult and this results in a noisy reconstruction. In order to assess the reliability of the reconstruction technique, several crater profiles were measured by both stereophotogrammetry and FIB cross-sectioning. Shown in Figure 3.11a-c is a crater where the interior is clearly visible, which yields a result that matches closely with the profile measured using the cross section taken with the FIB. On the other hand, on a crater where the interior yields almost no features (Figure 3.11d-f), the 3D reconstruction performs poorly (as expected). The 3D reconstruction method can also suffer from noise due to incorrect matching of points. This results in “noisy” surfaces which can make calculating the actual shape and depth of the crater difficult.

3.2.5 Elemental analysis using EDS

Many of the samples show features which appear to be impact craters but may not be. In order to distinguish these features from craters, elemental analysis of the feature using EDS can help. The chemical formula of PVDF is $-(C_2H_2F_2)_n-$. By using EDS on undamaged areas of the PVDF, one can detect C, F, and sometimes Al (from the metal coating), but Fe from the impactors is only detected near an impact crater, since PVDF contains no iron. EDS works by using the electron beam to eject electrons from the inner shell of an atom. When an electron from a higher shell falls into the resultant electron hole, an x-ray is emitted and the energy of the x-ray is equal to the energy difference between the two orbitals. The electron orbitals can be measured

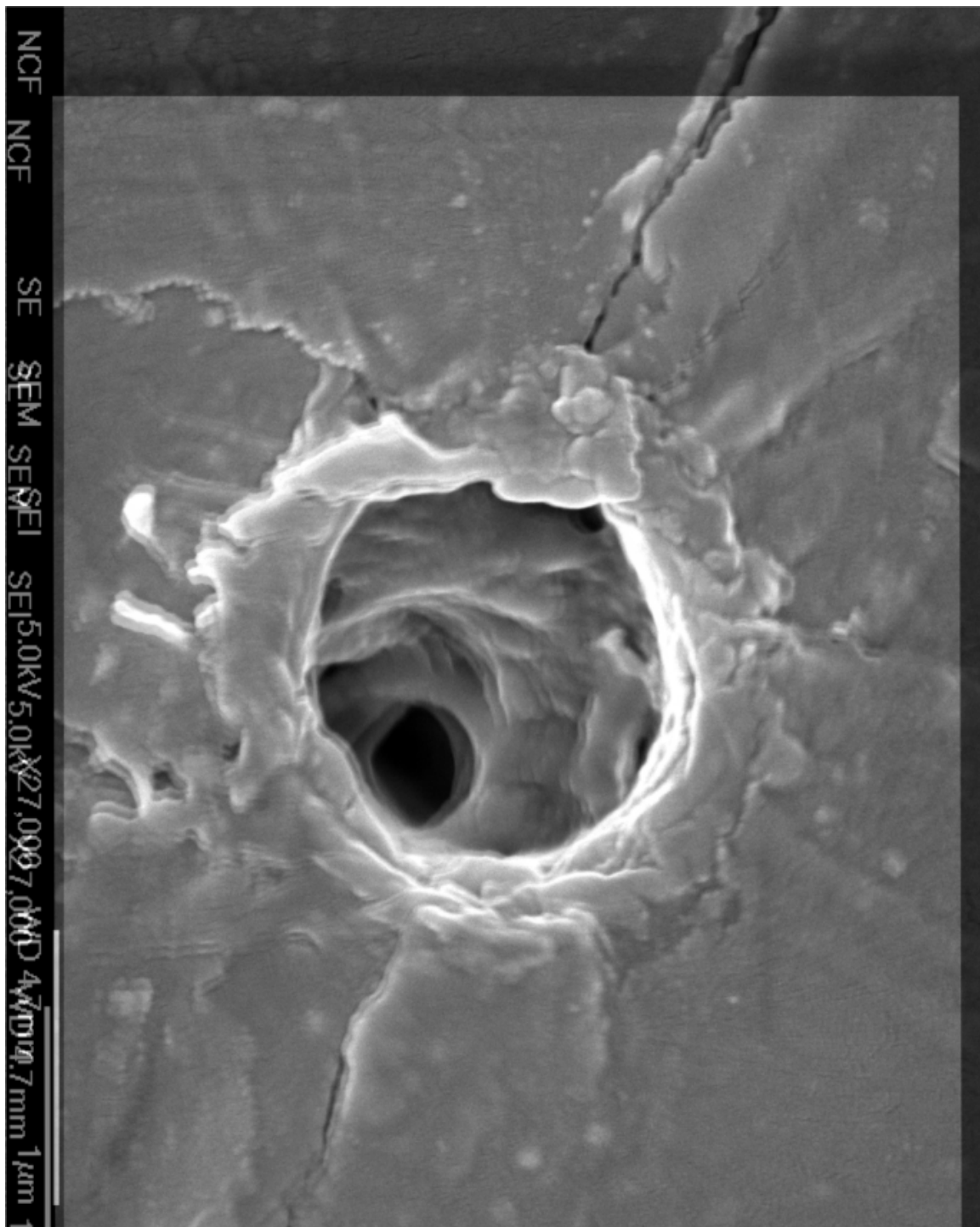


Figure 3.9: The two images from figure 3.8 are overlaid and the opacity of the top layer was reduced to 50%. Inside the crater, the disparity is the most obvious. On the surface, it is not clear there is any disparity.

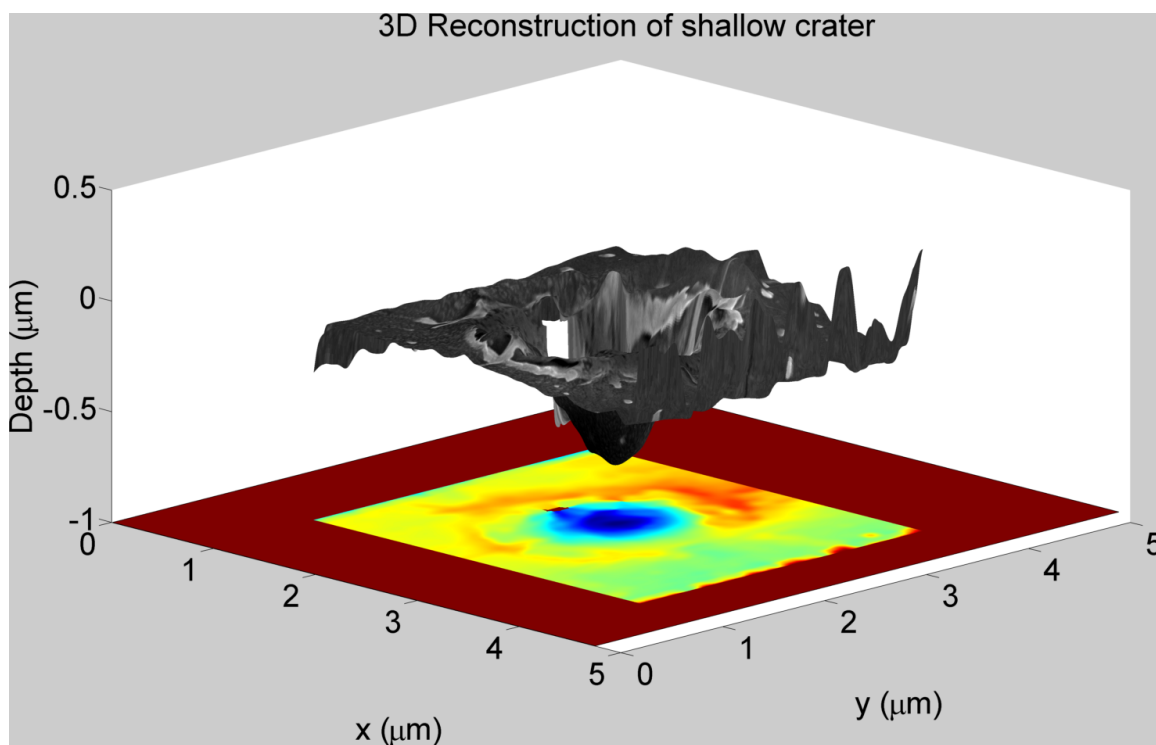


Figure 3.10: Sample 3D reconstruction from two images. In the color map, cool colors represent lower depths.

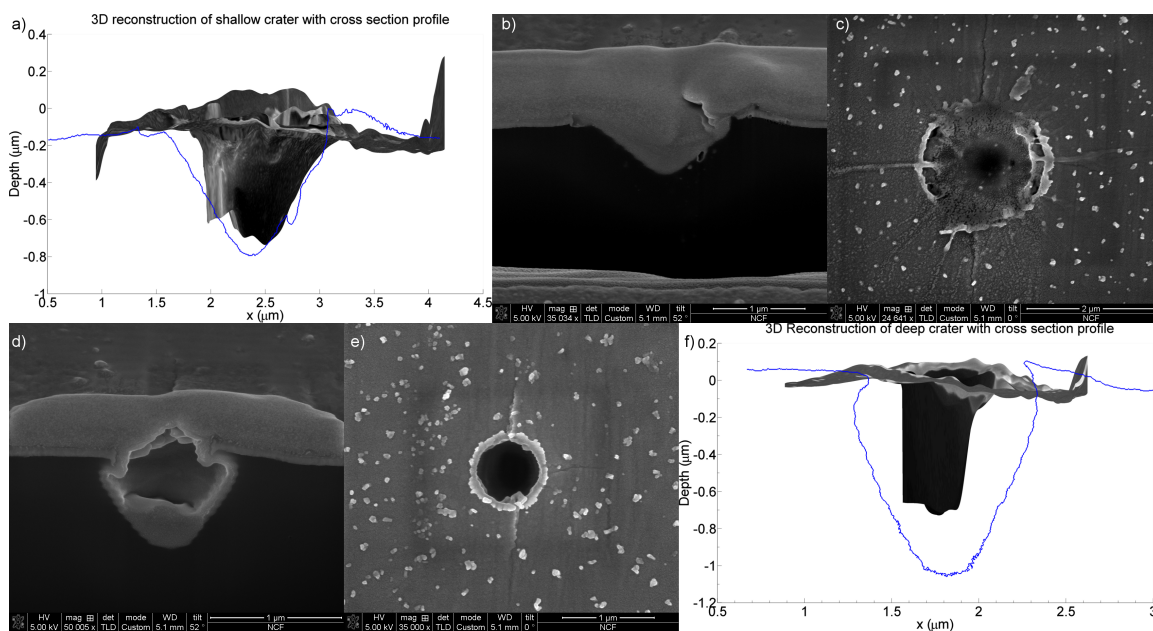


Figure 3.11: a) 3D reconstruction of a crater shown in b and c with the depth profile measured from the cross section overlaid. Notice the two depth profiles are well matched. b) Cross section of the crater viewed at a 52° angle. c) Undamaged view of the crater, crater interior is visible. d) Cross section of a different crater. e) Same crater as d, interior is not visible. f) 3D reconstruction with depth profile overlaid. Notice in this case the profiles do not match.

and the elements identified. Because heavy elements contribute to the background continuum x-ray intensity, the presence of gold increases the difficulty of accurately measuring trace elements. Fortunately, the gold layer applied to the PVDF sample is thin enough that EDS measurements are still possible (Figure 3.12). When using EDS, accelerating voltage and beam current must be increased to ensure enough energy to eject electrons from the inner orbitals. This increase in accelerating voltage and beam current results in a loss of imaging resolution due to an increased spot size and the increased interaction volume of the beam with the sample surface. Because of this, EDS measurements require extra time and are only used when there is some uncertainty whether a feature is a crater formed by impact, or if the feature was formed by another process.

3.3 Scaling-Law Results

Each of the 24 samples of PVDF were brought to the FESEM for analysis. One day was spent on each individual sample to find and image as many craters as possible. This was done due to the fact that each sample was approximately a 2 cm square and the target area of the beam was a 1 cm diameter circle within that square. Searching for $<1 \mu\text{m}$ craters in this area is difficult given the required resolution in order to distinguish craters from other blemishes on the surface such as cracks and dirt. On each sample anywhere between 5 and 30 craters were found resulting from the approximately 400 impactors. Using the techniques described in section 3.2.4, the diameter and depths of each imaged crater was measured. The results are shown in Figure 3.13. The measured depth and diameter was taken as the average measured depth and diameter for each sample. The error bars are the standard deviation of the depth and diameter added in quadrature with the errors from figure 3.1. The data has been fitted using a least squares method and compared to scaling laws used in Poppe et al. (2010), after correcting a typographical error of a factor of 10 in their Eqs. 2 and 6, based on Lambert (1997) and McDonnell and Sullivan (1991). The scaling law

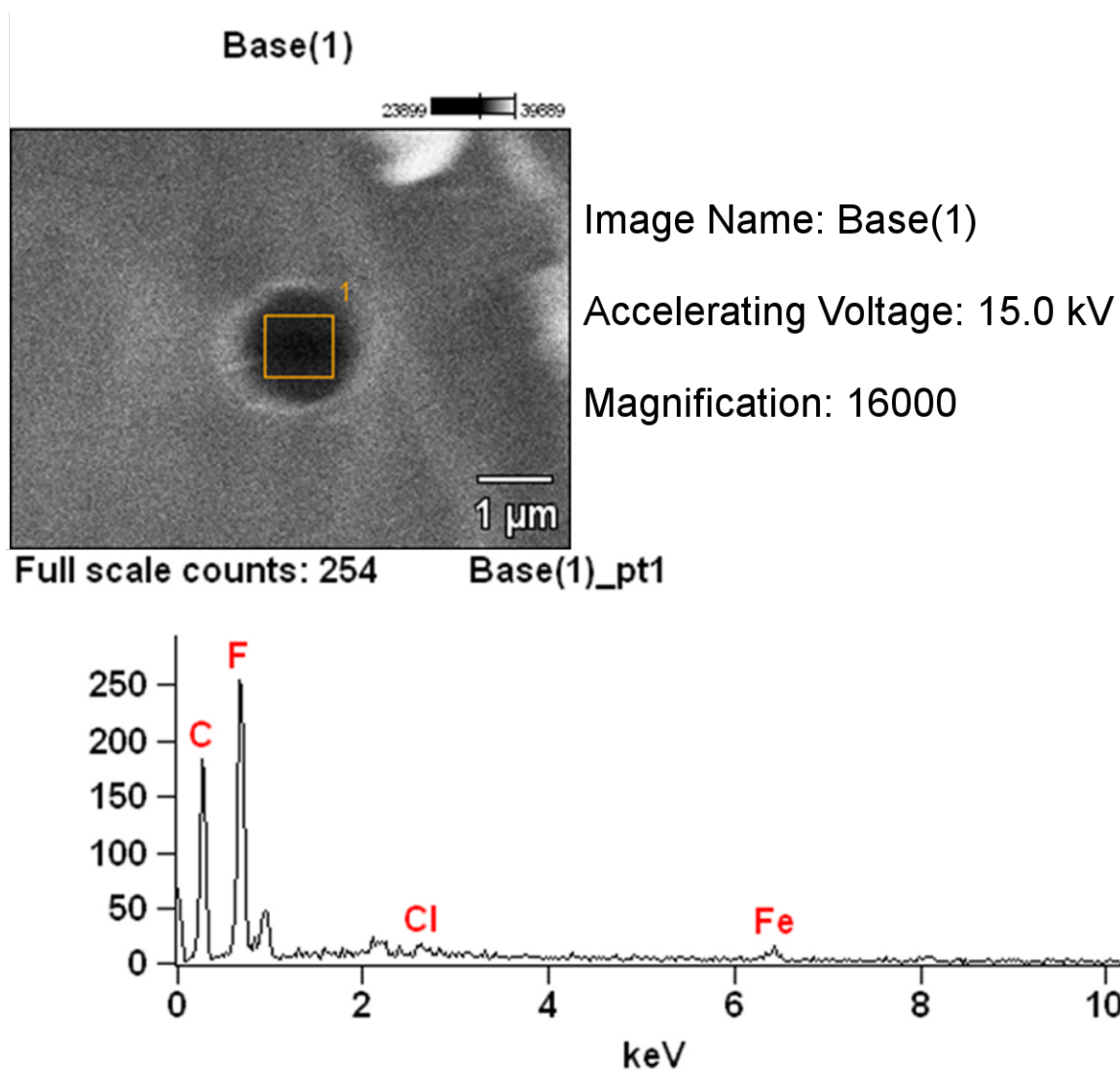


Figure 3.12: Sample EDS measurement of a crater. The image is blurry due to the higher accelerating voltage required to make EDS measurements. Image resolution is not important since x-ray energy constitutes the measurement.

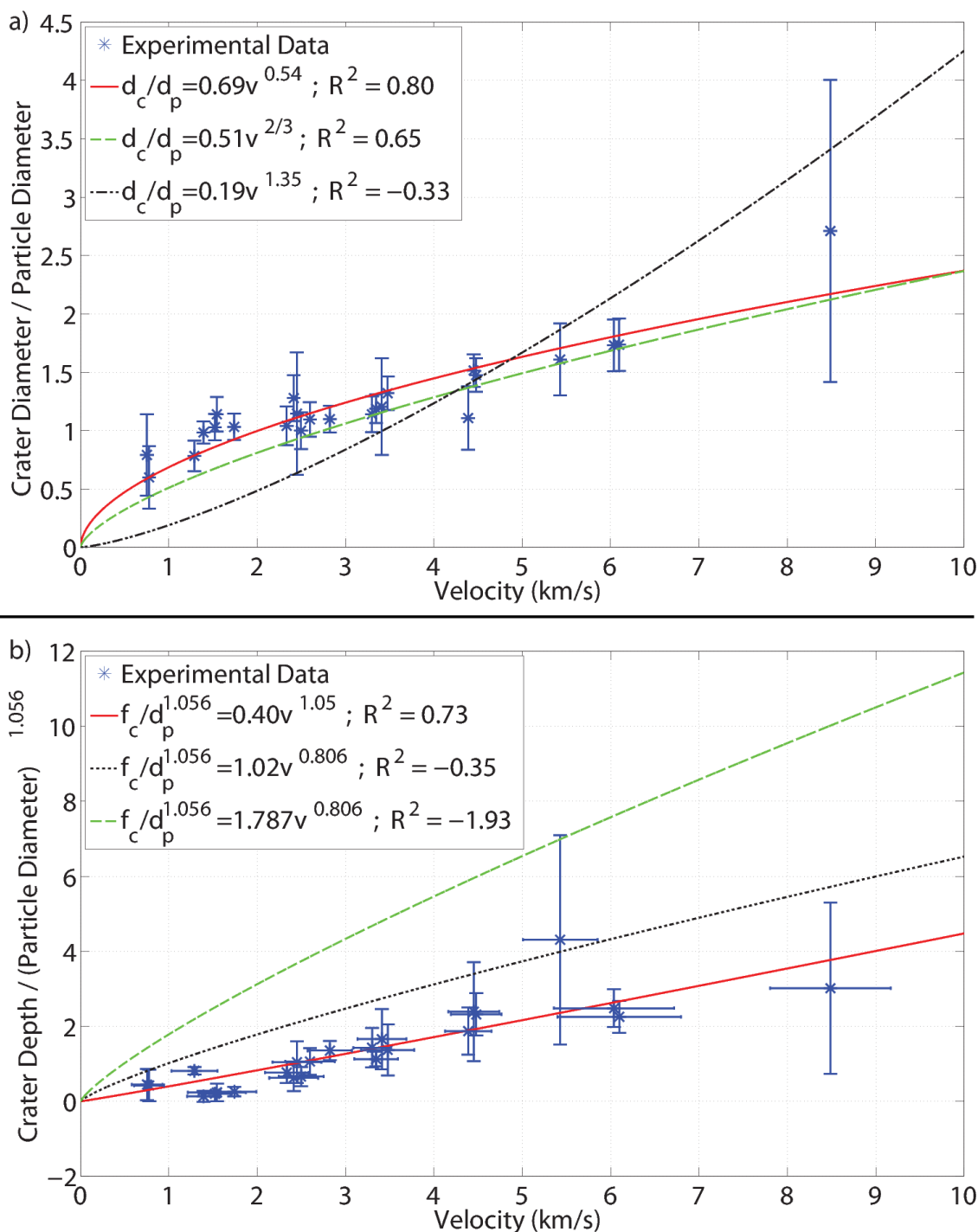


Figure 3.13: a) Crater diameter divided by particle diameter versus velocity. The red line is a least squares fit to $\frac{d_c}{d_p} = av^b$, the green line is the scaling law Eq. 2 from Poppe et al. (2010) multiplied by 10, and the black line is the scaling law Eq. 6 from Poppe et al. (2010) multiplied by 10. b) Crater depth divided by particle diameter versus velocity. The red line is a least squares fit to $\frac{f_c}{d_p} = cv^d$, and the green line is the scaling law Eq. 1 from Poppe et al. (2010); McDonnell and Sullivan (1991) using iron as the projectile. The black line is also Eq. 1 from Poppe et al. (2010) with olivine as the projectile material, which was mistakenly used in the simulation (Poppe, 2013).

for crater diameter was determined by a least squares fit to a power-law and given by

$$d_c/d_p = av^b \quad (3.3)$$

Coefficients (with 95% confidence bounds):

$$a = 0.69 (0.57, 0.80)$$

$$b = 0.54 (0.42, 0.65)$$

where d_c is the diameter of the crater, d_p is the diameter of the impactor, and v is the velocity of the impactor. Eq. 3.3 has a goodness-of-fit of $R^2 = 0.80$. In order to address Eq. 7 from Poppe et al. (2010),

$$d_c = 7.8v^{1.96}d_p^{2.14}, \quad (3.4)$$

another fit was performed for the crater diameter given by

$$d_c = av^b d_p^c \quad (3.5)$$

Coefficients (with 95% confidence bounds):

$$a = 0.84 (0.71, 0.98)$$

$$b = 0.33 (0.19, 0.47)$$

$$c = 0.95 (0.80, 1.10)$$

with $R^2 = 0.94$. On the other hand, Eq. 3.4 has an $R^2 = -1700$. This clearly shows that this form does not fit the data at all.

The crater depth was fitted to a power-law given by

$$f_c/d_p^{1.056} = cv^d, \quad (3.6)$$

Coefficients (with 95% confidence bounds):

$$c = 0.40 (0.192, 0.6096)$$

$$d = 1.05 (0.73, 1.36)$$

where f_c is the depth of the crater. Eq. 3.6 has a goodness-of-fit of $R^2 = 0.73$. Eq. 2 from Poppe et al. (2010) uses ratios of projectile and target densities to iron and aluminum respectively, in

order to generalize the results found in McDonnell and Sullivan (1991). In the Poppe et al. (2010) simulations, the projectile material was mistakenly chosen as olivine despite iron being the projectile material in the actual experiments (Poppe, 2013). Interestingly, by using the correct material in eq. 2 from Poppe et al. (2010), the scaling law is an even poorer fit to the experimental data. There are several possible reasons for this. The 3D reconstruction is still in development and may be underestimating crater depth, especially at the high velocity end. This is due to a limitation of the electrostatic accelerating method that causes faster particles to be smaller. Small craters are more difficult to image in such a way that the bottom of the crater is visible. Another possible source, is that eq. 1 from Poppe et al. (2010) was derived from iron impacts onto aluminum (McDonnell and Sullivan, 1991). As such, it is not inherent that iron impacting into PVDF should follow the same scaling law. Further work will address possible improvements to ensure correct measurement of the depth of the craters.

Previous crater scaling work has suggested that these scaling laws be proportional to $v^{2/3}$ (Charters and Locke, 1958; Watts and Atkinson, 1995). According to Charters and Locke (1958), this type of scaling suggests that the crater volume is proportional to the kinetic energy of the projectile. Watts and Atkinson (1995) argue that the velocity exponent should be between $2/3$, the energy solution, and $1/3$, the momentum solution depending on how dissipative the system is (more dissipative leads to an exponent near $2/3$) for the crater diameter scaling. In the case of penetration depth, the scaling depends on the Hugoniot term from the shock-speed versus particle speed relationship, s . Small s leads to a velocity exponent of $1/3$, whereas high s leads to an exponent approaching $2/3$. The scaling law found in eq. 3.3 appears to agree with both papers, with an exponent near $2/3$. However, the scaling law found in eq. 3.6 does not have a velocity exponent near $2/3$. Due to this, it is unclear how far these scaling laws can be extrapolated, as there is no clear physical explanation for the scaling of the crater depth.

In figure 3.14, the crater diameter is plotted against the particle diameter along with data from Kearsley et al. (2006); Price et al. (2010); Hörz (2012). The solid line is fit to the three data

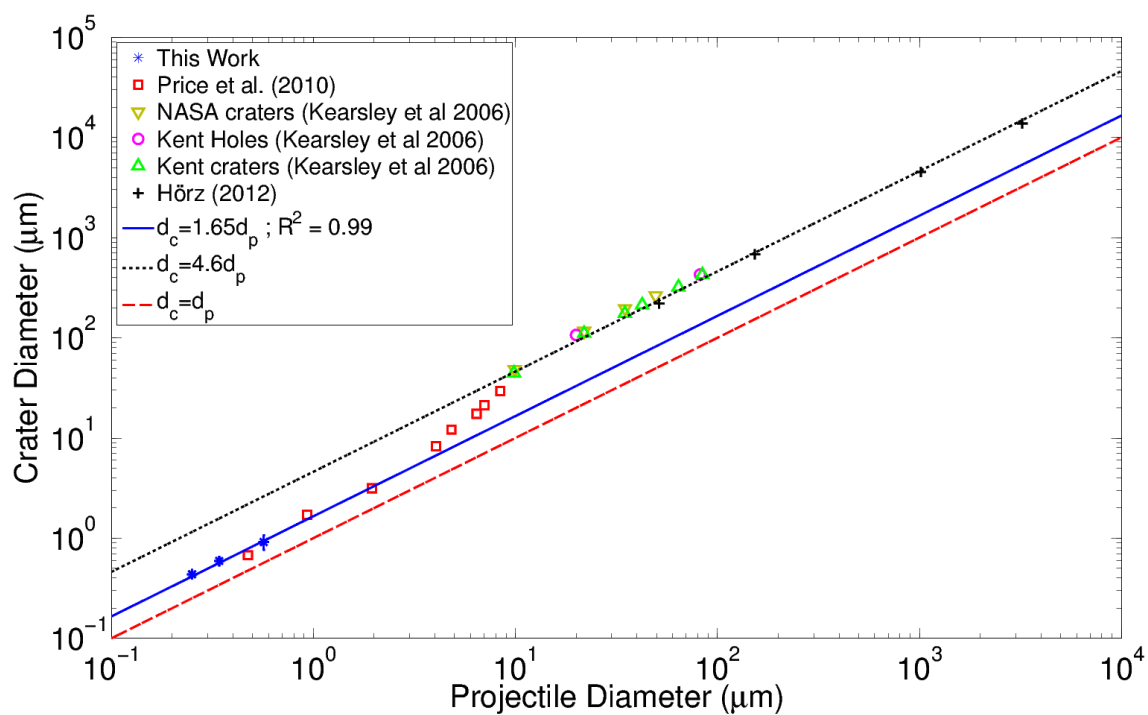


Figure 3.14: The velocity of all particles was ≈ 6 km/s. This work used iron particles hitting a PVDF target. The Price et al. (2010) data used silica projectiles hitting an aluminum foil. The Kearsley et al. (2006) data used soda-lime glass projectiles on aluminum foil, and include punctures as well as craters. The Hörz (2012) data used aluminum particles hitting an aluminum foil.

points from this work and is given by

$$d_c(\mu m) = g d_p(\mu m) \quad (3.7)$$

Coefficients (with 95% confidence bounds):

$$g = 1.65 \text{ (1.474, 1.833)}$$

with a goodness-of-fit of $R^2 = 0.99$. This data agrees with the finding in Price et al. (2010) that the crater scaling is different at particle size smaller than $3 \mu m$. This is interesting since the materials used in this work are very different than materials used in the previous works.

3.4 Conclusions and Future Work

This study presents a 3D stereophotogrammetry approach to measuring crater depths using two SEM stereopair images. This method is still under development as some of the 3D reconstructions can be quite noisy. With the use of advanced smoothing algorithms, it may be possible to measure the full volume of the crater accurately. Further work will be done to ensure the correct measurement of crater depths by continued cross-evaluation of the 3D stereophotogrammetry and the cross-sectioning techniques. This will be important in determining when the 3D technique will be sufficient for determining crater properties and when a cross section will be required. Future investigations will give more confidence in measured crater depths. The numerical simulations (Poppe et al., 2010) will be rerun using the scaling laws determined by this study to test for improvement in its accuracy to predict the impact generated charge in a PVDF detector. PVDF samples will also be taken to a light gas gun in order to extend the available mass and speed range of the impacting dust particles.

Scaling laws used in Poppe et al. (2010) were adapted from works using iron impactors and an aluminum target (McDonnell and Sullivan, 1991) and aluminum projectiles on flexible external insulation targets (layered material consisting of Nextel fabric, silica felt, and fabric of Porcher 116 glass) (Lambert, 1997). While the Lambert (1997) scaling law appears to agree with the measured scaling law, the McDonnell and Sullivan (1991) scaling law appears to be off by a factor of 3. It

is not clear that either scaling law used should necessarily agree with the measured scaling laws, however, it is important to use the correct scaling laws in drawing conclusions from the theory for PVDF detectors presented in Poppe et al. (2010). Measurements of particle size scaling laws agree with previous work done by Hörz (2012); Price et al. (2010); Kearsley et al. (2006).

In the next chapter I begin to explore the physics behind the cratering process and discuss the detailed shape of the measured crater surfaces.

Chapter 4

Cratering Theory

4.1 Introduction

There are many approaches to understanding the cratering process. In chapter 3, the form of the scaling law was selected to compare results to simulations done in Poppe et al. (2010). In this chapter, I will look at what physics actually goes into the cratering process and what form the crater scaling laws should actually take. Unfortunately the literature is very scattered on this topic. Most of the work done so far is empirical with some discussion of the physics behind the empirically determined form.

4.2 Theory

The governing parameters for scaling laws are

$$d_i, v, \{\tau_i\}, \{\tau_t\} \quad (4.1)$$

where d_i is the spherical diameter of the impactor, v is the velocity of the impactor, $\{\tau\}$ denotes material parameters, and subscripts i and t refer to impactor and target (Yu et al., 1994).

In the literature, crater scaling laws generally take the form of

$$\frac{f}{d_p} = K \left(\frac{\rho_p}{\rho_t} \right)^g v^a \quad (4.2)$$

where f is the property to be measured (diameter or depth), K is some empirically determined constant, ρ_p is the density of the impactor, ρ_t is the density of the target, and g and a are empirically determined power laws (Charters and Locke, 1958; Gault, 1973; Latunde-Dada et al., 2011).

Typically $1/3 \leq a \leq 2/3$ where it is said that when $a = 1/3$ momentum dominates the process and when $a = 2/3$ kinetic energy dominates the process. This comes about because it is generally believed that the crater is hemispherical. If I take the cube of equation 4.2, set a to $1/3$, and assume the crater is hemispherical, I get

$$f^3 = K \left(\frac{\rho_p}{\rho_t} \right)^{3g} v d_p^3 \quad (4.3)$$

$$f^3 = K \left(\frac{\rho_p}{\rho_t} \right)^{3g} v C m \quad (4.4)$$

$$AV = CK \left(\frac{\rho_p}{\rho_t} \right)^{3g} (mv) \quad (4.5)$$

$$AV = CK \left(\frac{\rho_p}{\rho_t} \right)^{3g} (p) \quad (4.6)$$

where p is the momentum, V is the volume of the crater and $C = (3/(4\pi\rho_p))$, and $A = 4/3\pi\rho_t b$ where b is an arbitrary factor. If I instead set $a = 2/3$ the resulting equation is

$$AV = CK \left(\frac{\rho_p}{\rho_t} \right)^g (mv^2) \quad (4.7)$$

$$AV = CK \left(\frac{\rho_p}{\rho_t} \right)^g (E) \quad (4.8)$$

where E is the kinetic energy. As such I see that V depends on the momentum, p , when the velocity exponent is equal to $1/3$ and depends on kinetic energy, E , when the velocity exponent equals $2/3$. The other term in the equation, $\left(\frac{\rho_p}{\rho_t} \right)^g$ is there to define differences between target material and impactor material. This form uses the density to distinguish these characteristics, however, this can be replaced with acoustic impedance (Engel, 1963), dynamic yield strength (Yu et al., 1994), longitudinal sound speed (Sawle, 1970), or some combination of these parameters. It is unclear what the dependence on material properties should be, and unfortunately will not be addressable in this work as only one target material and one impactor material was used.

4.3 Surface Fitting

The depths and diameters of the craters were measured by using an SEM and a 3D photogrammetry technique. This resulted in a 3D measurement of the surface and provided surface data that could be fitted to a known shape. It is not clear what shape would best simulate the

crater surface. In figure 4.1, the shape comparisons used can be seen. Initially a Gaussian, with the equation

$$z = ae^{-\frac{(x-x_0)^2+(y-y_0)^2}{w^2}} + b \quad (4.9)$$

was used. In order to fit to each surface, five parameters must be fitted, a , w , x_0 , y_0 , and b . These parameters correspond to the depth, width, x-coordinate of the center of the crater, y-coordinate of the center of the crater, and offset height of the crater respectively. The parameters of interest being fit are a and w while the other three parameters were necessary due to the fact that during imaging, each crater was not centered over the exact same position, and there were slight differences in the total offset of the surface calculated through the 3D photogrammetry technique. Looking at figure 4.1b and c, it is clear that the gaussian is too wide at the top of the crater, and too narrow at the bottom. In order to compensate for this, the super gaussian in figure 4.1d was used. The super gaussian equation is given by

$$z = ae^{-\left(\frac{\sqrt{(x-x_0)^2+(y-y_0)^2}}{w}\right)^n} + b. \quad (4.10)$$

Here the fit parameters are the same as the gaussian with the additional parameter n to be fitted. This n parameter corresponds to the amount of ‘‘curvature’’ in the surface. Larger n gives a more cylindrical shape whereas lower n gives a more gaussian shape. In this fit, the relevant fitting parameters were a , w , and n .

In order to perform these multi-parameter fits, a MATLAB code was written to walk around in parameter space and calculate what incremental change would minimize an error function. This method requires a choice of error function, step size, and an initial guess. The initial parameters were set as seen in table 4.1. This initial guess did a fairly good job of approximating the crater shape allowed for quicker convergence. The error function to be minimized was chosen as

$$err(a, w, n, x_0, y_0, b) = \sum_i^{pixels} \left| ae^{-\left(\frac{\sqrt{(x_i-x_0)^2+(y_i-y_0)^2}}{w}\right)^n} + b - z_{im} \right| (z_{im} - \max(z_m))^2 \quad (4.11)$$

where the subscript i denotes the value at pixel i , and $(z_{im} - \max(z_m))^2$ is a weighting factor used to increase the fidelity of the fit at the deepest part of the measured crater surface. During each

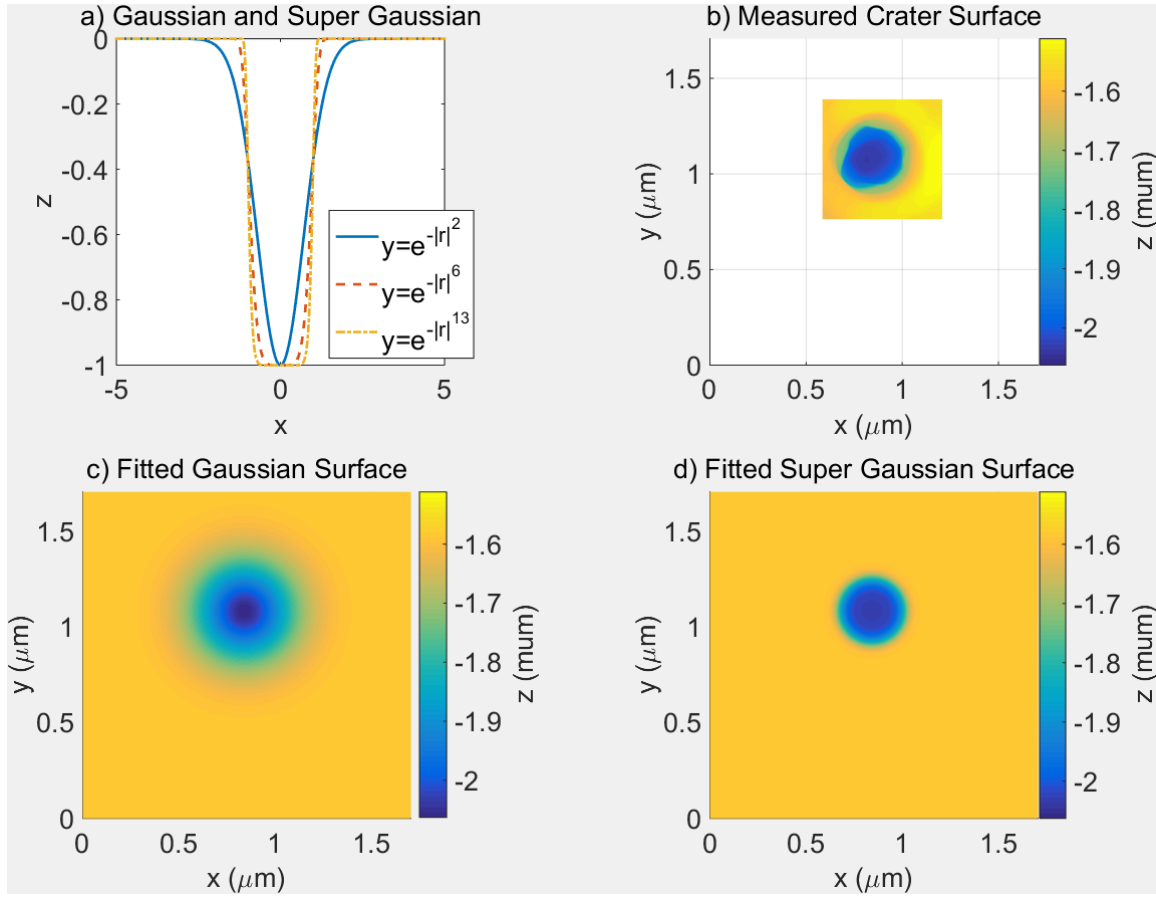


Figure 4.1: a) Comparison of Gaussian and super Gaussian functions. A super Gaussian is a Gaussian where the absolute value of the displacement r is raised to a higher order than 2. b) Measured surface of an impact crater where the impactor had a velocity of 6.10 km/s and a radius of 126 nm. c) 2D Gaussian fit to the surface in a $(z = ae^{-\frac{x^2+y^2}{w^2}})$, a and w were fit parameters. d) 2D super Gaussian fit to the surface in a $(z = ae^{-\left(\frac{\sqrt{x^2+y^2}}{w}\right)^n})$, a , w , and n were fit parameters. The color scale is the same for b,c, and d.

a	$\min(z_m) - \max(z_m)$
w	radius/2
n	4
x_0, y_0	indices of $\min(z_m)$
b	$\max(z_m)$

Table 4.1: Initial guess for parameters of surface to be fit. z_m is the measured surface of the crater and radius is the measured radius of the crater from chapter 3

iteration of this method, the error function is calculated and then recalculated with each parameter incremented by one stepsize and decremented by one stepsize (i.e. $err(a + astep), err(a - astep), err(n + nstep), \dots$ etc). Whichever calculation provides the minimized error function determines the new parameter value. For example, if the value of $err(a - astep)$ is the smallest in a given iteration, then the a parameter is reassigned as $a - astep$ and the process repeats. If the value of the error function with the current parameters is the smallest, then the stepsize in each parameter is reduced and the process repeats. This process is repeated until either the step size is small (less than a pixel) or the number of iterations is over 100000. First the initial guess is refined only in the x_0 , y_0 , and b parameters. This was done because the data will sometimes have spurious minimums and maximums. Because of this, the fitting can take longer or not converge due to the fact that it is fitting the initial guess to a local minima. To counteract this issue, the initial stepsize was chosen to be large and the stepsize is only reduced by one half. Then the code reruns the optimization loop where all fitting parameters were free. This generally reduced the number of iterations required to fit the surface.

In order to determine how well the fitting program worked, a goodness of fit was calculated. The goodness of fit was defined as

$$GoF = \frac{err(a_f, w_f, n_f, x_{0f}, y_{0f}, b_f)}{|a_f|N} \quad (4.12)$$

where the subscript f denotes the final fitted parameter, and N is the total number of pixels being fitted. Based on this definition of the goodness of fit, the smaller the goodness of fit, the better the fit is. The error function itself is a measure of how good the fit is, however, cannot be compared across surfaces. This is because the number of pixels being fit on each surface is different, as each surface had different good pixels in the picture that could be fit. Furthermore, the goodness of fit must be normalized to the depth of the crater. For example, if you imagine a crater surface and a given fit to the surface, and imagine at one point the difference is given by x . Imagine now that both the crater and the fit are twice as deep but otherwise unchanged. This difference at that one point is now $2x$. By applying this logic to every point in the surface, it becomes clear that the error

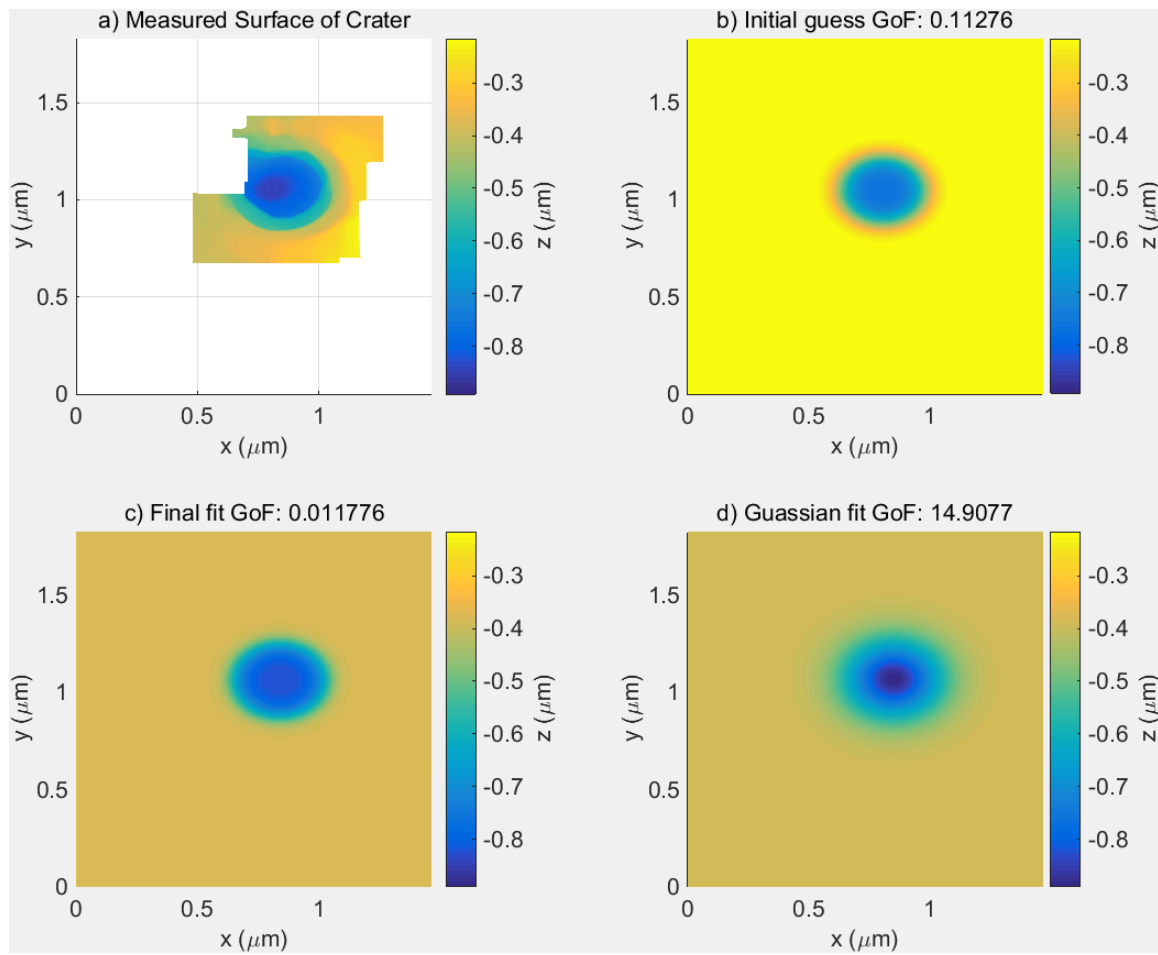


Figure 4.2: a) The measured surface of the crater. b) The initial guess used to start the fitting code. c) The final fitted surface after running the fitting code. d) An example of a bad fit. This surface was obtained by fitting the surface to a Gaussian.

functions is twice as large. The fit, however, has not gotten twice as bad despite this doubling of the error function. Therefore it is clear that the depth of the crater must be taken into account. Figure 4.2 shows a comparison between a single measured crater surface and several fitted surfaces that can give a better idea of how to compare the goodness of fit parameter.

Figure 4.3 shows several craters and their associated best fit surface. Figure 4.3a and b show the best goodness of fit of all measured crater surfaces, while c and d show an average goodness of fit. As you can see, Figure 4.3 e and f is an example of when the fitting method fits to a local minima instead of the entire surface. This did not appear to happen very often and this particular case likely occurred due to the larger sections of missing surface data.

There were a total of 252 surfaces that were good enough to be fit to. The number of surfaces available on each sample varied, some having upwards of 20 and some having only 1. The goodness of fits on all of them ranged from 0.0022 to 0.158. The mean goodness of fit was 0.0193 and the standard deviation was 0.018. This means that almost 95% of the fits had a goodness below 0.055. Figure 4.2b shows a typical goodness of fit for an initial guess. As you can see, there is a factor of ten improvement of goodness of fit after performing the fitting which is pretty typical for most surfaces.

4.4 Results

For each measured surface, a fit similar to the one in figure 4.4 was obtained. By fitting all available surfaces for each PVDF sample, a library of fitted parameters was created. For each sample, the mean of each parameter was used to determine the best fit for that particular impactor velocity and size. These parameters were then plotted and fit to a function with the equation

$$p/d = \alpha v^\beta \quad (4.13)$$

where p is the parameter to be fit (a , w , or n), d is the impactor diameter, v is the impactor velocity, and α and β are parameters to be fit. By doing this, an equation for each parameter is created that can be used to estimate the crater shape for any give velocity and size of particle.

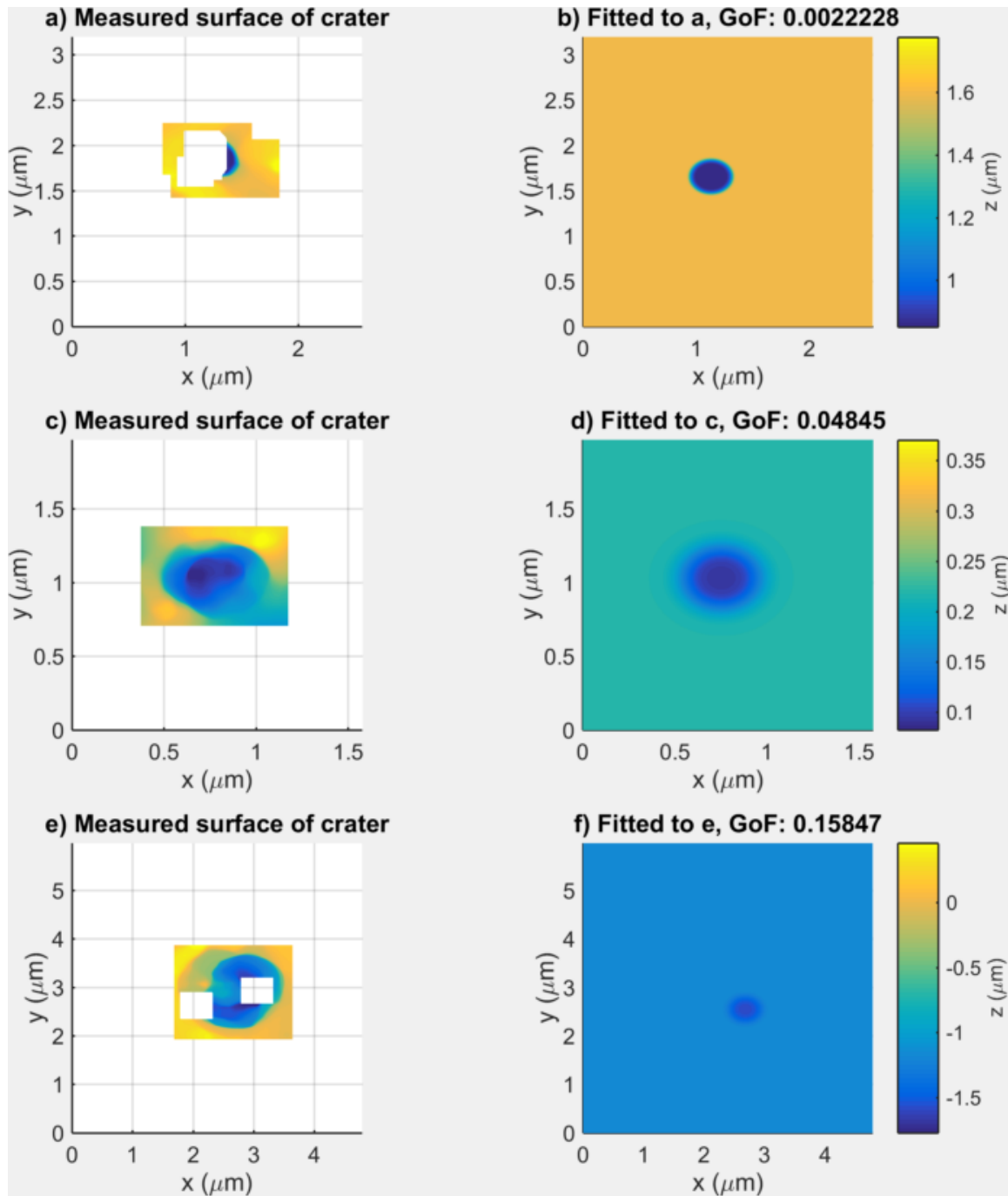


Figure 4.3: Comparison of goodness of fits of different crater surfaces. a,b) The measured surface and the best fit to the crater with the best goodness of all the measured surfaces. c,d) The measured surface and the best fit to the crater with a median goodness of fit. e,f) The measured surface and best fit to the crater with the worst goodness of fit. Here it appears the code fit to a local minima instead of the entire crater.

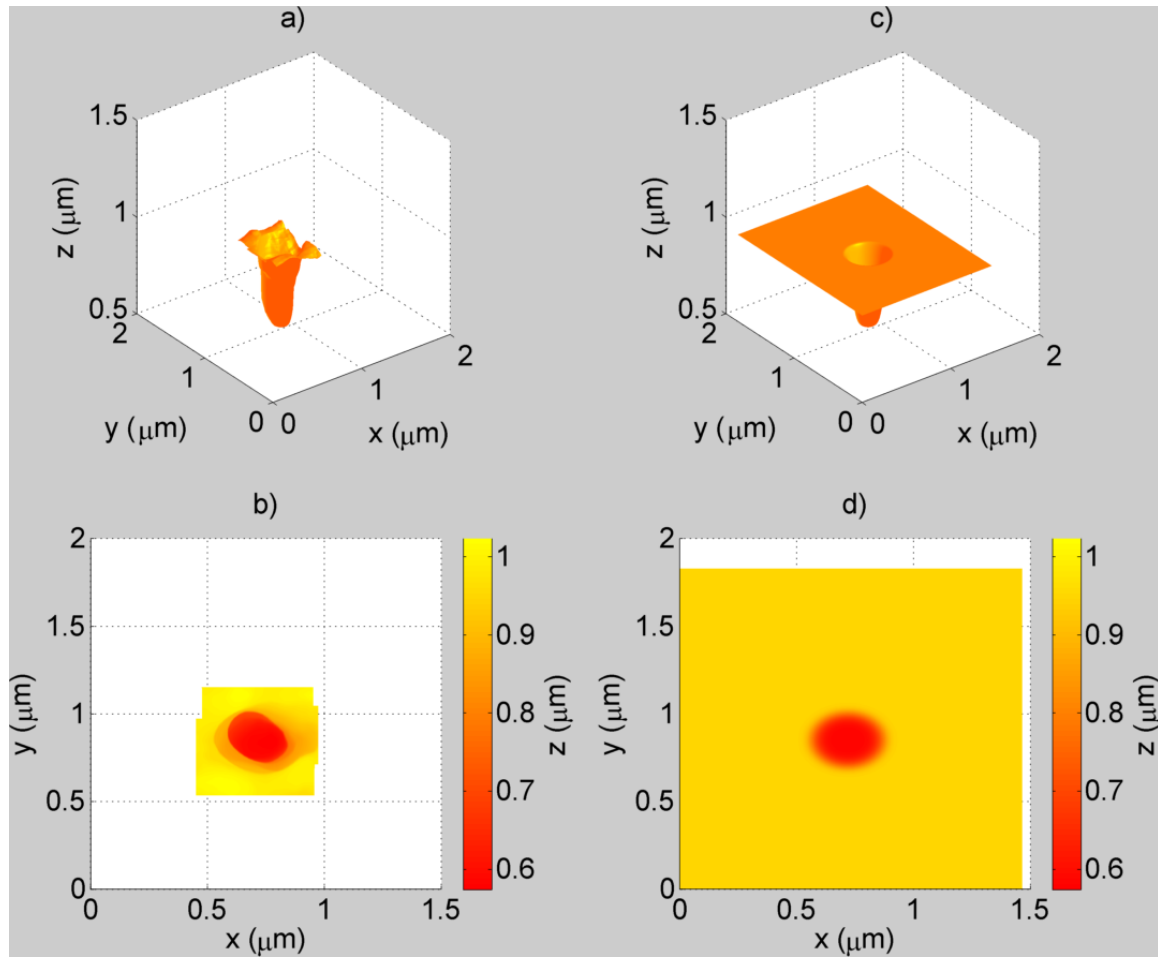


Figure 4.4: a) The surface measured from the PVDF sample shown in 3D with lighting. The impactor had a velocity of 6.10 km/s and a radius of 126 nm. b) The measured surface as a colormap. c) The fitted surface in the same lighting as a. d) The fitted surface as a colormap. Fitted parameters are $a = -0.364$, $w = 0.1567$, and $n = 5.5636$. As you can see the fit compares quite well with the measured surface.

Parameter	α	95% confidence bounds	β	95% confidence bounds	R^2
a	-0.3076	(-0.3929, -0.2223)	0.9731	(0.8029, 1.143)	0.8864
w	0.2032	(0.1529, 0.2534)	0.6877	(0.5246, 0.8507)	0.7729
n	1.26	(0.4663, 2.053)	1.485	(1.133, 1.838)	0.8138

Table 4.2: Fit parameters and 95% confidence bounds for those fits

Figure 4.5a shows the ratio of the a parameter to the particle diameter (in μm) versus the particle velocity (in km/s), figure 4.5b shows the ratio of the w parameter to the particle diameter versus velocity, and figure 4.5c shows the ratio of the n parameter to particle diameter versus the particle velocity. Some of the vertical error bars are missing in the figures. They were omitted because the number of surfaces that could be fit was less than 5. Because of this, a sensible error in the parameter could not be determined so the errorbar was omitted. The results are summarized in table 4.2. As expected, the a parameter has an exponent near 1. This parameter is essentially the measured depth of the particle. In chapter 3, the equation for depth was measured to be

$$f_c/d_p^{1.056} = 0.40v^{1.05}. \quad (4.14)$$

By replacing f_c with a , I see that these parameters either fall within or just outside the 95% confidence bounds. This result is to be expected, as these two parameters should ideally be identical.

The interpretation of the w parameter is harder as it approaches the radius as the n parameter goes to infinity but is less well defined as the n parameter approaches 0. At $n = 2$, a Gaussian, the w parameter is equal to $HWHM/\sqrt{\ln(2)} \approx 1.2 * HWHM$ where $HWHM$ is the half width half max. Since a Gaussian technically extends to infinity, it is hard to define where the exact radius is, however the $HWHM$ appears visually at least to be about the half the radius of the crater when a Gaussian is fitted to the crater surface. For the purposes of this paper however, the w parameter will be treated as similar to the radius as the n parameter is always greater than 2. With this in mind, looking at the equation for the diameter of the crater,

$$d_c/d_p = 0.69v^{0.54}, \quad (4.15)$$

is also close to that measured for w (remember that $w \approx d_c/2$). This increases our confidence in

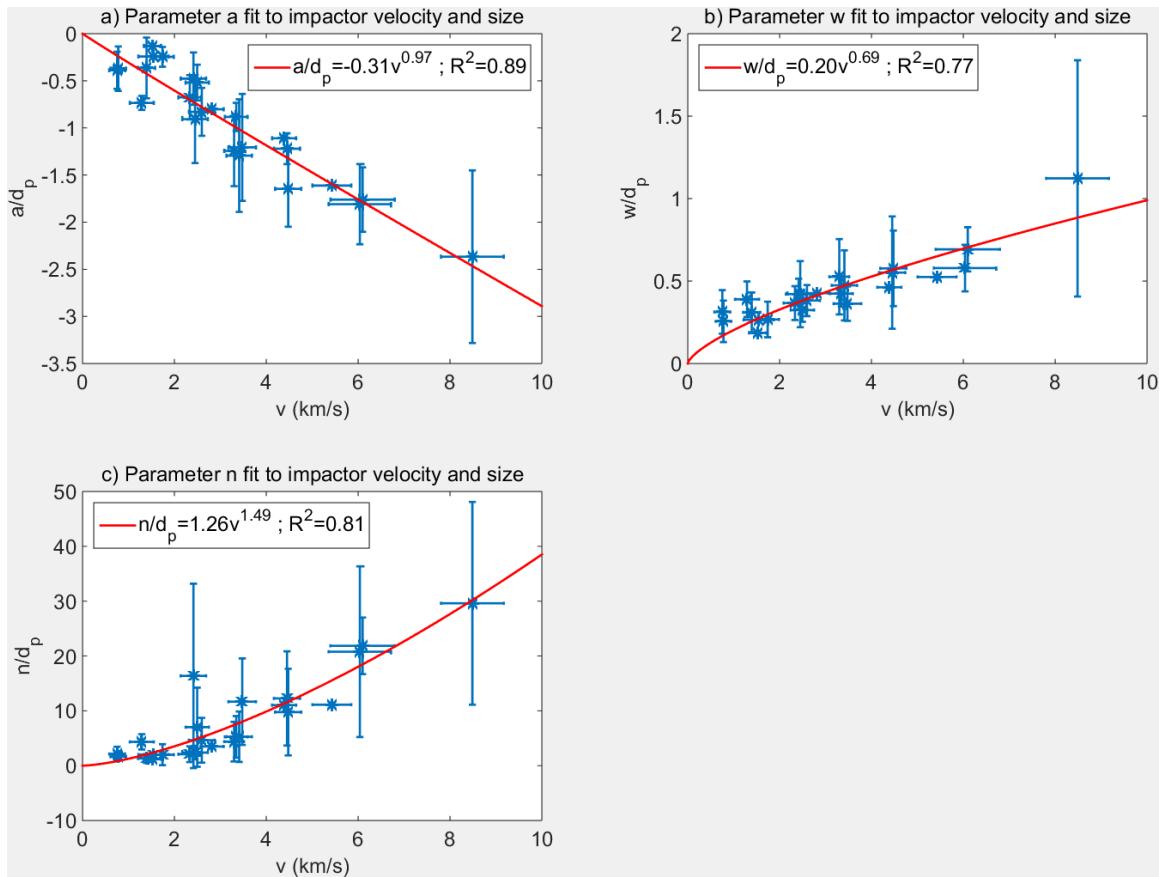


Figure 4.5: Equation for fitting used was $p = \alpha v^\beta$ where p is the parameter to be fit. Vertical error bars were plotted only in cases where there were more than 5 measured crater surfaces to fit parameters to. Otherwise the vertical error bar is missing due to the fact that there is no good estimate of the error. a) Fit for parameter a , crater depth. Fit equation is similar to measured depth scaling law in section 3.3. b) Fit for parameter w , crater radius. Good agreement with the diameter scaling law measured in section 3.3. c) Fit for parameter n , crater curvature. Suggests that as velocity increases and/or size decreases, the hole is more cylindrical.

our previous method of measuring the depth and diameter of the crater.

The n parameter is a measure of the curvature of the crater. The higher n is, the closer the crater shape approaches a cylinder. Looking at figure 4.5c, it is clear that as the velocity of the particle increases and the size of the particle decreases, the n parameter goes up. This is interesting as many previous studies suggest that hypervelocity impacts produce craters that are hemispherical. This increase in the n parameter suggests that up to a point, the particle is digging a “tunnel” into the material. This may be due to the projectile and target material. The compressive strength of pvdf is around 62 MPa while the bulk modulus of iron is 119 GPa. Since PVDF will fail under a much lower compressive stress, it seems possible that the iron particle will not deform at high speeds immediately upon impact with the weaker PVDF.

4.5 Conclusions and Future Work

Craters created by micron or smaller dust particles in PVDF are best described by a super Gaussian, a Gaussian with a higher exponent than 2. This is due to the fact that the craters are more cylindrical and flatter bottomed. A Gaussian shape is not wide enough near the maximum depth. Furthermore, the fits were quite accurate as they were iterated until the parameters were accurate to 0.001 of a pixel and the goodness of fit parameter showed a factor of 10 or more improvement for most fitted surfaces. Future fitting work may increase the number of parameters being used to fit to the crater surface.

In the next chapter, the signal from a PVDF detector is explored by using a 2D poisson relaxation solver. This code was originally used in Poppe et al. (2010) and is now being rechecked with the new crater fitting work.

Chapter 5

PVDF Signal Simulations

5.1 Introduction

PVDF is a material with strong pyroelectric and piezoelectric properties. Because of this, it has a wide range of uses. A PVDF detector consists of a central thin layer of PVDF which is permanently polarized. Metallized contact electrodes are then applied across the surface of the PVDF. When a dust impact occurs, a fast current pulse is generated across the capacitor and this is what is measured by the detector (Simpson and Tuzzolino, 1985). This signal allows the detector to count the number of particles impacting the detector.

5.2 Previous Work

Assuming I have a PVDF detector of thickness L and area A , and a volume polarization of P pointing in the direction normal to the area, then a signal of ΔQ is produced. It is believed that the signal is produced not by the pyroelectric or piezoelectric responses, but instead from the rapid destruction of polarized material. Simpson and Tuzzolino (1985) calculates the expected charge to be

$$\Delta Q = \left[\frac{\epsilon_r l / L}{1 + (\epsilon_r - 1) l / L} \right] \frac{\pi}{4} D^2 P \quad (5.1)$$

$$\Delta Q' = \frac{\pi}{4} (D')^2 P \quad (5.2)$$

where ϵ_r is the dielectric constant of PVDF and has a value of $\epsilon_r = 12$, l is the crater depth in μm , D is the crater diameter in μm , and D' is the diameter of the hole in the case of a penetrating

impact in μm . In order to use these equations to calculate the expected signal from a particle with a mass and velocity, Simpson and Tuzzolino (1985) uses an equation given by Pailer and Grün (1980) for the penetration depth l in metals and plastics,

$$l = m_p^{0.40} v_p^{0.88} \rho_p^{0.33} / (\eta_t^{0.06} \rho_t^{0.5}) \quad (5.3)$$

where l is the crater depth in cm, m_p is the mass of the projectile in g, v_p is the projectile velocity in km/s, ρ_p is the projectile density in g/cm^3 , η_t is the ductility of the target material, and ρ_t is the density of the target in g/cm^3 . By assuming the ductility to be unity, and that l and D are proportional to each other (Nagel and Fechtig, 1980), then these equations can be used to predict the signal produced by the PVDF detectors knowing only the mass and velocity of the impactor. This results in

$$\Delta Q \propto l^3 (m^{1.2} v^{2.6}) \quad (5.4)$$

for small l/L and

$$\Delta Q \propto l^2 (m^{0.8} v^{1.8}) \quad (5.5)$$

for large l/L .

Poppe et al. (2010), on the other hand, assert that when the metal layer is destroyed, the permanently polarized material underneath is exposed thereby creating a net surface charge on a region of the detector. Near this crater, the exposed surface charge then creates fringing electric fields that induce a surface charge on the metal layer. Figure 5.1 shows the fringing fields around an impact crater in a PVDF detector. As you can see, the equipotential lines are curved near the crater inducing a movement of charge in the material near the crater. This “depolarization” charge is what is measured by the detector. The dimensions of the impact crater determine the strength of the resulting fringing fields and therefore the depolarization charge.

In order to test this theory, Poppe et al. (2010) used a Poisson-relaxation method on a two-dimensional 400x400 square grid with Dirichlet boundary conditions to determine the charge created by a cylindrical crater of given depth and diameter. Figure 5.1 shows a typical simulation setup. The shaded region is the pvdf material, and the white region is all vacuum. The polarization

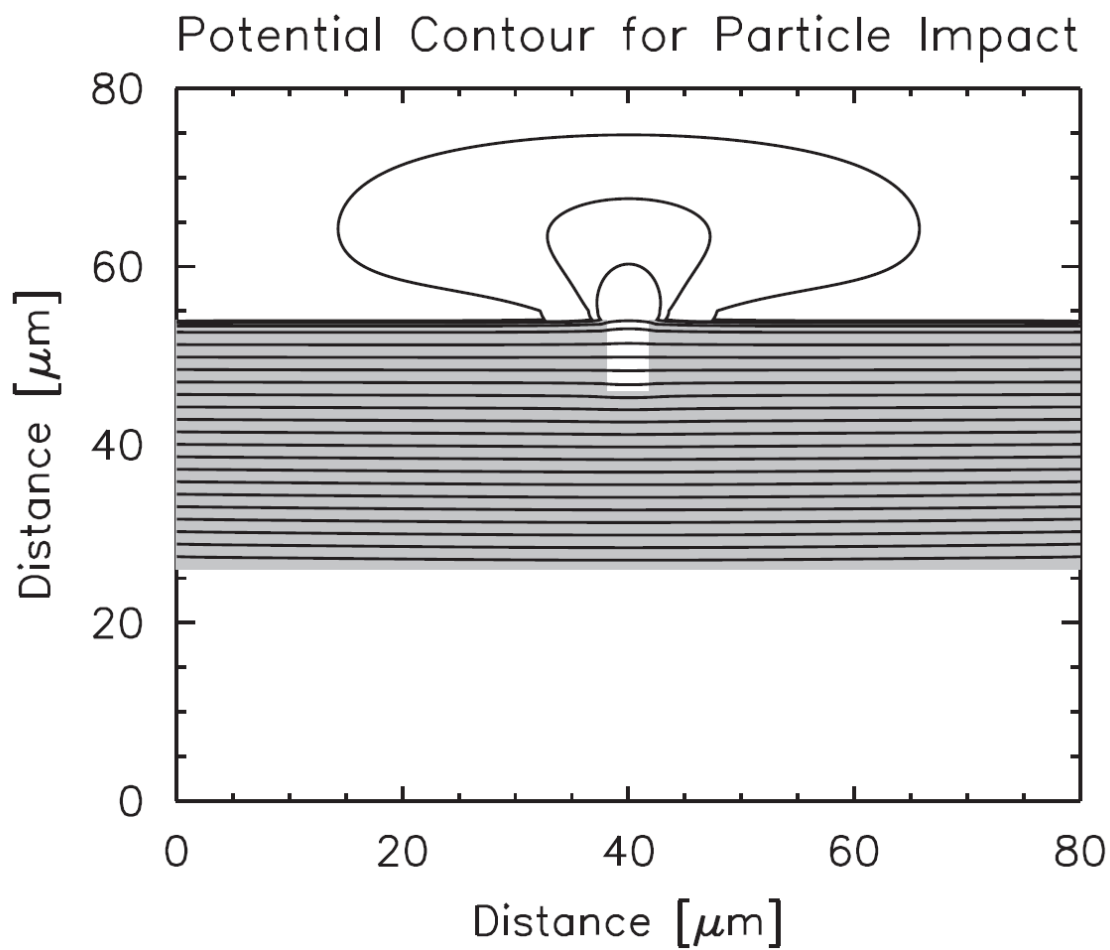


Figure 5.1: This shows potential contours for a $5 \mu\text{m}$ diameter crater and $10 \mu\text{m}$ depth crater. The shaded area represents PVDF material and the black lines are equipotential lines. Potential contours in the bulk of the PVDF are spaced evenly while near the surface the spacing is decreased to illustrate the fringing fields near the crater (Poppe et al., 2010).

density of the PVDF material was set to $5 \times 10^{-2} \text{ C/m}^2$ and the relative permittivity, ϵ_r , was set to 12. The surface charge density was calculated by finding the change in the electric field across the surface. The net charge produced by the detector was then calculated by subtracting the difference between the surface charge of a piece of PVDF with no crater, and a piece of PVDF with the crater assuming azimuthal symmetry (Poppe et al., 2010).

5.3 Relaxation Method Simulation

Relaxation methods are a way of solving ordinary differential equations by approximating them with finite-difference equations on a grid of points. This is done by taking an equation of the form

$$\frac{d\phi}{dx} = g(x, \phi) \quad (5.6)$$

and rewriting it using a finite difference approximation such as

$$\phi_k - \phi_{k-1} - (x_k - x_{k-1})g\left[\frac{1}{2}(x_k + x_{k-1}), \frac{1}{2}(\phi_k + \phi_{k-1})\right] = 0. \quad (5.7)$$

In this work, I am trying to solve Poisson's equation given by

$$\nabla^2\phi = f, \quad (5.8)$$

where f is an arbitrary function, using a relaxation method which can be done by the fact that the second derivative of a real-valued function on the real numbers can be approximated by

$$\frac{d^2\phi(x)}{dx^2} = \frac{\phi(x-h) - 2\phi(x) + \phi(x+h)}{h^2} + O(h^2). \quad (5.9)$$

Translating this into it's 2D equivalent gives

$$\phi^*(x, y) = \frac{1}{4}(\phi(x+h, y) + \phi(x, y+h) + \phi(x-h, y) + \phi(x, y-h) - h^2 f(x, y)). \quad (5.10)$$

By repeatedly setting $\phi^* = \phi$ and repeating the process, the method will relax to a solution. Once the potential is known over the entire simulated area, the charge density can be calculated as

$$-\nabla^2\phi = \rho/\epsilon_0, \quad (5.11)$$

where ρ is the charge density. With the charge density in hand, assuming the crater is axially symmetric, the total charge can be calculated on the top and bottom electrodes. The difference between the charge density on the top and the bottom is the charge measured by the instrument.

Previous work included an experimental dataset that measured the charge generated from iron impacts on a 28 μm thick PVDF detector. In order to compare the results of the experiment to the theory, a crater scaling law was taken from McDonnell and Sullivan (1991) and Lambert (1997) which is based on aluminum impacts in aluminum targets and adapted to iron impacts on PVDF. Using these scaling laws produced a result from the simulations that did not agree with experiment. In figure 5.2, the ratio of theoretical to experimental charge is plotted against experimental charge. Assuming the theory is correct, the graph should show the data as a straight horizontal line centered around 1. The fact that each one of these plots shows a clear dependence on experimental charge suggests that there is something fundamentally incorrect with each theory. Each theory, however, is dependent on the scaling law used to translate the impactor properties to the size of the crater created by the impactor, and the scaling law for iron impactors on PVDF has not been measured until now.

5.4 Results

The simulations from Poppe et al. (2010) were rerun using the scaling laws measured in this work. Figure 5.3 shows the results from three different theories of pvdf signal generation. The red circles show the original Poppe et al. (2010) simulation results, the blue crosses show the results of the simulation when the scaling laws are replaced with those measured in this work, and the black plusses show the original Simpson and Tuzzolino (1985) theory with their crater scaling laws replaced by those measured in this work. Interestingly, the simulation results became worse after using the measured crater scaling laws, however, the Simpson and Tuzzolino theory became better (compare the black plusses to figure 5.2a). It is clear, however, that the dependence of the theoretical charge on the experimental charge is still incorrect as the results show a clear dependence on experimental charge that should not be present. This presents the largest problem

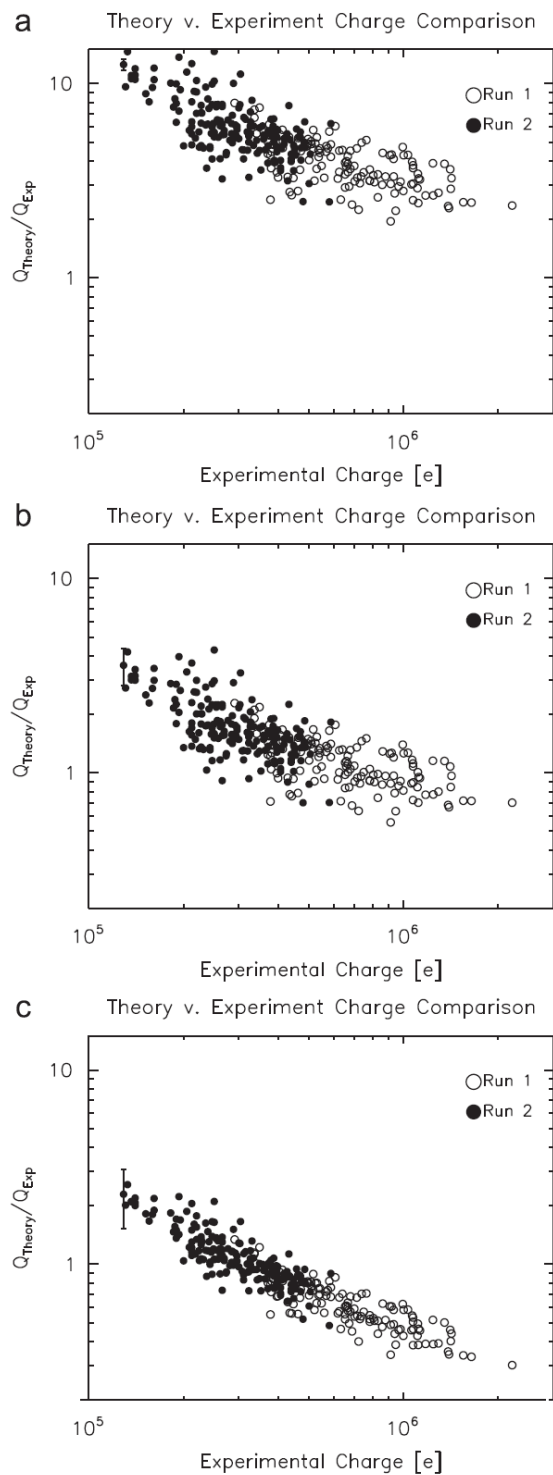


Figure 5.2: The ratio of theoretical to experimental charge for (a) Simpson and Tuzzolino's theory, (b) an analytic approximation and (c) Poppe et al. (2010) (Poppe et al., 2010).

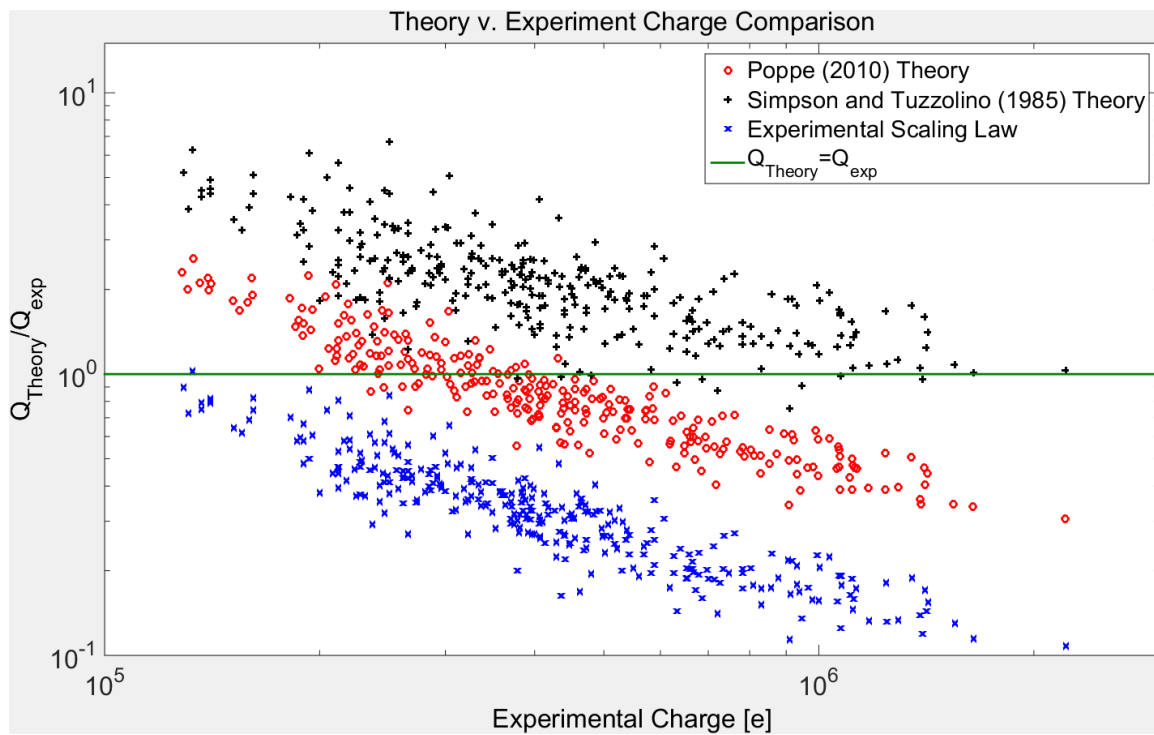


Figure 5.3: The ratio of theoretical to experimental charge showing simulation results from using the crater scaling law used in Poppe et al. (2010) and the crater scaling law measured in this work. The black pluses are using the crater scaling law measured in this work but using the theory from Simpson and Tuzzolino (1985).

as this indicates that there is something wrong with the current theory of signal generation.

In order to determine where this dependence may be coming from, some improvements were made to the code in order to speed up convergence. The previous code used an initial guess of the potential of 0 V at every grid point. The new code now uses the potential expected when the pvdv has no crater as an initial starting point. A simulation run is shown in figure 5.4. The potential difference across the PVDF was 13.176 kV on all samples. As seen in figure 5.4a, the initial potential guess was linearly changing between the two surfaces of the PVDF and constant outside of the PVDF. This allows for faster convergence as the expected result need not diffuse in through the boundary conditions. The final result looks similar to what intuition would suggest. Most of the contours are unchanged throughout the PVDF and on the side without the crater it looks identical to the initial guess. Near the crater, the potential lines are curved which changes the electric field in the region. This situation is better illustrated in figure 5.5 where the electric field and charge density in the simulated area is shown. Here it is obvious that the charge is all near the surface of the PVDF. This can be seen in both electric field plots and is most obvious in the charge density plot. The contours here are very hard to plot since they are so close together (the surface boundary layer should only be one grid spacing, however it appears in these figures to be smoothed out over approximately 5 grid cells). This effect is likely due to the discretization of the gradient calculation.

In order to determine the cause of this spurious dependence, the code was modified with several changes. As a test, the relative permittivity of PVDF and the polarization of PVDF were independently varied to see if this could be the cause of the dependence. This was done partially because the permittivity of PVDF is not well known. It is dependant on temperature and so can be expected to change over the course of an experiment. In order to do this, the polarization of PVDF was varied until the first simulated crater produced a charge similar to what was measured. Then the entire dataset was rerun using this new value of permittivity. The results of this test are shown in figure 5.6. It is clear that changing the permittivity does not change the trend of the data. Interestingly, the value of permittivity used appears to reduce the spread of the data which

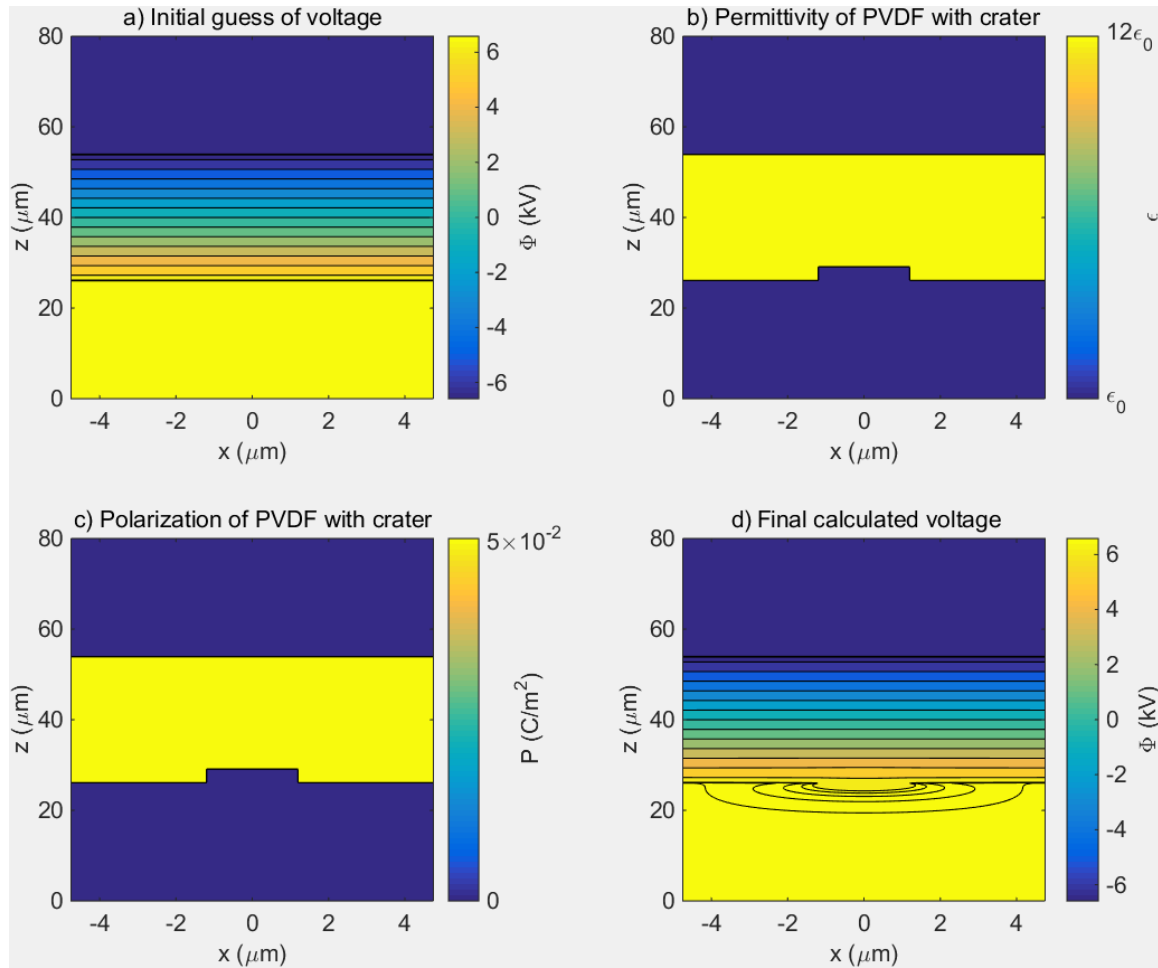


Figure 5.4: Contour plots of the simulation data. Each of these plots shows a slice through the center of the crater. a) Initial potential guess, potential lines are spaced 1kV apart from -6 kV to 6 kV. Near the PVDF surface, starting at ± 6.5 kV, lines are spaced every 20 V. b) Permittivity of the simulation, shaded region is PVDF. c) Polarization of simulation, shaded region is PVDF. d) Final calculated potential, same contour lines as a.

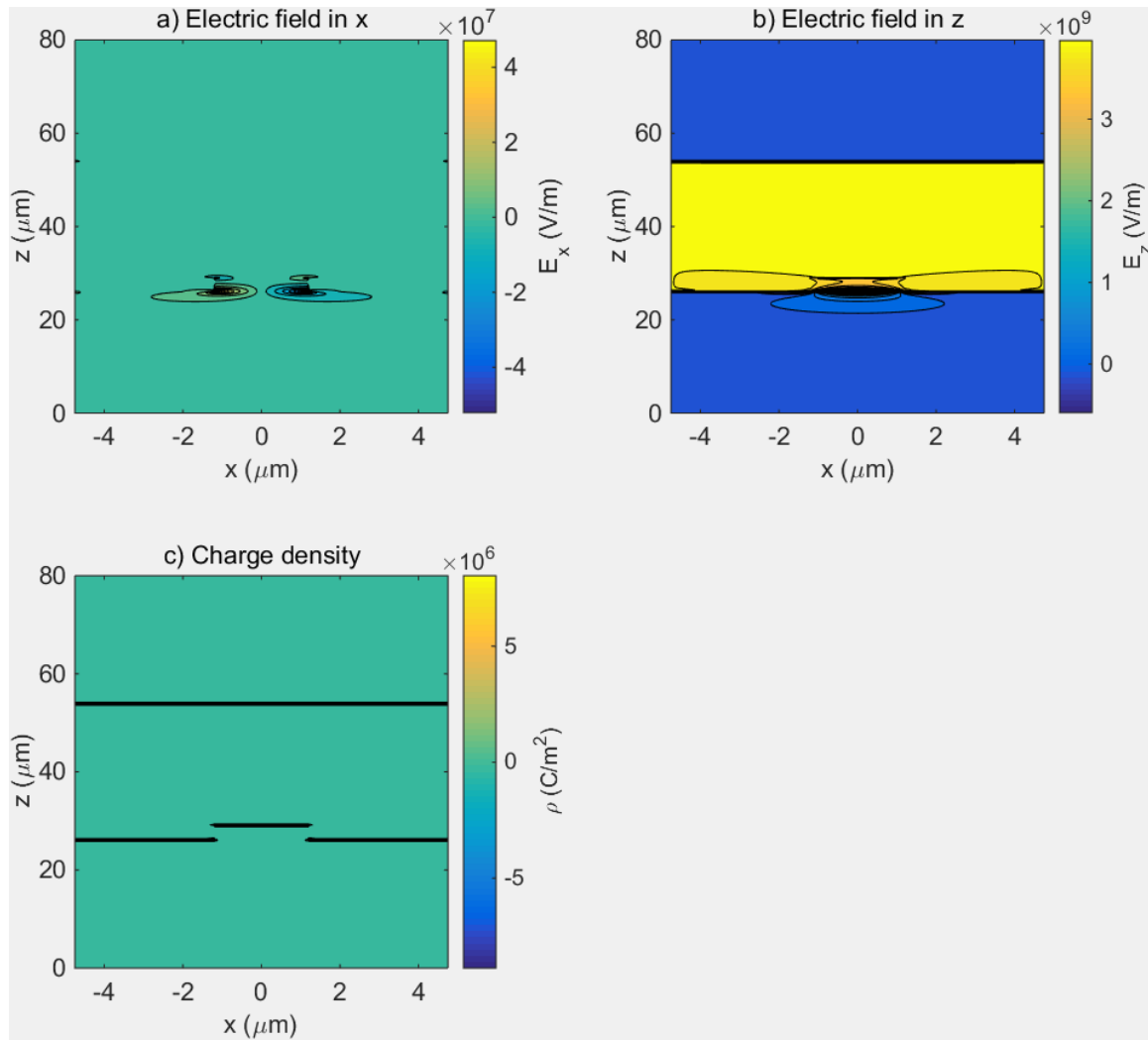


Figure 5.5: Contour plots of the E fields and charge. a) Calculated electric field in the x-direction (notice the magnitude is at most 2 orders of magnitude smaller than in the z-direction). b) Calculated electric field in the z-direction. c) Charge density.

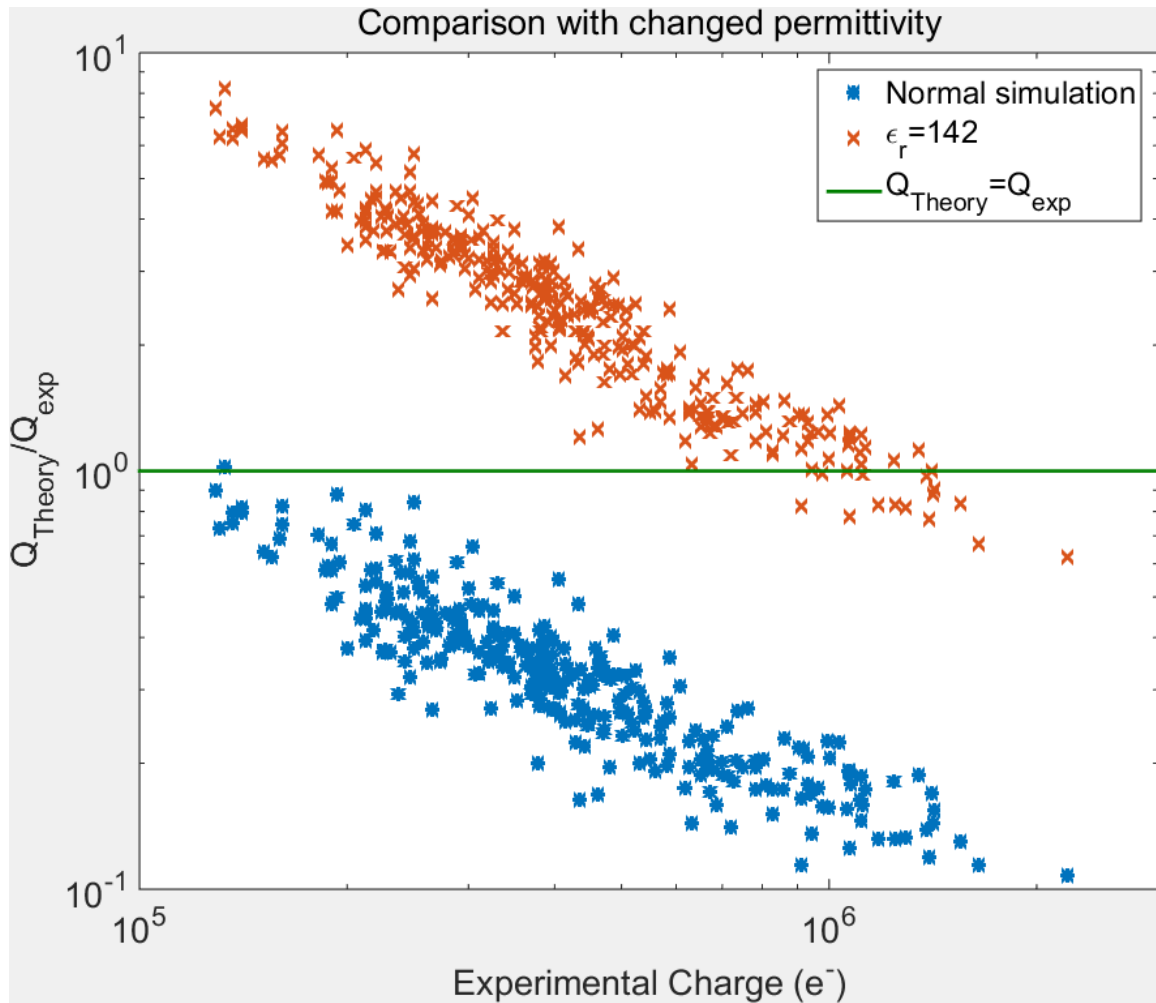


Figure 5.6: Comparison between simulation with updated crater scaling law and with a different relative permittivity. The trend continues in both datasets and does not appear improved at all by changing the permittivity.

suggests that changing the permittivity is not equivalent to just changing a multiplicative factor; however, the largest affect seems to be multiplying the simulation by a multiplicative factor. The permittivity used here is clearly ridiculous, at $\epsilon_r = 142$, but this exercise was still illustrative in that it suggests that dependence on the exact value of the permittivity is not particularly important.

The polarization of PVDF was also varied independantly to the relative permittivity in the same manner. Unfortunately the results also suggest that the polarization by itself is not likely to be the issue. The polarization was measured to be $P = 0.196 \text{ C/m}^2$. This value is also too high to be sensible. By varying both the permittivity and polarization, it is discovered that the polarization parameter affects the measurement strongest. The measured values were $\epsilon_r = 11.5$ and $p = 0.19 \text{ C/m}^2$. The results are displayed in figure 5.7. Changing the polarization seems to have the same effect as changing the permittivity. It increases the charge for all points by some common factor. This unfortunately does not fix the major problem, that the predicted charge from the theory does not follow a straight horizontal line on the plot.

The resolution of the experiment in the z-direction was held to just $0.2 \mu\text{m}$ per grid spacing. This is due to the fact that the entire width of the PVDF must be simulated. On the other hand, the x-direction was scaled such that the diameter of the crater was 100 grid spacings. This means that the resolution in the z-direction is significantly reduced compared to the x-direction, with the crater depth taking up as small as only 16 grid spacings. This does not seem sensible, so the grid spacing in the z-direction was increased by a factor of 4 to $0.05 \mu\text{m}$ per grid spacing. This was done by doubling the resolution in the z-direction and increasing the area within the simulation that was considered part of the PVDF. This resulted in simulations that look like 5.8. The results of these simulations are shown in figure 5.9. Looking at this, the amount of charge increased, but otherwise doesn't appear to have any other affect. This means that the spurious dependence is not due purely to discretization effects. If this were the case, one would expect the error to decrease as the simulation approached the continuum. Since this is not the case, increased resolution appears only to help with the amount of charge calculated.

Another improvement in the code is that the shape measured in chapter 4 was used to shape

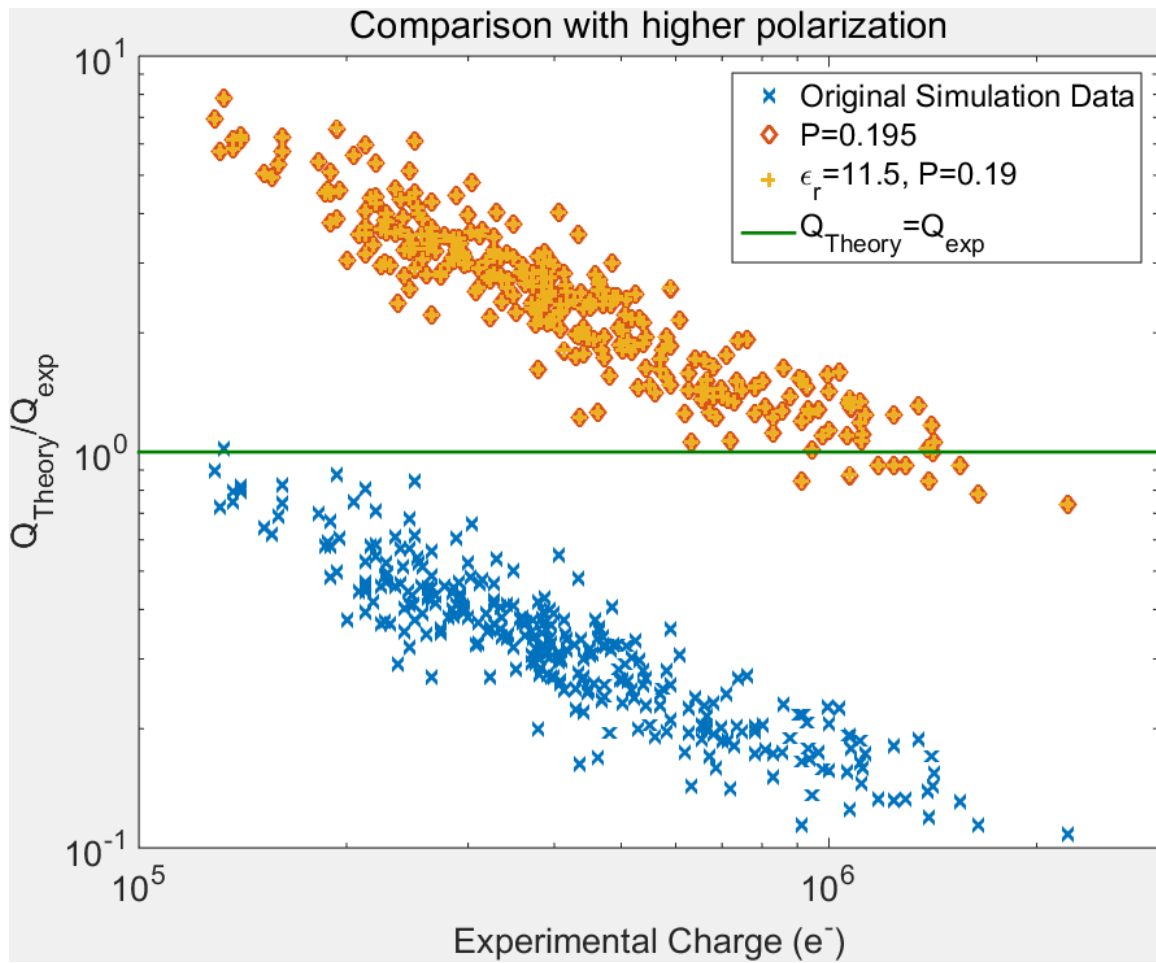


Figure 5.7: Comparison between simulation with the original simulation using measured crater scaling law and same simulation with different polarization, and with different polarization and relative permittivity. Unfortunately the trend has not been fixed by varying polarization.

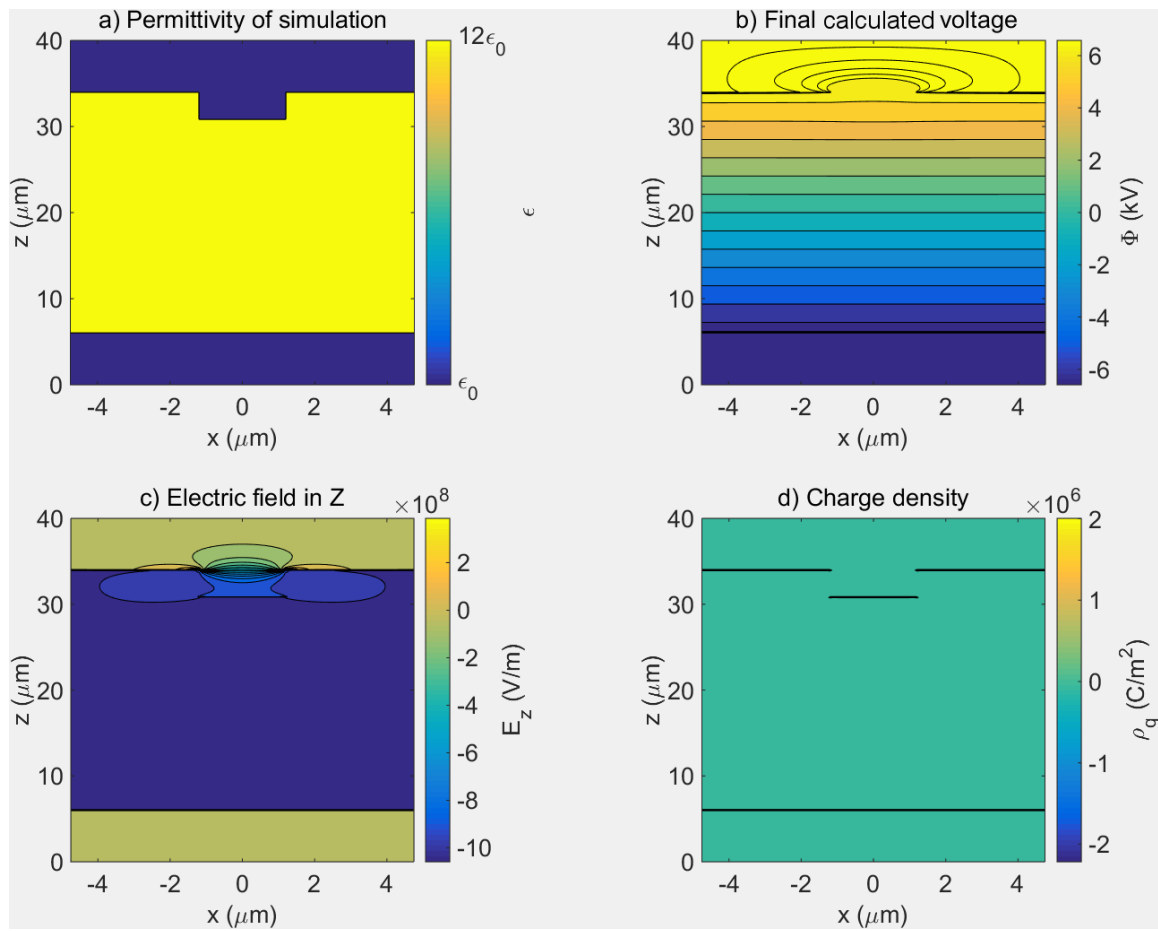


Figure 5.8: Simulation run with a 401x801 grid, resolution is quadrupled in z compared to figures 5.4 and 5.5 by doubling the number of z grid cells and doubling the number of cells the pvdf spans.

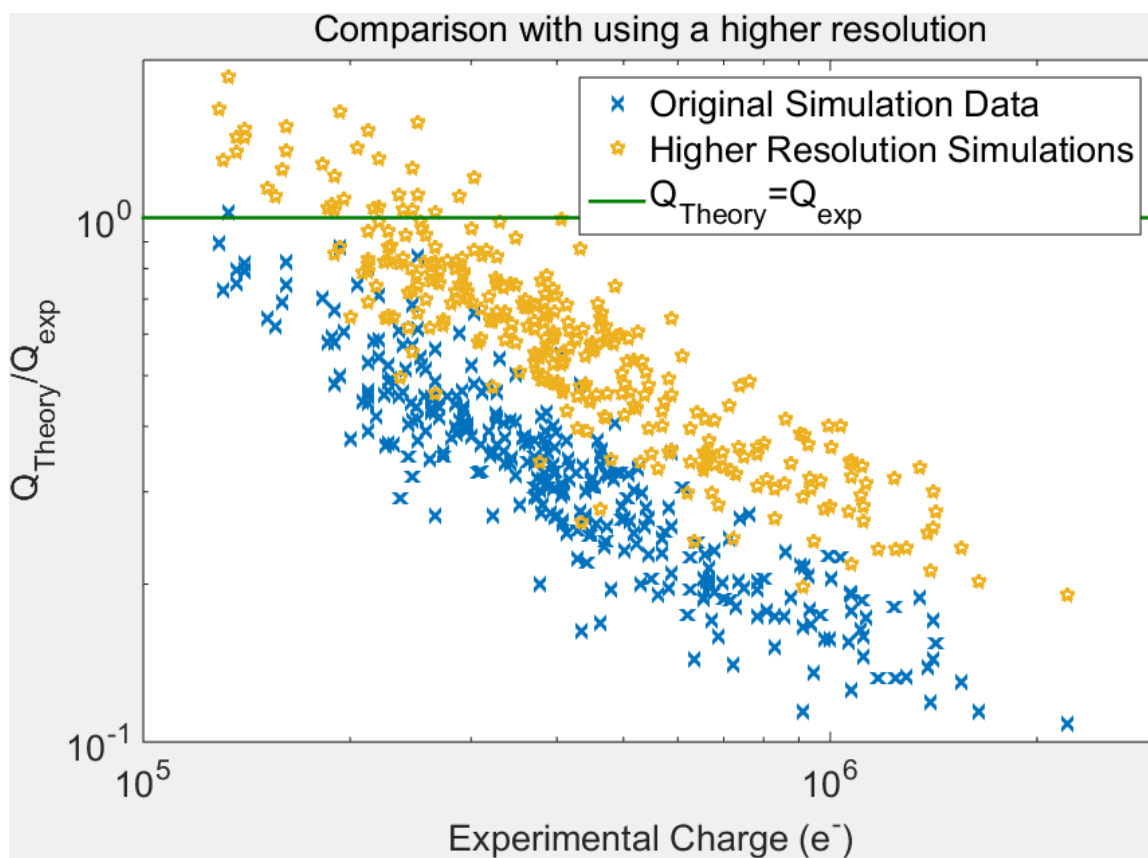


Figure 5.9: Original simulation results with measured scaling law plotted with simulation results with increased resolution in the z-direction. Resolution was increased by a factor of 4.

the crater in the simulation. Previous simulations only used a cylindrical shape with the depth and diameter as input parameters. This new code models the crater as a super Gaussian using parameters determined by the scaling laws measured in chapter 4. Figure 5.10 show the simulation properties used. The results of these simulations are shown in figure 5.11. Unfortunately the spurious dependence does not go away. Changing the shape of the crater did seem to make a very slight improvement to the data, however it still does not fix the dependence. It is unclear as to where this dependence is coming from.

5.5 Conclusions and Future Work

The Poisson relaxation simulation did not yield results that correspond with experiment. The biggest problem is that despite improvement to the code through better crater scaling laws, to higher resolution, to better crater shape, there is always a dependence of the ratio of the predicted charge to the experimental charge on the experimental charge. It is unclear as to where this dependence is coming from, however it shows that there is a clear error somewhere, be it in the code or in the theory. Increasing the resolution of the simulation should increase the fidelity and allow for more intricate detail in simulating the shape of the crater. Perhaps modeling the crater shape better may improve the results from the simulation, though this does not seem likely. Furthermore, the impact process generates heat which penetrates into the surface of the PVDF. This extra heat could destroy the polarization of the PVDF material creating an effective crater that is larger than the physical surface of the crater. This effect would have some dependence on projectile energy which relates to generated charge signal in such a way that the results should be improved.

In the next chapter, the results from each chapter are summarized. Some suggestions for continuing this work are also made.

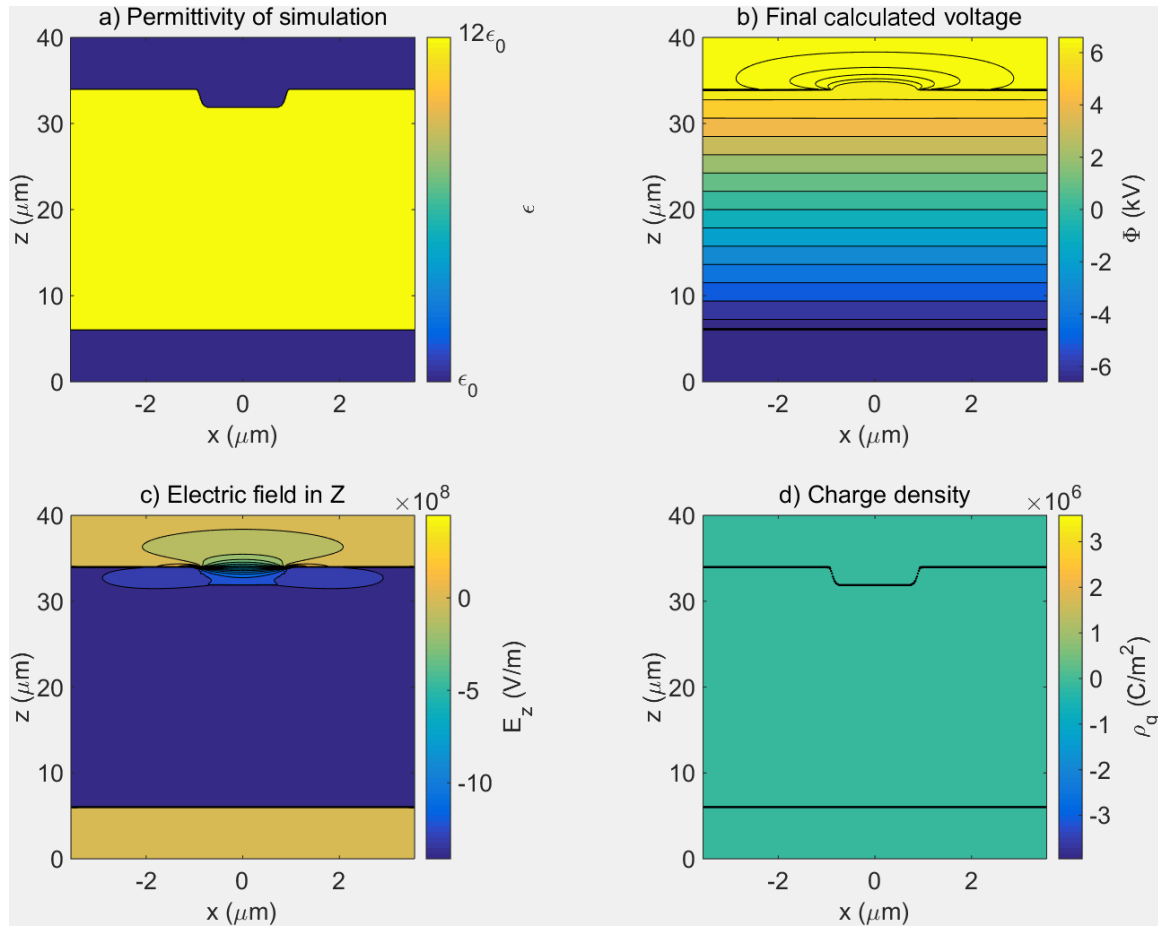


Figure 5.10: Simulation run with a 401x801 grid, and the crater is modeled as a super Gaussian based on the fitting parameters measured in Chapter 4. a) The permittivity of the simulation (looks identical to the polarization but with different color values). b) Final calculated potential of the simulation. c) Electric field in the Y-direction. d) Charge density.

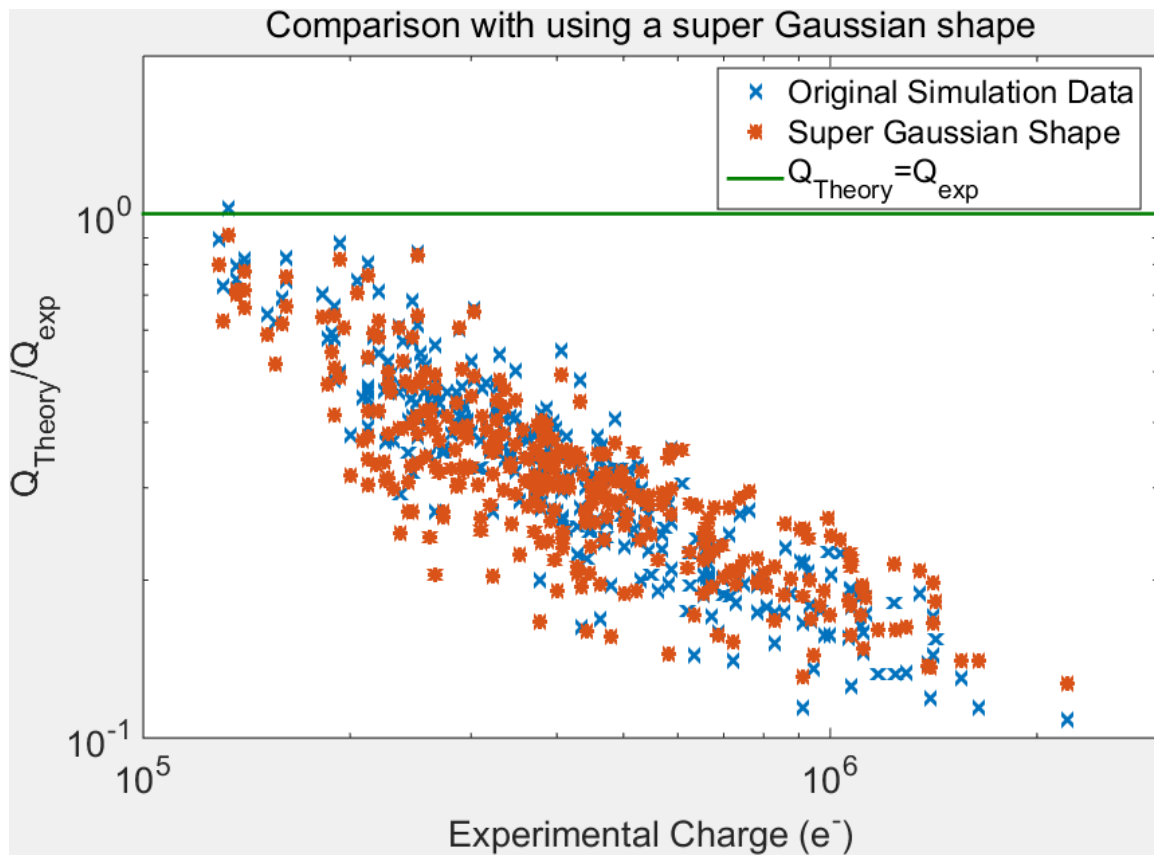


Figure 5.11: Original simulation results with measured scaling law plotted with simulation results with super Gaussian shaped crater. The spurious dependence has been very slightly reduced, but otherwise the results appear similar.

Chapter 6

Conclusions

Dust is a new and very interesting field of study. It is still very difficult to detect and characterize, however offers many rewards for doing so. It holds a wealth of information that has previously been ignored. A 3MV dust accelerator facility was described as well as its operation and characteristics. This new tool has been used in many experiments. These experiments include calibration of dust detectors, damage studies in various materials, basic scientific phenomena such as ablation, and impact cratering physics from micron sized dust particles. The accelerator is a wonderful tool that will be used for many forms of scientific enquiry in the future.

The methodology and results of a study to measure crater scaling laws of spherical iron impactors in PVDF targets was described. The scaling law for the depth and diameter of impact craters was measured. The technique used to do these measurements was 3D photogrammetry, where the 3D shape of an object is determined from two images of the same object taken at different viewing angles. This technique was checked on a couple craters where the depth was measured both by the 3D photogrammetry technique and from measuring the outline of the crater by making a cross section of the crater using a FIB. This technique will prove invaluable in the future for analyzing surface defects and impact craters.

Further study into the cratering process was performed using SPH codes. This effort unfortunately did not lead to results, however, provided insight into the use of SPH codes for hypervelocity impact study. Instead, the detailed shape of a crater was described by fitting a super Gaussian surface to several measured crater surfaces. This allowed fitting parameters to be measured that

determine the form of the super Gaussian the crater will take depending on the velocity and size of the impactor. As expected, the two fitting parameters that are similar to crater depth and crater diameter resulted in measured scaling laws very similar to those measured for crater depth and diameter. The other parameter, the curvature of the crater, showed that the faster and smaller the particle was, the more cylindrical the crater was.

A Poisson relaxation simulation was run to determine the expected charge generated on a PVDF detector with a given impactor velocity and size. This simulation was repeated several times with several different changes to try to discover the physical processes in generating the signal. The results of the simulation always show an odd trend where the theoretically determined charge showed an obviously incorrect correlation to the experimentally determined charge. Originally this was believed to be caused by the use of an incorrect scaling law, however, this has proven to not be the case. Furthermore, it has been proven that not knowing the exact value of the permittivity or polarization has also not contributed significantly to this effect. Modeling the shape of the crater has improved the results very slightly, but not enough to consider it the reason behind the spurious dependence.

Future work includes determining where the spurious dependence is coming from. It is still unclear why the theory over estimates charge on low charge signal and underestimates the charge on large signals. There may be more to the theory that has yet to be discovered. The resolution of the simulation can be increased further. Also the simulation can be rewritten to be fully 3D to handle non-normal angles of incidence. Also, a melt layer of PVDF may be created due to the heat generated by the impact. This melt layer would add to the size of the crater changing the crater to an effective crater size that was not taken into account in this work. This effect would be dependent on projectile energy and could explain this trend. With these improvements, perhaps the spurious dependence will also become understood. Furthermore, the cratering study can be extended to other impacting materials, like pyroxene or other minerals that may be more similar to what you expect to see in space. Also this study could be repeated but varying the impact angle of the dust. All impacts in this study were at normal incidence. This may not be the case in space

and would help enlighten the process of generating the signal as the crater formed is no longer symmetric.

With some more development, PVDF sensors can provide a wealth of information. Their lightweight and low power consumption make them ideal as dust detectors aboard any number of spacecraft. With a better understanding of how the detector works, the limits of the detector can be better understood and the science return can be increased. The impactor mass and velocity can be better constrained. In the future it would be ideal for every spacecraft to have a small pvdf dust detector to provide information on the local dust environment.

Bibliography

- Auer, S., 2001. Instrumentation, in *Interplanetary Dust*. Springer Verlag.
- Bay, H., Tuytelaars, T., Van Gool, L., 2006. Surf: speeded up robust features. In: *Proceedings of the 9th European Conference on Computer Vision*. pp. 404–417.
- Charters, A. C., Locke, G. S. J., 1958. A preliminary investigation of high-speed impact: The penetration of small spheres into thick copper targets. Tech. rep., NACA.
- Collette, A., et al., 2014a. Micrometeoroid impact charge yield for common spacecraft materials. *Journal of Geophysical Research: Space Physics*, n/a–n/a.
URL <http://dx.doi.org/10.1002/2014JA020042>
- Collette, A., Sternovsky, Z., Horanyi, M., 2014b. Production of neutral gas by micrometeoroid impacts. *Icarus* 227 (0), 89 – 93.
URL <http://www.sciencedirect.com/science/article/pii/S0019103513003898>
- Colwell, J. E., et al., 2007. Lunar surface: Dust dynamics and regolith mechanics. *Rev Geophys* 45.
- Currie, D., DellAgnello, S., Monache, G. D., 2011. A lunar laser ranging retroreflector array for the 21st century. *Acta Astronautica* 68 (78), 667 – 680.
URL <http://www.sciencedirect.com/science/article/pii/S0094576510003371>
- Davis, T., 2001. Charging system.
URL <http://www.pelletron.com/charging.htm>
- Eichhorn, G., 1975. Measurements of light flash produced by high-velocity particle impact. *Planet Space Sci* 23, 1519–1525.
- Engel, O. G., 1963. Hypervelocity cratering data and a crater-depth model for the regime of partial fluidity. In: *Proceedings of the Sixth Symposium on Hypervelocity Impact*.
- Fechtig, H., Grün, E., Kissel, J., 1978. *Laboratory Simulation*. Wiley and Sons, pp. 607–669.
- Friichtenicht, J., 1962. Two-million-volt electrostatic accelerator for hypervelocity research. *REV SCI INSTRUM* 33, 209–212.
- Gault, D., 1973. Displaced mass, depth, diameter, and effects of oblique trajectories for impact craters formed in dense crystalline rocks. *The moon* 6 (1-2), 32–44.
URL <http://dx.doi.org/10.1007/BF02630651>

- Goldsworth, B. J., et al., 2002. Laboratory calibration of the cassini cosmic dust analyser (cda) using new, low density projectiles. *Adv. Space Res.* 29 (8), 1139–1144.
- Grün, E., et al., 2002. Dust astronomy: New venues in interplanetary and interstellar dust research. In: Sykes, M. V. (Ed.), *The Future of Solar System Exploration*. Vol. 272 of ASP Conference Series. Astronomical Society of the Pacific, pp. 283–295.
- Grün, E., et al., 2005. 2002 kuiper prize lecture: Dust astronomy. *Icarus* 174 (1), 1 – 14.
URL <http://www.sciencedirect.com/science/article/pii/S0019103504003197>
- Hasegawa, S., et al., 1999. Design of electrostatic accelerators for the development of microparticle detectors in japan. *Advances in Space Research* 23 (1), 119 – 122.
URL <http://www.sciencedirect.com/science/article/pii/S0273117798002385>
- Hirai, T., et al., 2014. Microparticle impact calibration of the arrayed large-area dust detectors in {INterplanetary} space (aladdin) onboard the solar power sail demonstrator {IKAROS}. *Planetary and Space Science* 100 (0), 87 – 97, cosmic Dust {VI}.
URL <http://www.sciencedirect.com/science/article/pii/S0032063314001366>
- Horányi, M., et al., 2008. The student dust counter on the new horizons mission. *Space Sci Rev* 140, 387.
- Horányi, M., et al., December 2014. The lunar dust experiment (ldex) onboard the lunar atmosphere and dust environment explorer (ladee) mission. *Space Science Reviews* 185 (1-4), 93–113.
- Hörz, F., 2012. Cratering and penetration experiments in aluminum and teflon: Implications for space-exposed surfaces. *Meteoritics & Planetary Science* 47 (4), 763–797.
URL <http://dx.doi.org/10.1111/j.1945-5100.2012.01354.x>
- Janches, D., et al., January 2006. Modeling the global micrometeor input function in the upper atmosphere observed by high power and large aperture radars. *Journal of Geophysical Research* 111 (A07317).
- Jones, C., 1981. The 25mv tandem accelerator at oak ridge. *NUCL INSTRUM METHODS* 184, 145–151.
- Kearsley, A. T., et al., 2006. Laboratory simulation of impacts on aluminum foils of the stardust spacecraft: Calibration of dust particle size from comet wild-2. *Meteoritics & Planetary Science* 41 (2), 167–180.
URL <http://dx.doi.org/10.1111/j.1945-5100.2006.tb00201.x>
- Kempf, S., et al., January 2005. High-velocity streams of dust originating from saturn. *Nature* 433.
- Kissel, J., et al., 2004. The cometary and interstellar dust analyzer at comet 81p/wild 2. *Science* 304 (5678), 1774–1776.
URL <http://www.sciencemag.org/content/304/5678/1774.abstract>
- Krasheninnikov, S. I., Smirnov, R. D., Rudakov, D. L., 2011. Dust in magnetic fusion devices. *Plasma Phys Contr F* 53, 083001.
- Krüger, H., et al., 2003. Jovian dust streams: A monitor of io’s volcanic plume activity. *GEOPHYS REF LETT* 30 (21), 2101.

- Lambert, M., 1997. Hypervelocity impacts and damage laws. *Advances in Space Research* 19 (2), 369 – 378.
URL <http://www.sciencedirect.com/science/article/pii/S0273117797000276>
- Landgraf, M., et al., May 2000. Aspects of mass distribution of interstellar dust grains in the solar system from in situ measurements. *Journal of Geophysical Research* 105 (A5), 10343–10352.
- Lane, G., 1969. The application of stereographic techniques to the scanning electron microscope. *J. Phys. E: Sci. Instr.* 2, 565–569.
- Latunde-Dada, S., et al., 2011. Hypervelocity impacts into graphite. *Journal of Physics: Conference Series*.
- Lowe, D., 2004. Distinctive image features from scale-invariant keypoints. *International Journal of Computer Vision* 60, 91–110.
- Luong, Q.-T., et al., 1993. On determining the fundamental matrix : analysis of different methods and experimental results. Research Report RR-1894, INRIA.
- McDonnell, J., Sullivan, K., 1991. Hypervelocity impacts on space detectors: decoding the projectile parameters. In: *Proceedings of the Workshop on Hypervelocity Impacts in Space*. Unit for Space Sciences, University of Kent, Canterbury, U.K.
- Mocker, A., et al., 2011. A 2mv van de graaff accelerator as a tool for planetary and impact physics research. *REV SCI INSTRUM* 82.
- Moritoh, T., et al., 2001. Optimization of a compact two-stage light-gas gun aiming at a velocity of 9 km/s. *Review of Scientific Instruments* 72 (11).
- Müller, E. W., August 1955. Field desorption. *Physical Review* 203, 618–624.
- Nagel, K., Fechtig, H., 1980. *Planet. Space Sci.* 28, 567–573.
- Pailer, N., Grün, E., 1980. *Planet. Space Sci.* 28, 321.
- Paler, E. P., Harrison, D. R., Grow, R. W., 1961. Charging, initial acceleration and detection of micron diameter particles. Tech. rep., Physics Division, Air Force Office of Scientific Research.
- Phillips, T., November 2007. Shielding spacecraft from dangers of space dust.
URL http://www.nasa.gov/vision/universe/watchtheskies/meteor_cloud.html
- Piazessi, G., 1973. Photogrammetry with the scanning electron microscope. *J. Phys. E: Sci. Instr.* 6, 392–396.
- Poppe, A., 2013. Private communication.
- Poppe, A., et al., 2010. Simulation of polyvinylidene fluoride detector response to hypervelocity particle impact. *Nucl Instr Meth Phys Res* 622, 583.
- Poppe, A., James, D., Horányi, M., Mar 2011. Measurements of the terrestrial dust influx variability by the cosmic dust experiment. *Planet. Space Sci.* 59, 319–326.
- Postberg, F., et al., 2009. Sodium salts in e-ring ice grains from an ocean below the surface of enceladus. *Nature* 459.

- Price, M. C., et al., 2010. Comet 81p/wild 2: The size distribution of finer (sub-10 m) dust collected by the stardust spacecraft. *Meteoritics & Planetary Science* 45 (9), 1409–1428.
URL <http://dx.doi.org/10.1111/j.1945-5100.2010.01104.x>
- Routier-Kierzkowska, A.-L., Kwiatkowska, D., 2008. New stereoscopic reconstruction protocol for scanning electron microscope images and its application to in vivo replicas of the shoot apical meristem. *Functional Plant Biology* 35, 1034–1046.
- Rudolph, V., August 1966. Massen-geschwindigkeitsfilter für künstlich beschleunigten staub. *Z. Naturforschg.* 21a, 1993–1996.
- Sawle, D. R., 1970. Hypervelocity impact in thin sheets and semi-infinite targets at 15 km/sec. *AIAA Journal* 8 (7), 1240–1244.
- Shelton, H., Jr., H. C., Wuerker, R., 1960. Electrostatic acceleration of microparticles to hypervelocities. *J APPL PHYS* 31, 1243–1246.
- Shu, A., et al., 2012. 3 mv hypervelocity dust accelerator at the colorado center for lunar dust and atmospheric studies. *Review of Scientific Instruments* 83 (7), –.
URL <http://scitation.aip.org/content/aip/journal/rsi/83/7/10.1063/1.4732820>
- Simpson, J. A., et al., 1986. Dust counter and mass analyser (ducma) measurements of comet halley's coma from vega spacecraft. *Nature* 321, 278–280.
- Simpson, J. A., Tuzzolino, A. J., 1985. Polarized polymer films as electronic pulse detectors of cosmic dust particles. *Nucl Instr Meth Phys Res* 236, 187–202.
- Spahn, F., et al., March 2006. Cassini dust measurements at enceladus and implications for the origin of the e ring. *Science* 311 (5766), 1416–1418.
- Srama, R., et al., Sep. 2004. The Cassini Cosmic Dust Analyzer. *Space Sci. Rev.*114, 465–518.
- Srama, R., Auer, S., 2008. Low-charge detector for the monitoring of hyper-velocity micron-sized dust particles. *MEAS SCI TECHNOL* 19 (055203).
- Sternovsky, Z., et al., Jan. 2007. The Large Area Mass Analyzer (LAMA) for In-Situ Chemical Analysis of Interstellar Dust Particles. *Dust in Planetary Systems* 643, 205–208.
- Sternovsky, Z., et al., March 2011. Novel instrument for dust astronomy: Dust telescope. In: *Aerospace Conference, 2011 IEEE*. pp. 1–8.
- Sternovsky, Z., et al., 2001. Ion field emission from micrometer-sized spherical glass grains. *IEEE Trans Plasma Sci* 29, 292–297.
- Stübig, M., et al., 2001. Laboratory simulation improvements for hypervelocity micrometeorite impacts with a new dust particle source. *Planetary and Space Science* 49 (8), 853 – 858.
URL <http://www.sciencedirect.com/science/article/pii/S0032063301000356>
- Szalay, J. R., Piquette, M., Horányi, M., 2013. The student dust counter: Status report at 23 au. *Earth Planets Space* 65, 1145–1149.
- Thomas, E., et al., December 2013. Fpga cross-correlation filters for real-time dust detection and selection. *Planetary and Space Science* 89, 71–76.

- Ticos, C. M., et al., 2006. Plasmadynamic hypervelocity dust injector for the national spherical torus experiment. *Review of Scientific Instruments* 77 (10).
- Tuzzolino, A., et al., 2005. Final results from the space dust (spadus) instrument flown aboard the earth-orbiting argos spacecraft. *Planetary and Space Science* 53 (9), 903 – 923.
URL <http://www.sciencedirect.com/science/article/pii/S0032063305000772>
- Wagner, S. A., September 2006. The apollo experience lessons learned for constellation lunar dust management. Tech. Rep. TP-2006-213726, National Aeronautics and Space Administration, Washington, DC 20546-0001.
- Wanke, M. C., et al., 2005. Advanced diagnostics for impact-flash spectroscopy on light-gas guns. Tech. rep., Sandia National Laboratories.
- Watts, A. J., Atkinson, D., 1995. Dimensional scaling for impact cratering and perforation. *Int. J. Impact Engng.* 17, 925–935.
- Webster, G., November 2008. Dust storm cuts energy supply of nasa mars rover spirit.
URL <http://www.jpl.nasa.gov/news/news.php?release=2008-206>
- Wikipedia contributors, 2015. Eugene Cernan.
URL http://en.wikipedia.org/wiki/Eugene_Cernan
- Yu, S., Sun, G., Tan, Q., 1994. Experimental laws of cratering for hypervelocity impacts of spherical projectiles into thick target. *Int. J. Impact Engng.* 15 (1), 67–77.